Ultrafast Structural Fluctuations and Rearrangements of Water's Hydrogen Bonded Network

by

Joseph J. Loparo

B.S. Chemistry
Case Western Reserve University, 2001

Submitted to the Department of Chemistry
in partial fulfillment of the requirements for the degree of

Doctor of Philosophy

at the

Massachusetts Institute of Technology
[February 2007]
December 2006

@ Massachusetts Institute of Technology. All rights reserved.

Signature of Author: ______________________
Joseph J. Loparo
December 15, 2006

Certified by: ______________________
Andrei Tokmakoff
Associate Professor of Chemistry
Thesis Supervisor

Accepted by: ______________________
Robert W. Field
Professor of Chemistry
Chair, Departmental Committee on Graduate Studies

MASSACHUSETTS INSTITUTE OF TECHNOLOGY
MAR 0 3 2007
LIBRARIES

ARCHIVES

This doctoral thesis has been examined by a committee of the Department of Chemistry that included:

Professor Keith A. Nelson ____________________
Chair

Professor Robert W. Field ____________________

Associate Professor Andrei Tokmakoff ____________________
Thesis Supervisor

Ultrafast Structural Fluctuations and Rearrangements of Water's Hydrogen Bonded Network

by

Joseph J. Loparo

Submitted to the Department of Chemistry on December 15, 2006
in partial fulfillment of the requirements for the degree of
Doctor of Philosophy

Abstract

Aqueous chemistry is strongly influenced by water's ability to form an extended network of hydrogen bonds. It is the fluctuations and rearrangements of this network that stabilize reaction products and drive the transport of excess protons through solution. Experimental observations of the dynamics of the hydrogen bonded network are difficult because (1) the timescales are exceedingly fast with relevant fluctuations occurring on a tens of femtosecond period and (2) the experimental probe must be sensitive to the local hydrogen bonded structure. In this thesis I address these experimental challenges through the development of ultrafast nonlinear infrared spectroscopy of the OH stretch of HOD in D_2O. The frequency of the OH stretch, ω_{OH}, is sensitive to the configuration of the hydrogen bonded pair. Therefore, time-dependent changes in ω_{OH} can be correlated with changes in the hydrogen bonded geometry.

I describe how broadband homodyne echo and polarization-dependent pump-probe experiments can be utilized to separate the contributions of spectral diffusion, vibrational relaxation and molecular reorientation. These experiments observe the underdamped motion of the hydrogen bonded pair and the librational motion of the OH dipole on the 180 and 50 fs timescales, respectively. These dynamics occur on a relatively local (i.e. molecular) length scale. At times greater than ~300 fs the experiments observe signatures of a kinetic regime. No longer can the spectral relaxation be ascribed to a clear molecular motion. Instead, the decay originates from the collective reorganization of many molecules.

Two dimensional infrared spectroscopy (2D IR) is applied to further investigate the mechanism of hydrogen bond rearrangement. 2D IR is an optical analogue of multidimensional NMR. As a correlation spectroscopy, time dependent changes in 2D IR line shapes track how vibrational oscillators relax from one frequency to another. I describe two methods of acquiring high fidelity 2D line shapes at wavelengths of 3 μm. Both methods utilize a HeNe laser as a frequency standard and balanced detection of the signal field. Spectral diffusion is found to dominate the evolution of the 2D line shapes of the OH stretch up to the vibrational lifetime of 700 fs. At times beyond this point the line shapes change substantially, indicating population relaxation out of the v=1 state and the formation of a spectroscopically distinct vibrationally excited ground state. Frequency dependent relaxation of the 2D IR line shapes reveals that molecules in hydrogen bonded and non-bonded configurations experience qualitatively different fluctuations. Non-bonded configurations are found to return to band center on ~100 fs timescale indicating that these configurations are inherently unstable. Hydrogen bonded oscillators undergo underdamped oscillations at the hydrogen bond stretching frequency before subsequent barrier crossing.

Hydrogen bonding not only affects ω_{OH}. The transition dipole, μ, is modulated by the hydrogen bonding interaction, resulting in higher oscillator strength for strong hydrogen bonds. I describe how modeling the temperature dependent behavior of IR and Raman line shapes in combination with nonlinear IR spectroscopies can extract the frequency dependent magnitude of μ. The variation in the transition dipole with frequency is found to be roughly linear on resonance but is found to be strongly nonlinear for weak hydrogen bonds on the high frequency side of the OH line shape.

Thesis Supervisor: Andrei Tokmakoff
Title: Associate Professor of Chemistry

Acknowledgements

"These walls are kind of funny. First you hate'em, then you get used to 'em. Enough time passes, gets so you depend on them. That's institutionalized...."
-Red from *The Shawshank Redemption*

It's true this place does kind of grow on you. I arrived at MIT a little over five years ago. It was the Tokmakoff group as an assembly of scientists and individuals that drew me here with their enthusiasm for their work and their kindness. I have not been disappointed, and if I had the opportunity to go back in time and do it all over again I would not choose differently. It has been my privilege to work with a number of people who I have admired not only for their scientific ability but whom are also great people. Unfortunately, it seems as if having these two traits in common is all too uncommon in the business of academics.

First and foremost I am indebted to the other members of "Team Water" especially Chris Fecko, Joel Eaves, Phillip Geissler and Sean Roberts, for without their help much of the work detailed in this thesis would not have happened. Chris was the ideal graduate student mentor. He is a true teacher and my own development as a scientist benefited greatly from his attention to detail and his technical abilities. Working together through the frustrations of setting up the first experiments was an experience I will never forget, and although it sounds ridiculously silly I view him more as an older brother than lab mate. Joel too became a good friend. One would think that goofing on the Boston accent could only bring so much enjoyment. Somehow Joel is able to keep me laughing. I have both enjoyed and benefited greatly from our conversations in his time at MIT and subsequently, and I am glad that that we have been able to remain friends. I am sure Chris and Joel would agree with me that Phill was an amazing resource to have around. Such brilliance and humility are rarely in the same package. In many ways he was a second advisor to us and my only disappointment was that he left for Berkeley! Sean has been my lab companion these past three years and in many ways has taken over from where Joel left off. His continuing work with Joel's MD model has provided important insight into our experiments, and I have enjoyed talking science and sharing our common interests in music and pop culture. I look forward to learning about the exciting things he and Team Water's newest members, Poul Petersen and Rebecca Nicodemus, discover. Go Team Water!

My scientific career has been shaped by two great scientific mentors. Cather Simpson at Case Western Reserve University provided me with an amazing opportunity to conduct research in her lab as a freshman. The years spent in her lab were very important to me and the friendships I formed with the people in the group were some of the strongest relationships I had in college. Her faith in my abilities played an important role in developing my own scientific self-confidence and the freedom she granted me to get my hands dirty helped me to significantly advance my abilities as an experimentalist. Likewise, I am indebted to my graduate advisor Andrei Tokmakoff. I think a special bond is formed with someone when you go through tough times together. I feel privileged to have been a part of the early years of the Tokmakoff group, and that I could help in Andrei's pursuit of tenure. It certainly was challenging but I am proud of what we were able to accomplish. I have grown substantially as a scientist under Andrei's tutelage. Much of the most significant change has been born out of our differences with the greatest lesson being the importance of taking scientific risks. Change isn't always easy, but I am grateful that Andrei challenged me.

And sometimes this place feels like a prison… There is a keen temptation when reflecting on one's graduate school career to sugarcoat the realities of life as a graduate student. Even for the most prolific, one's moments on the summits of scientific achievement are fleeting compared to the days spent in the valleys of failed experiments. Much of the graduate student experience is learning to deal with the inevitable frustrations of doing something that has never been done before and learning to embrace these challenges as part of the scientific process. To that end it is best to have people to help you on this journey. I have been blessed to have a great support network. Throughout my life my family, in particular my parents, Ken and Mary Loparo and my sister, Jessica Delaney, have been a great source of strength in all my endeavors and each in their own way has served as an example for me to emulate. From a young age, my parents have fostered my scientific interests both emotionally and financially. Many science kits and textbooks were purchased as my interests shifted from archaeology to astronomy to molecular biology to electronics to biochemistry and eventually to chemistry. More recently throughout graduate school my parents have been a consistent sounding board and have spent innumerable hours listening to me vent. So often this resulted in me placing my burdens onto their shoulders. God only knows how much premature aging I have caused them, but I know how thankful I am that they were and continue to be available for me. Having my sister, Jess, around for four of these years in Boston was an amazing gift. I have always been close to my sister, but these years our relationship certainly deepened. I will always fondly remember our Sunday night dinners together and trips to the dog park with my "niece" Cara. It has brought me much joy that she was able to find such a great husband in Michael Delaney and I value his support and friendship. My grandfather, James Bowman, also deserves special mention as his support throughout the years has always been appreciated. His life is yet another example, along with those of my parents, that has taught me what it means to have a career and the importance of never losing sight of the dignity of each human person. Lastly, I wish to thank the Palazzolo family for how they have welcomed me with open arms and have so earnestly supported me.

Graduate school is a transient existence and people come in and out of your life. I have enjoyed my time with the members of the Tokmakoff group over the years. In addition to those that I have worked with directly, a few deserve special mention. Lauren DeFlores and Matt DeCamp both became good friends and confidants these last few years. I am grateful for their support in matters both professional and personal. Two of my classmates have been with me since the beginning. I have been friends with Brian Yen and David Oertel ever since we started doing Quantum Mechanics problem sets together in the Fall of 2001. What a blessing to have two close friendships for one's whole duration of graduate school! These two were always there when it seems if everyone else had disappeared. We have been through a lot together, certainly way too much to detail here, and I am grateful for their loyal friendship. It saddens me to think we have to part ways, but I trust that we will stay in touch. Brian and I spent countless hours together getting dinner and discussing the very bizarre world that is MIT. The generosity of Brian and his "life partner", Melanie Pribisko, in often choosing to spend some of the precious time they had together to be with me has touched me deeply. It is something that I appreciate even more since I have been in my own long distance relationship. Dave, as a fellow Ohio product, has helped me to maintain my perspective lest I begin to believe that is nothing worth anything west of Pennsylvania. It is important to have those people to turn to who share your values and appreciate your worldview. In this regard, Dave has been a great sounding board for ideas and often a much needed advisor to my own struggles.

Lastly, I want to acknowledge my fiancée, Erin Palazzolo, and dedicate this thesis to her. It is only fitting that she share intimately in this work as we prepare to unite our lives fully in marriage. In a seemingly contradictory fashion our relationship has served to reprioritize my life, placing my professional life in proper perspective while at the same time revitalizing my work and filling it with new meaning. Sometimes one does not realize what they are missing until they find it. I could never have imagined how Erin's loving presence would change my life, and I continue to be pleasantly surprised each day. I am so grateful for her love.

Contents

List of Figures

Chapter 1

Introduction

1.1 Why water?

Water is truly everywhere. Maybe the only thing more ubiquitous than water is the number of research articles on water that begin with this observation. For it is most certainly true that the phrase "water is ubiquitous" is in fact ubiquitous. Water's abundance, in its own right, does not make it particularly exciting. There are plenty of things that surround us that are pretty boring. Could you imagine staying in a cramped and steamy dorm room for a week to attend a Gordon Research Conference on *Gaseous Nitrogen* or *Soil: More than just decaying vegetable matter*?

Water's peculiarities are what make it so intriguing. Compared to its peers (i.e. other low molecular weight liquids) water has a high melting and boiling point, expands upon freezing and has a high viscosity that *decreases* upon an increase in pressure.[1,2] Distinct from these "thermodynamic" anomalies, water has surprising aqueous reactivity. Water is able to quickly solvate nascent charge, which is critical for stabilizing charge transfer reactions, and is able to shuttle excess protons well beyond the diffusion limit for similarly sized ions. Because of our familiarity with water (it is ubiquitous after all) we take many of these anomalous properties for granted. From a young age we know that ice floats on water and so many of us never pause to think how abnormal it is for the solid phase to be less dense than the liquid. As countless authors have tirelessly pointed out, "as the lubricant of life"[3] water's relatively odd properties have implications from "astronomy to zoology"[4]. Life would be profoundly different if water were more mundane.

Water's structure and properties are due to the weak, non-covalent interaction known as the hydrogen bond. The structure of most other liquids is determined almost entirely by the repulsive forces that originate from molecules getting too close to one another. From a classical perspective, water's structure is a result of the balance of these repulsive forces with the attractive electrostatic interaction between the partially negative charge of the oxygen of one water molecule with the partially positive charge of the hydrogen on a neighboring water molecule. This attractive force is known as the hydrogen bond and is approximately 10 times stronger than most other non-covalent interactions, such as dispersion forces, but is roughly 10 to 100 times weaker than a covalent bond. Each water molecule is able to form four hydrogen bonds, by donating two and accepting two, resulting in a locally tetrahedral arrangement. It is rather easy to see why water behaves differently than other liquids incapable of forming hydrogen bonds. The attractive interaction between water molecules makes it harder to pull them apart, resulting in higher melting and boiling points and viscosity.[1,2] Increasing pressure reduces the hydrogen bonding interaction between water molecules. This decrease more than compensates for the reduction in volume between water molecules, reducing the viscosity. The highly directional nature of hydrogen bonds in water results in a hexagonal lattice of water molecules upon freezing that has a larger spacing between molecules compared to the liquid and is therefore less dense.

1.2 Models of water's structure

So what happens to ice's structure upon melting? It seems like a fairly straightforward question but after years of research it still raises rancor. Clearly the increase in density implies that the average distance between molecules must decrease, accompanying the increase in disorder of the liquid state. X-ray and neutron scattering experiments are able to provide a time-averaged glimpse of water's structure through radial distribution functions.[5] These measurements, along with MD simulations suggest that water maintains its largely tetrahedral structure but that at any given instant ten percent of the hydrogen bonds appear to be "broken".[6] This leads to another important question of what it really means to be hydrogen-bonded in the first place. Unfortunately, this question is also widely debated. Traditionally, people have defined that two molecules are in a hydrogen bond if they fulfill certain pairwise geometric or energetic criteria. Figure 1.1 illustrates the common geometric definition.

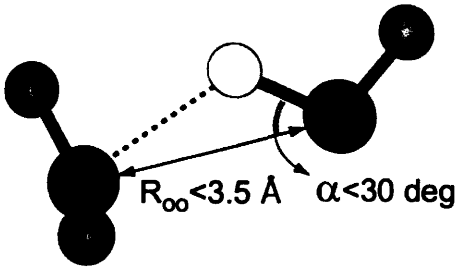

Figure 1.1. (Color) Geometric definition of a hydrogen bond.

This definition is not as arbitrary as it may at first appear. The oxygen – oxygen distance of 3.5 Å corresponds to the first minimum of the corresponding radial distribution function while the angle of 30° is the critical angle determined from the maximum amplitude of librational motions.[7]

Structural models[2] of water can often be broken into two limiting cases: mixture and continuum models. Mixture models presume that water is composed of a number of stable and distinct hydrogen bonding environments that interconvert.[8-10] The green free energy surface in Figure 1.2 depicts this scenario for two stable species, the hydrogen bonded pair (HB) and a broken or non-hydrogen bonded pair (NHB), which occupies a local minimum on the free energy surface. Continuum models assume that the liquid largely maintains the tetrahedral structure of ice with fluctuations about this average structure.[11-13] In this picture the NHB state occupies a maximum on the free energy landscape and would appear transiently as hydrogen bonded molecules switch partners or as large distortions about the HB state. This scenario is represented in the blue free energy surface in Figure 1.2.

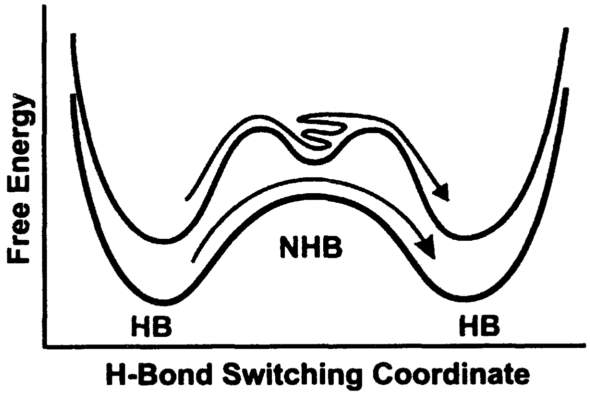

Figure 1.2. (Color) Two limiting free energy scenarios depicting hydrogen bond switching in liquid water. The scenarios differ in the stability of the NHB state. The NHB state occupies a local minimum (top) or transition state (bottom).

Mixture and continuum models can be misleading in that they are often discussed in very static terms. Molecules in liquids are constantly moving. This is especially true for water where relevant molecular fluctuations occur on a tens of femtoseconds (1 fs = 10^{-15} seconds) timescale.[14-19] It has been established that hindered rotations or librations, which occur on a ~50 fs timescale (i.e. 400-1000 cm^{-1}), play an important role in the initial solvation of charged products.[14] Likewise, hydrogen bond stretching on a 180 fs timescale, O..O..O bending motions on a 550 fs timescale, and the collective reorganization of water molecules (1.4 ps) contribute to the distortion and rearrangements of the hydrogen bonding network.[15]

A thorough understanding of water's structure requires the ability to distinguish distortions from stable structures. Ultimately a stable chemical species must occupy a minimum on the free energy surface and therefore persist in time longer than the timescale of the fastest intermolecular fluctuations. Therefore, stable species are separated on the free energy landscape by barriers greater than kT (~200 cm^{-1}). Instantaneous snapshots of atomic positions can be misleading because the configuration may represent molecules at their average (and therefore stable) positions or might indicate large but transient distortions about a point of stability. Eisenberg and Kauzmann, in their classic text *The Structure and Properties of Water*, astutely noted this when they suggested three different ways of describing structure in the liquid state.[2] The first, "I" (instantaneous) structure refers to atomic positions obtained by methods that have time resolution faster than the timescale of intermolecular vibrations. Measurements that probe the dephasing of electrons, such as x-ray absorption spectroscopy observe the "I" structure of the liquid. "V" (vibrational) structure is averaged over the timescale of intermolecular fluctuations and best represents the stable geometry of the liquid. "D" (diffusional) structure represents averaging the liquid structure over a timescale comparable to the timescale of diffusion.

Understanding how the "I" and "V" structural pictures of the liquid are related is the most useful for discerning between mixture and continuum models and are the most relevant for understanding how fluctuations mediate aqueous chemistry. It is these dynamics of the hydrogen bonding network that influence aqueous reactivity.

1.3 Infrared spectroscopy as a probe of liquid structure

Observing liquid structure on the timescale of molecular motions is an experimentally daunting task. In general, those techniques with the atomistic structural resolution necessary, such as NMR, lack the time resolution required to probe nature's fastest liquid, water. On the other hand, many of the standard ultrafast spectroscopies, such as time domain Raman methods or electronic echo experiments, lack the structural resolution necessary to resolve different hydrogen bonding environments. Ultrafast infrared spectroscopy serves as the perfect solution to these problems; the OH stretching frequency, ω_{OH}, is related to the local hydrogen bonding environment while the generation of ultrashort mid-IR pulses allows for time resolution on the timescale of water's intermolecular fluctuations.

Hydride stretching vibrations are particularly sensitive to the hydrogen bonding environment because the formation of a hydrogen bond weakens the OH force constant, red-shifting the stretching frequency (i.e. shifts to lower frequency). The shift in frequency is related to the strength of the hydrogen bond, with ω_{OH} being shifted by over a thousand wavenumbers from the gas phase frequency for extremely strong hydrogen bonds. With a shift of ~300 cm^{-1} from the gas phase value water's hydrogen bond is only of moderate strength.

The connection between ω_{OH} and hydrogen bonding environment is most clear in isotopic mixtures of water, such as HOD in D_2O, where the OH stretch is vibrationally isolated from other OH oscillators. The situation is more confusing in pure water where near degeneracies between neighboring OH oscillators result in the formation of excitonic states that are difficult to assign.[20] The past few years have seen a large theoretical effort to make the relationship between the OH stretching frequency of HOD in D_2O and the hydrogen bonding environment more quantitative.[17,21-23] While the details of the theoretical approaches have differed, there are number of qualitatively similar conclusions. First, the spectroscopy of the OH stretch of HOD in D_2O is really the spectroscopy of the hydrogen bonded pair with ω_{OH} determined almost entirely by the configuration of the hydrogen bond acceptor. As shown in Fig. 1.3, there is a relatively strong correlation between the hydrogen bond length, quantified here as R_{oo}, the distance between the neighboring oxygens, and ω_{OH}. Increasing the hydrogen bond length blue-shifts ω_{OH}, consistent with a decrease in hydrogen bond strength. While not as strong a correlation, when the angle between donor and acceptor becomes strained, denoted here as α, ω_{OH} also blue shifts due to hydrogen bond weakening. Second, the electric field projected onto the OH bond vector is the structural variable that is perfectly correlated with ω_{OH}. This field arises from all the surrounding D_2O molecules, yet, due to geometric arguments, is determined largely (~90%) by the hydrogen bond acceptor.

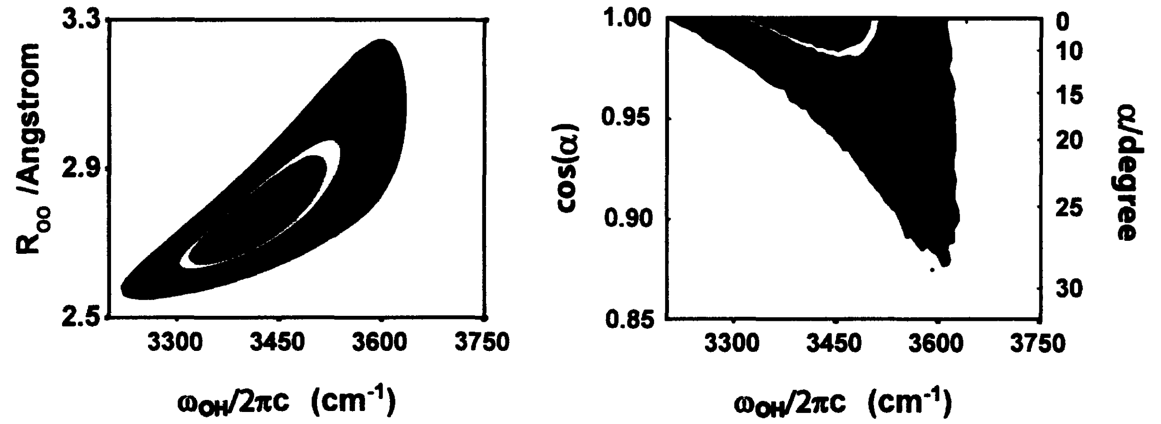

Figure 1.3. (Color) Joint probability distribution for intermolecular hydrogen bonding variables R_{OO} and cos(α) with ω_{OH} calculated within an MD simulation.[24]

1.4 Thesis outline

If ω_{OH} is related to the hydrogen bonding environment, then changes in frequency must reflect the structural dynamics of the hydrogen bonding network of water. Experiments that observe the time-dependent change in ω_{OH} are capable of resolving hydrogen bond dynamics. There is a long history of using ultrafast IR spectroscopy to accomplish this aim. The initial IR hole burning experiments were conducted by Graener, Seifert and Laubereau in 1991.[25] Subsequent studies have provided important characterizations of vibrational relaxation, spectral diffusion and molecular reorientation but have lacked the time resolution to access the dynamical regime (sub 100 fs) of the hydrogen bond network.[26-30] The goal of this thesis is to probe these structural fluctuations using ultrafast IR spectroscopy with the specific aim of understanding how they lead to rearrangements of the hydrogen bonding network of water. Emphasis is placed on using two-dimensional IR spectroscopy (2D IR) as a means of achieving these goals. 2D IR line shapes are optical analogues of their NMR counterparts. As a correlation spectroscopy, 2D IR allows one to observe the time dependent evolution of ω_{OH} on the timescale of vibrational dephasing.

Chapter 2 provides a practical introduction of the nonlinear spectroscopy techniques used in this thesis. Many excellent references provide a formal theoretical treatment of nonlinear spectroscopy.[31,32] The purpose of this chapter is to provide a physically minded description of the spectroscopy without all the details.

Chapter 3 describes the experimental methods used and developed in this thesis with a particular emphasis on the acquisition of 2D IR line shapes. I detail the generation of sub 50 fs mid-IR pulses in our home-built optical parametric amplifier (OPA), and the subsequent control of the timing and polarizations of these IR pulses in the interferometer. Short mid-IR pulse durations are necessary to probe the fast dynamics of water. High fidelity acquisition of 2D IR line shapes requires interferometric control of excitation pulse time delays and high signal to noise. I present two methods, one a mixed time/frequency approach and the other a direct time/time collection scheme, based on using a HeNe tracer as frequency standard and balanced interferometry.

An ensemble characterization of hydrogen bond fluctuations is provided in Chapter 4. Using broadband vibrational echo peak shift and polarization-selective pump-probe measurements of the OH stretch of HOD in D_2O, I describe how these experiments are able to observe the underdamped motion of the hydrogen bond which occurs on a 180 fs timescale and the librational or hindered rotational motion of OH dipoles on a 50 fs period. Up to ~300 fs the experiments observe the local molecular dynamics of the hydrogen bonding pair. Subsequent to this, the experiments probe hydrogen bond kinetics. In this regime, one cannot assign a well defined molecular motion to the measured spectral relaxation. Instead the experiments probe the collective reorganization of many molecules that accompany hydrogen bond switching. I conclude with a comparison to molecular dynamics (MD) simulations of water. These simulations have long predicted the underdamped motion of the hydrogen bond and librations but neither had been previously observed experimentally in the IR spectroscopy of water.

While providing an important point of comparison to MD simulations, Chapter 4 provides an average description of water's dynamics integrated over all hydrogen bonding environments under the OH line shape. Chapters 5 and 6 describe the 2D IR spectroscopy of the OH stretch of HOD in D_2O. As a correlation spectroscopy 2D IR is able to follow the spectral relaxation of different hydrogen bonded environments and watch them exchange. Chapter 5 details how spectral diffusion and vibrational relaxation appear in 2D IR line shapes. Chapter 6 describes how the asymmetries in the 2D IR line shapes reflect the mechanism of hydrogen bond switching.

Chapters 4-6 exploit the correlation between ω_{OH} and the hydrogen bonding environment to observe the structural rearrangements of the hydrogen bonding network. Chapter 7 asks how hydrogen bonding affects the transition dipole of the OH stretch. Increasing hydrogen bond strength results in higher OH oscillator strength. I describe how temperature dependent FTIR and homodyne echo measurements can be modeled to extract the frequency dependence of the OH transition dipole.

References

[1] *Water - A Comprehensive Treatise*, edited by F. Franks (Plenum, New York, 1972-1982), Vol. 1-7.

[2] D. Eisenberg and W. Kauzmann, *The Structure and Properties of Water.* (Clarendon Press, Oxford, 1969).

[3] L. D. Barron, L. Hecht, and G. Wilson, Biochem. 36, 13143 (1997).

[4] J. B. Asbury, T. Steinel, C. Stromberg, S. A. Corcelli, C. P. Lawrence, J. L. Skinner, and M. D. Fayer, J. Phys. Chem. A 108, 1107 (2004).

[5] T. Head-Gordon and G. Hura, Chem. Rev. 102, 2651 (2002).

[6] F. H. Stillinger, Science 209 (4455), 451 (1980).

[7] J. Teixeira, M.-C. Bellissent-Funel, and S. H. Chen, J. Phys. Condens. Matter 2, SA105 (1990).

[8] S. A. Benson and E. D. Siebert, J. Am. Chem. Soc. 114, 4296 (1992).

[9] G. W. Robinson, C. H. Cho, and J. Urquidi, J. Chem. Phys. 111 (2), 698 (1999).

[10] R. J. Speedy, J. Phys. Chem. 88, 3364 (1984).

[11] E. H. Stanley and J. Teixeira, J. Chem. Phys. 73 (7), 3404 (1980).

[12] S. A. Rice and M. G. Sceats, J. Phys. Chem. 85, 1108 (1981).

[13] F. H. Stillinger, Adv. Chem. Phys. 31, 1 (1975).

[14] R. Jimenez, G. R. Fleming, P. V. Kumar, and M. Maroncelli, Nature 369, 471 (1994).

[15] E. W. Castner, Jr., Y. J. Chang, Y. C. Chu, and G. E. Walrafen, J. Chem. Phys. 102, 653 (1995).

[16] I. Ohmine, J. Phys. Chem. 99, 6767 (1995).

[17] C. J. Fecko, J. D. Eaves, J. J. Loparo, A. Tokmakoff, and P. L. Geissler, Science 301, 1698 (2003).

[18] J. J. Loparo, C. J. Fecko, J. D. Eaves, S. T. Roberts, and A. Tokmakoff, Phys. Rev. B 70, 180201 (2004).

[19] C. J. Fecko, J. J. Loparo, S. T. Roberts, and A. Tokmakoff, J. Chem. Phys. 122, 054506 (2005).

[20] S. Woutersen and H. J. Bakker, Nature 402, 507 (1999).

[21] R. Rey, K. B. Moller, and J. T. Hynes, J. Phys. Chem. A 106 (50), 11993 (2002).

[22] C. P. Lawrence and J. L. Skinner, J. Chem. Phys. 117 (12), 5827 (2002).

[23] T. Hayashi, T. l. C. Jansen, W. Zhuang, and S. Mukamel, J. Phys. Chem. A 109 (1), 64 (2005).

[24] J. D. Eaves, A. Tokmakoff, and P. Geissler, Journal of Physical Chemistry A 109, 9424 (2005).

[25] H. Graener, G. Seifert, and A. Laubereau, Phys. Rev. Lett. 66, 2092 (1991).

[26] S. Woutersen and H. J. Bakker, Phys. Rev. Lett. 83, 2077 (1999).

[27] S. Woutersen, U. Emmerichs, and H. J. Bakker, Science 278, 658 (1997).

[28] G. M. Gale, G. Gallot, F. Hache, N. Lascoux, S. Bratos, and J.-C. Leicknam, Phys. Rev. Lett., 1068 (1999).

[29] J. C. Deak, S. T. Rhea, L. K. Iwaki, and D. D. Dlott, J. Phys. Chem. A 104, 4866 (2000).

[30] R. Laenen, K. Simeonidis, and A. Laubereau, J. Phys. Chem. B 106 (408-417) (2002).

[31] S. Mukamel, *Principles of Nonlinear Optical Spectroscopy*. (Oxford University Press, New York, 1995).

[32] J. Sung and R. J. Silbey, J. Chem. Phys. 115, 9266 (2001).

Chapter 2

A practical introduction to nonlinear vibrational spectroscopy

2.1 Introduction

The pinnacle of condensed phase reaction dynamics is to observe how molecular dynamics affects reactivity. Understanding how molecules interact with their surrounding solvent, fluctuate in position and how excess energy is dissipated, are all necessary to put together a comprehensive picture of chemistry on the molecular level. As imaging at the sub-Angstrom level with time resolution on the timescale of nuclear motion (i.e. femtoseconds) is currently impossible, chemists have long used spectroscopy to gain information about these dynamics. Vibrational spectroscopy, which is the focus of this thesis, is particularly powerful because the frequencies of molecular vibrations are highly dependent on their local environment.

One can begin to understand how spectroscopic lineshapes are sensitive to molecular dynamics by considering a classical analogy. Envision a collection of anharmonic springs with each spring meant to represent a relatively local molecular vibration. Isolated from each other, each spring has an identical force constant and therefore an identical natural frequency. Interactions with neighboring springs are capable of altering the force constant, such couplings lead to shifts in the frequencies of the springs. Now imagine that we are able to coherently drive all the springs instantaneously. This coherent, macroscopic vibration of the ensemble of springs will rapidly dephase due to a number of processes and is known as a free induction decay. An inhomogeneous distribution of spring frequencies (caused by a distribution of coupling strengths to other springs) will cause the coherent oscillation to decay away at a rate that is related to the breadth of the inhomogeneous distribution of frequencies. Figure 2.1 shows this example. Dephasing of the coherent oscillation also results from pure dephasing, the introduction of random phase shifts in the oscillations of individual springs and spectral diffusion which is the changing of the oscillator's frequency due to time dependent changes in coupling to other springs. Spectral diffusion can be quantified though a frequency autocorrelation function:

$$C(t) = \langle \delta\omega(0)\delta\omega(t) \rangle$$

where $\delta\omega(t) = \omega(t) - \langle \omega \rangle$.

Linear spectroscopy, such as an absorption measurement that one might conduct with an FTIR spectrometer, is very similar to the above example. In this case, infrared radiation acts as a molecular hammer that coherently excites molecular vibrations. These tiny springs are actually tiny dipoles that radiate at the frequency of vibration. Fourier transformation of the resulting free induction decay yields the one dimensional spectral line shape. The one dimensional line shape is incapable of distinguishing what processes lead to the free induction decay. Nonlinear spectroscopy is capable of revealing the mechanism.[1]

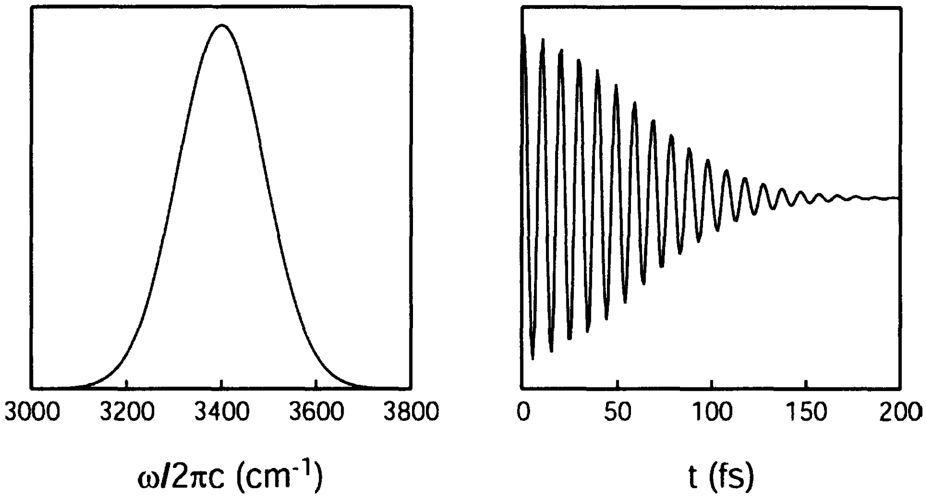

Figure 2.1. Free induction decay for an inhomogeneous distribution of oscillators. The left panel shows the distribution of spring frequencies. The right panel shows the dephasing that results from the coherent excitation of the springs.

2.2 Formalism of nonlinear spectroscopy

So what makes a spectroscopy nonlinear?[2] Quite simply, a spectroscopy is nonlinear if the signal field does not depend linearly on the excitation field. Linear spectroscopies refer to such processes as absorption and reflectance and generally involve weak excitation fields. Nonlinear spectroscopies involve multiple interactions between the excitation fields and the sample. One useful consequence of this is that nonlinear techniques are capable of producing new optical frequencies different from the ones that impinge on the sample, as occurs in harmonic generation.

Our focus will be on third order spectroscopies, also known as four wave mixing experiments. In these experiments three input fields generate a fourth field, the signal field. Given that photons have momentum, the nonlinear signal that is emitted by the sample is in the phased matched directions of $\pm\mathbf{k}_a \pm\mathbf{k}_b \pm\mathbf{k}_c$ where $\mathbf{k}_i$ is the wave vector of pulse *i*. This polarization corresponds to an ensemble of vibrational oscillators that have been coherently driven through the field-matter interactions. The third order polarization, $\mathbf{P}^{(3)}(t)$, can be expressed:

$$\mathbf{P}^{(3)}(t) = \int_0^\infty dt_3 \int_0^\infty dt_2 \int_0^\infty dt_1 \mathbf{R}(t_3,t_2,t_1)\mathbf{E}(t-t_3)\mathbf{E}(t-t_3-t_2)\mathbf{E}(t-t_3-t_2-t_1)$$

where $\mathbf{R}(t_3,t_2,t_1)$ is the response function of the system, **E** refers to the electric field of the incident pulses and t_1, t_2, and t_3 refer to the timings of the field-matter interactions. **R** describes the interaction between the electric fields and the transition dipole of the molecular vibration, μ. Figure 2.2 illustrates the timings for different types of third order experiments. Referring to Figure 2.2a, the time delays between the first and second and between the second and third pulses are known as the evolution (τ_1) and waiting (τ_2) periods, respectively. The time delay between the third pulse and the detection of the signal field is known as the detection (τ_3) time period. The broad bandwidth of the excitation pulses in conjunction with the fact that there are three pulses results in the probing of the v=0, 1, and 2 levels of the vibrational oscillator. Feynman diagrams are pictorial representations used to keep track of the different states that can be prepared by the excitation pulses and that can contribute to the response function. Figure 2.3 depicts the Feynman diagrams for the three level vibrational system assuming collection of the signal in the phase matching direction of $\mathbf{k}_{sig} = -\mathbf{k}_a + \mathbf{k}_b + \mathbf{k}_c$.

(a) Definition of time delays for 3rd order spectroscopy

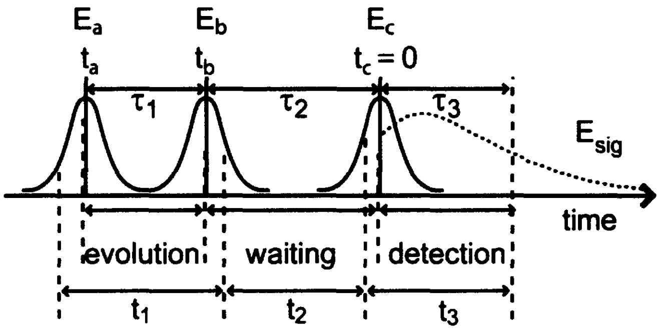

(b) Echo peak shift: primarily sensitive to spectral diffusion

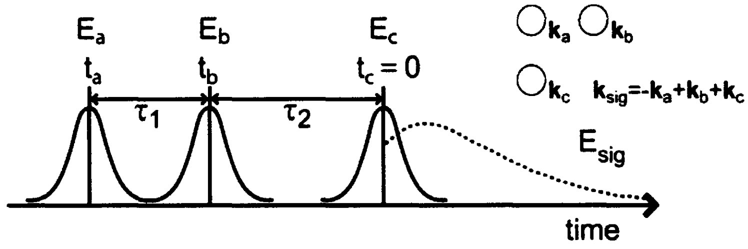

(c) Pump-probe: primarily sensitive to population relaxation

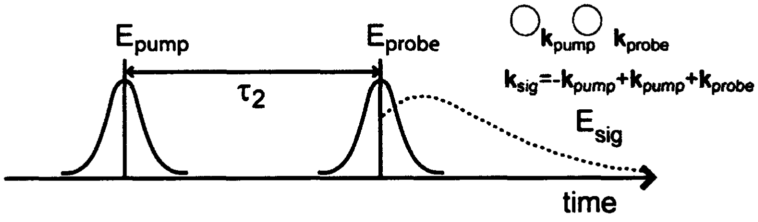

(d) 2D IR: primarily sensitive to couplings & spectral diffusion

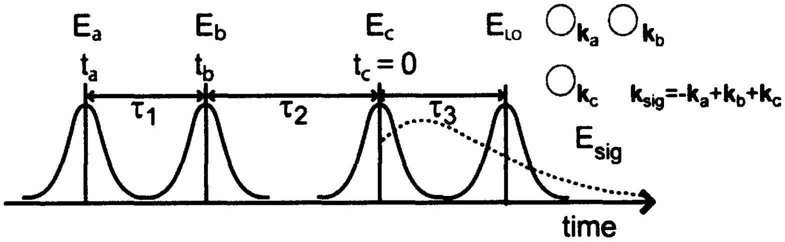

Figure 2.2. Pulse orderings and phase matching geometry for common third order nonlinear spectroscopies. Phase matching expressions indicate the signal collection direction. (a) Definition of time delays in third order spectroscopy. (b) Pulse ordering for an echo peak shift measurement, τ_1 is scanned for a fixed value of τ_2. (c) Pulse ordering for a pump-probe experiment. Only τ_2 needs to be scanned. (d) Pulse ordering for the 2D IR experiment. Time delays τ_1 and τ_3 are scanned for a fixed value of τ_2.

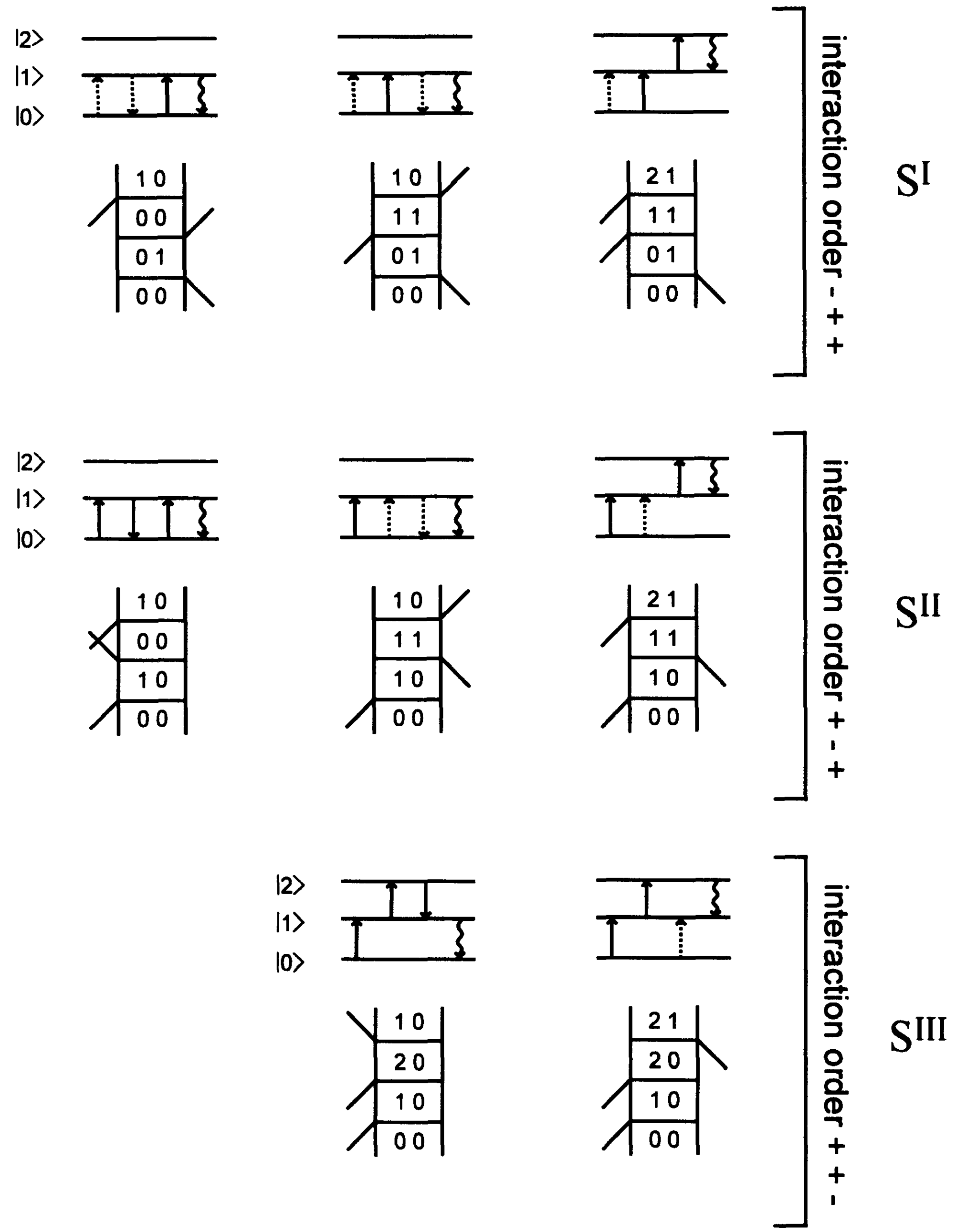

Figure 2.3. Feynman and ladder diagrams for a three level system. S^{I}, S^{II}, and S^{III} refer to the subset of diagrams and correspond to rephasing, nonrephasing and two-quantum diagrams, respectively.[3]

Examination of the Feynman diagrams shows that classes of diagrams differ in their interaction ordering. Therefore controlling the timings between the excitation pulses results in the selection of a subset of diagrams. There are three classes of diagrams that need to be considered: rephasing (S^{I}), nonrephasing (S^{II}), and the two-quantum (S^{III}) diagrams.[4] The two quantum diagrams only result when all three excitation pulses overlap in time. The response function is a sum over the different Feynman diagrams. Sung and Silbey derived analytical expressions for the response functions of each Feynman path.[5] Using the cumulant approximation which assumes that the frequency fluctuations are Gaussian, these are expressed in terms of two point frequency correlation functions, $C(t)$.

The rephasing diagrams can be understood qualitatively by considering the famous classical analogy of runners on a track.[6] From this perspective, individual vibrational oscillators are runners with the first excitation pulse corresponding to the starting gun. The runners run with a distribution of velocities, equivalent to an inhomogeneous distribution of vibrational frequencies. With the second gun (excitation pulse) the runners stop and stand in place and wait. During the waiting time the runners are capable of forgetting how fast they were running. At the firing of the third gun, they turn around and run back towards the starting line. If all the runners maintain their initial velocities they will rephase perfectly back at the starting line and therefore removing the normal dephasing resulting from inhomogeneity. If, however, the runners change their velocities during the course of their running they will not all arrive back at the starting line at the same time. For vibrational oscillators, a change in the runner's velocity corresponds to a change in frequency (i.e. spectral diffusion). From a quantum mechanical perspective (see Figure 2.4), the first excitation creates a coherent superposition state that evolves at the frequency of the energy gap between the ground and excited vibrational levels. The second pulse creates a stationary population state while the third pulse creates an additional coherent state 180° out of phase from the initial state. The echo signal is related to the frequency memory and oscillates at $e^{i\omega_1 t_1}e^{-i\omega_3 t_3}$. Spectral diffusion results in a decrease in the inhomogeneity and the intensity of the echo signal.

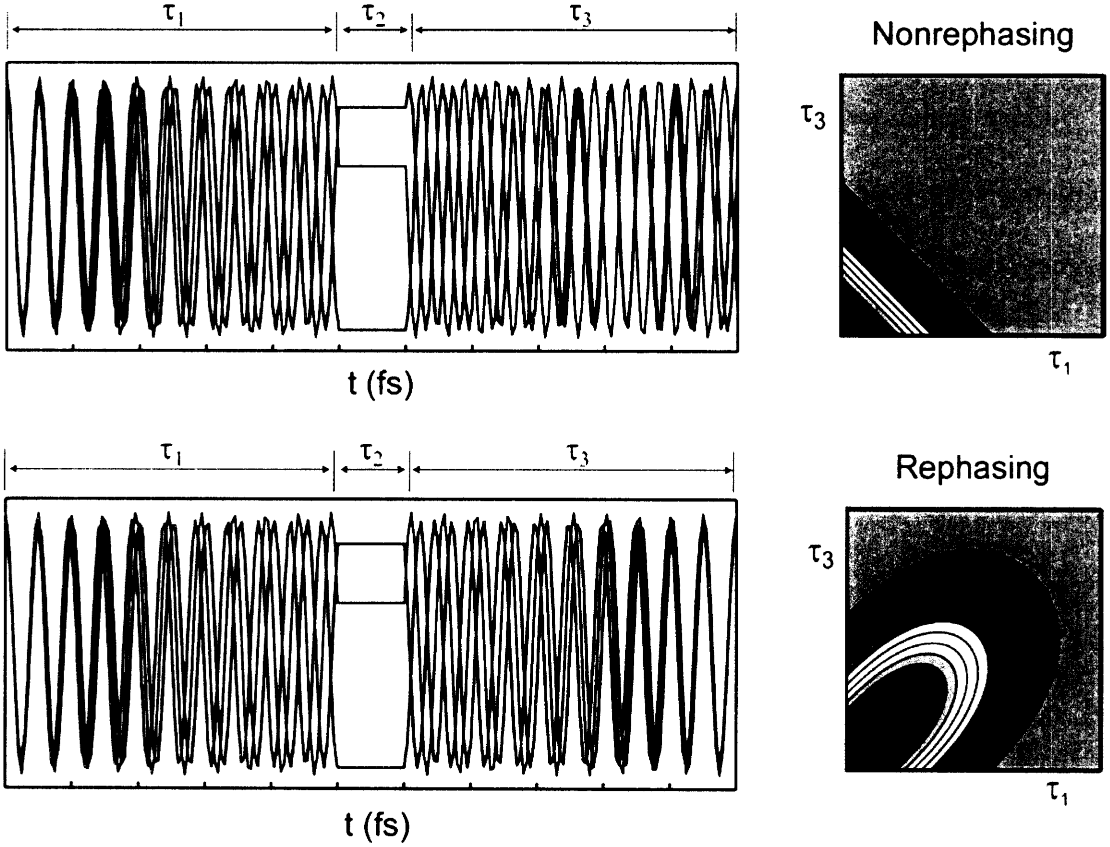

Figure 2.4. (Color) Time dependent evolution of the nonrephasing and rephasing signals, assuming perfect frequency memory. Different colors refer to different frequencies of oscillators taken from the static distribution. The difference in the sign of the phase accumulated in τ_3 results in qualitatively different rephasing and nonrephasing signals. These differences disappear with the loss of frequency correlation.

In the nonrephasing process (see Figure 2.4), the two coherent states in the first and third time periods are of the same phase, $e^{-i\omega_1 t_1}e^{-i\omega_3 t_3}$. Classically this corresponds to the runners always running the same direction around the track. Therefore the nonrephasing signal resembles a free induction decay with increasing inhomogeneity resulting in a faster decay of the nonrephasing signal.

2.3 Vibrational echo peak shift spectroscopy

Echo techniques are the most sensitive to the loss of frequency memory. Vibrational echo peak shift (PS) measurements provide the most direct way quantify frequency fluctuations and have been used to probe both electronic and vibrational systems.[1,7,8] In PS experiment three excitation beams generate the signal field which is emitted in the background free direction of $\mathbf{k}_{sig} = -\mathbf{k}_a + \mathbf{k}_b + \mathbf{k}_c$. The signal field is integrated over the τ_3 time period and is therefore only measured as a function of τ_1 and τ_2:

$$I_{echo}(\tau_1,\tau_2) = \int_0^\infty d\tau_3 \left|\mathbf{P}^{(3)}(\tau_1,\tau_2,\tau_3)\right|^2 .$$

Given this phase matching geometry, rephasing and nonrephasing responses are collected with different excitation pulse orderings. Rephasing signals are generated at positive τ_1 values while the nonrephasing signal generation is only possible at negative τ_1 times.

As noted earlier, it is the rephasing diagrams that are highly dependent on the frequency memory. The runners on a track analogy shows that the peak of the rephasing signal or echo should occur when τ_1 is equal to τ_3. The top panel of Figure 2.5 shows a nonlinear response function calculation of the rephasing signal along the τ_3 axis for different values of τ_1. As anticipated, the echo signal peaks at the τ_3 value corresponding to the value of τ_1. The overall signal level eventually starts to decrease with increasing τ_1 due to spectral diffusion that can occur during τ_1 and τ_3. The bottom panel shows the observable of the PS measurement, which is collected by scanning τ_1 for a fixed value of τ_2. Integrating over τ_3 results in the peak of the echo signal occurring at positive τ_1 times. The shift in the echo maximum is known as the echo peak shift. It decays with increasing τ_2 as frequency memory is lost due to spectral diffusion.

In practice the echo PS measurement is often conducted in a triangle phase matched geometry and two signals $\mathbf{k}_+$ and $\mathbf{k}_-$ are collected separately. This experimental geometry is shown in Figure 2.6. The two signals are equivalent under exchange of the *a* and *b* indices and thus are symmetric about $\tau_1 = 0$ axis. The peak shift is equal to half the separation between the maxima of the two signals. This eliminates any problems caused by errors in setting the $\tau_1 = 0$ timing. Such errors could otherwise lead to misleading results such as long-lived inhomogeneity.

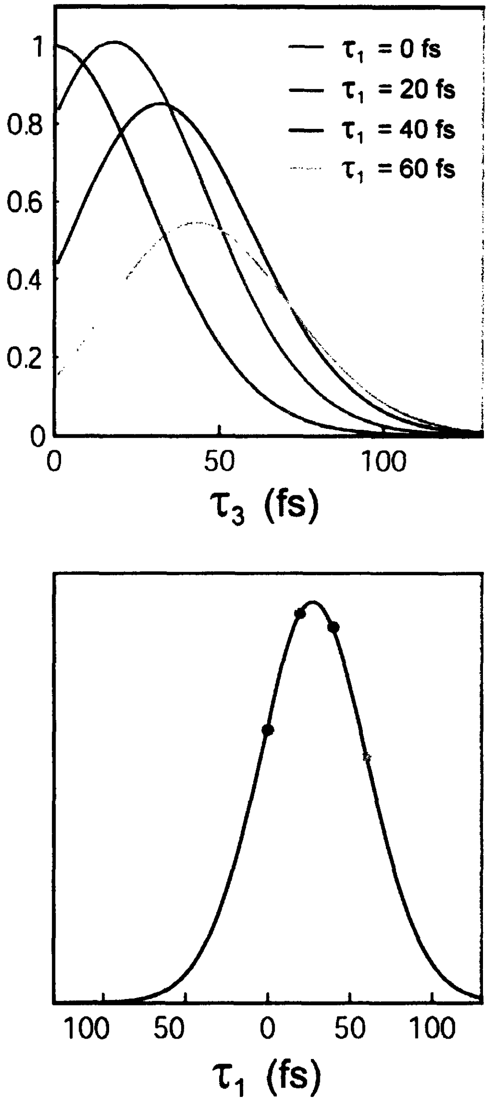

Figure 2.5. (Color) A nonlinear response calculation of the vibrational echo signal using the parameters of the OH stretch of HOD in D_2O (see Chapter 4 for details) as inputs and with $\tau_2 = 0$ fs. The top panel shows echo slices for a fixed value of τ_1. The bottom panel shows the echo signal as it is measured in the experiment. The colored dots correspond to the slices shown in the top panel. The echo maximum is shifted off of $\tau_1 = 0$ fs indicating frequency memory.

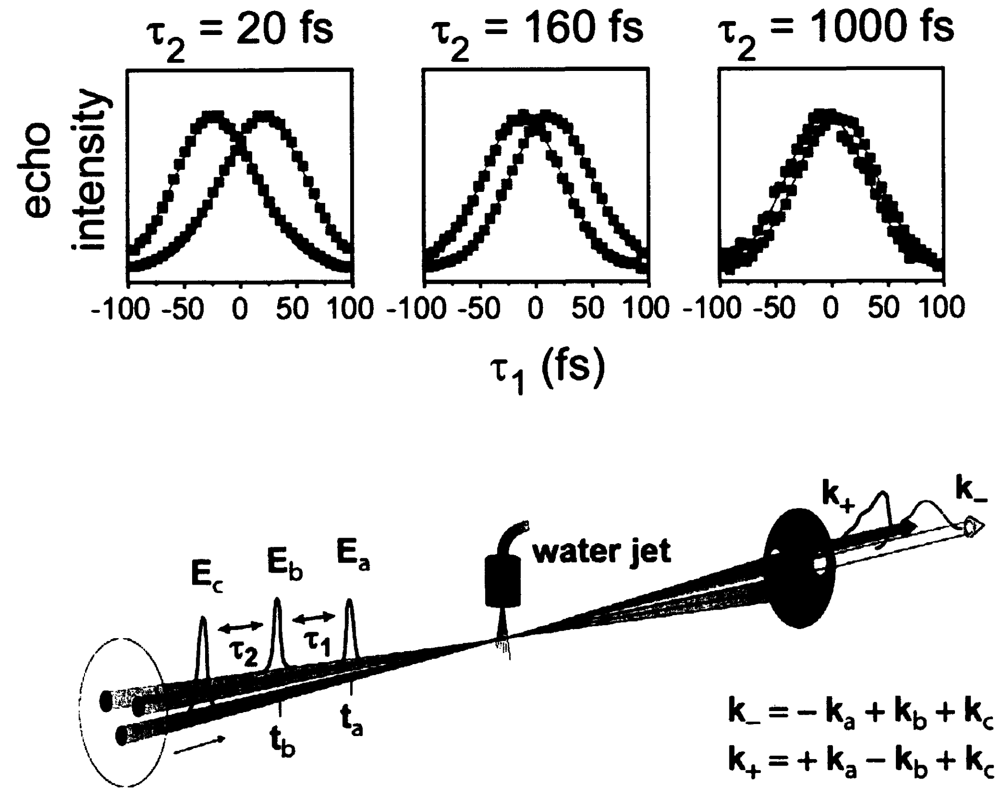

Figure 2.6. (Color) Experimental acquisition of vibrational echo peak shifts where the subscripts a, b and c refer to the excitation pulse's wave vector. The top panels show vibrational echoes of the OH stretch of HOD in D_2O as a function of τ_2 and illustrate the symmetry of the $\mathbf{k}_+$ and $\mathbf{k}_-$ signals about $\tau_1 = 0$.[9]

2.4 Pump-probe spectroscopy

Pump-probe spectroscopy is a third order experiment involving only two excitation beams. The decay of the pump-probe signal is primarily sensitive to vibrational population dynamics. In the limit of delta function pulses, two field-matter interactions come from the pump beam that act to instantaneously create a population state (i.e. τ_1=0) while the third interaction from the probe beam acts to interrogate this population with

τ_3=0. The signal field is emitted along the direction of the probe beam. This interference between the signal and probe beams is known as heterodyne detection. It provides both amplitude and phase information of the signal that allows one to distinguish the positive going signal due to the transient bleach(v=0→1) and stimulated emission (v=1→0) from the negative going transient absorption at the frequency of v=1→2. Population relaxation out of the v=1 excited state and subsequent refilling of the ground state hole results in the simultaneous decrease of both the transient bleach and absorption as one scans the τ_2 time delay between the pump and probe pulses. Disappearance of the transient absorption along with the persistence of the bleach indicates that the ground state hole is not being repopulated and that the intermediate state is spectroscopically distinct from the original ground state. While pump probe measurements are most sensitive to population relaxation, finite pulse durations result in coherent contributions because the system is allowed to evolve in τ_1 on the order of the pulse length.[10]

One is capable of probing molecular reorientation using polarization-selective pump probe measurements. The population created by the pump beam is an anisotropic *cos*^{2} distribution resulting from the lab to molecular frame projections of the two field-matter interactions. By varying the polarization of the probe, one is able to watch the randomization of this oriented ensemble of dipoles, while separating the contribution from population relaxation. The anisotropy calculated from the ratio of signal intensities given parallel, $S_{\|}(\tau_2)$, and perpendicular, $S_{\perp}(\tau_2)$, probe polarizations:

$$r(\tau_2)=\frac{S_{\|}(\tau_2)-S_{\perp}(\tau_2)}{S_{\|}(\tau_2)+2S_{\perp}(\tau_2)}.$$

quantifies molecular reorientation.[11] Chapter 4 presents polarization-selective pump probe measurements of the OH stretch of HOD in D_2O.

2.5 2D IR spectroscopy

Multidimensional or two-dimensional infrared (2D IR) spectroscopy is an optical analog of multidimensional NMR methods. 2D IR goes a step beyond homodyne echo experiments by measuring the amplitude and phase of the signal field directly. As in the pump-probe experiment this is accomplished through heterodyne detection. Here the signal is interfered with a known reference field, called the local oscillator. A 2D time domain surface is constructed by collecting a grid of τ_1 vs. τ_3 points for a fixed value of τ_2. Double Fourier transformation of the τ_1 and τ_3 axes yields the 2D frequency domain spectrum with axes ω_1 and ω_3.

Double Fourier cosine transformation of the rephasing and nonrephasing spectra yields phase twisted line shapes that result from the mixing of real and imaginary parts (see Figure 2.7). This is a well-known effect in multidimensional NMR.[12] The difference in the sign of the phase between τ_1 and τ_3 causes the rephasing and nonrephasing line shapes to be tilted in different directions. Rephasing spectra oscillate at $(\mp\omega_1, \pm\omega_3)$ while nonrephasing spectra are at $(\pm\omega_1, \pm\omega_3)$ in the Fourier plane. Mirror reflection of the rephasing spectrum and subsequent summation of the rephasing and nonrephasing spectra cancels the dispersive tails of the individual line shapes resulting in the purely absorptive correlation spectrum (see Figure 2.7).[13,14]

The 2D IR correlation spectrum can be understood in terms of a double resonance (hole-burning) experiment. In a double resonance experiment, one burns spectrally narrow holes into the absorption line shape with the pump pulse. After waiting a time, τ_2, this distribution is interrogated with a broadband probe pulse. In a 2D correlation spectrum one creates a coherent superposition of oscillators in τ_1. This ensemble is allowed to evolve in τ_2 and is then probed in τ_3. In this way, one correlates the frequency of oscillation in τ_1 with τ_3. The frequency axes of the 2D IR spectrum ω_1 and ω_3 correspond to the ω_{pump} and ω_{probe} axes of the double resonance experiment. The important difference between the 2D IR experiment and the double resonance experiment is that in the latter the experimentalist chooses the frequency and time resolution of the pump pulse while in the 2D IR experiment the time resolution is set by the dephasing of the molecule. In this way, the 2D IR experiment automatically obtains the maximum time resolution physically possible.

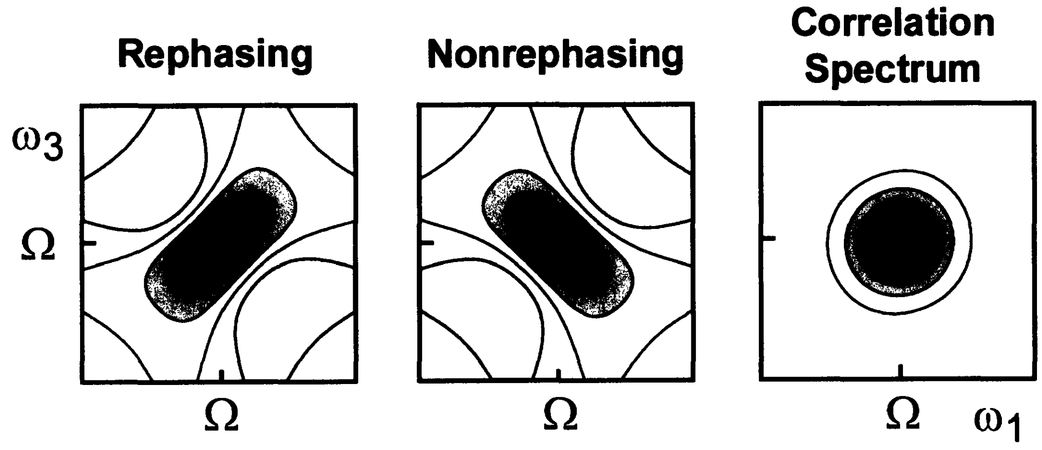

Figure 2.7. (Color) Plot of the real part of the rephasing and nonrephasing Fourier transform for a two-level system. The addition of the rephasing and nonrephasing spectra results in the correlation spectrum, which is purely absorptive.

Molecular vibrations are inherently multilevel systems. Perusing the Feynman diagrams in Figure 2.3 shows that for some diagrams the system is oscillating between v=1 and 2 in the detection period. Thus two peaks are present in the 2D IR spectrum corresponding to the v=0→1 transition and the anharmonically shifted v=1→2 transition.

The waiting time dependence of the correlation spectra reveals spectral diffusion of vibrational oscillators. In the inhomogeneous limit 2D IR line shapes are diagonally elongated, indicating that oscillators are at the same frequencies in the τ_1 and τ_3 time periods. At the other extreme, in the homogeneous limit, oscillators sample the breadth of the frequency distribution during the waiting time. This results in a 2D line shape that is more symmetric. Figure 2.8 illustrates these two limits. Chapter 5 details the waiting time dependence of 2D line shapes and how this evolution is related to the intensity weighting of rephasing and nonrephasing spectra.

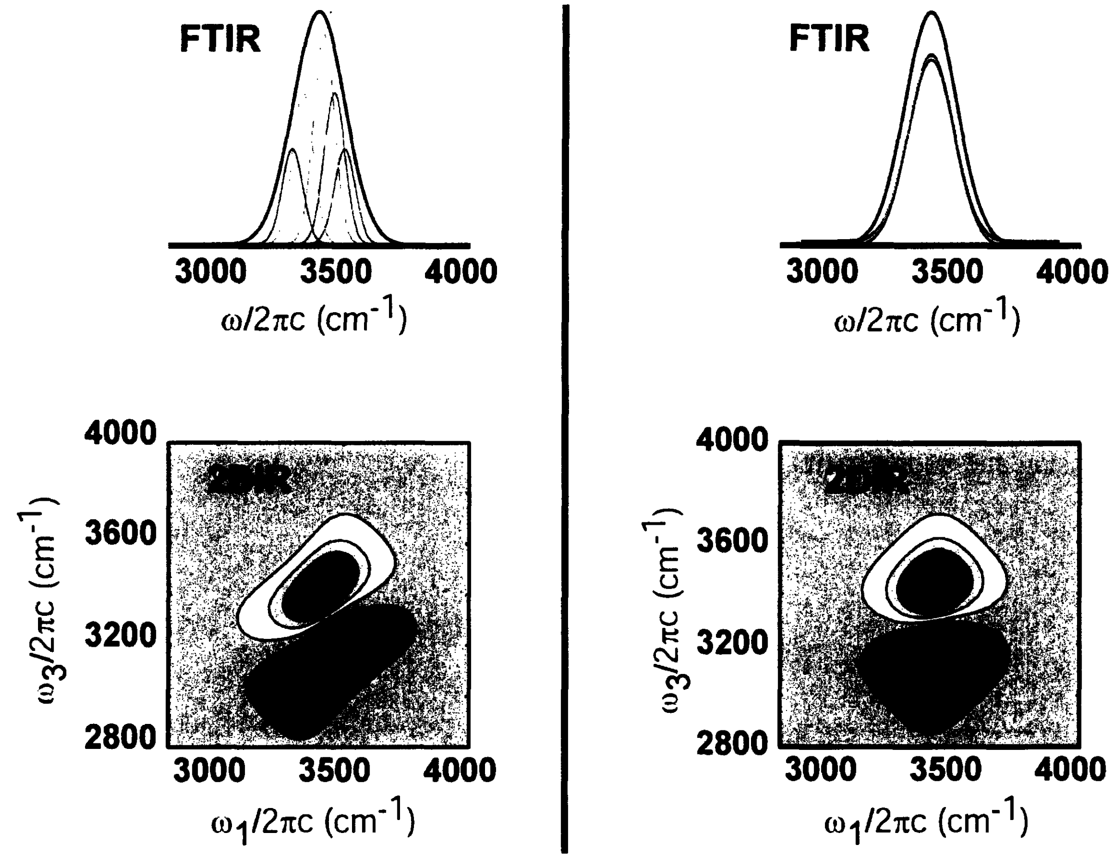

Figure 2.8. (Color) FTIR absorption and 2D IR spectra for a three level vibrational system in the inhomogeneous (left panel) and homogeneous (right panel) limits. Note that the FTIR spectra are identical in both cases but that the 2D line shape is able to distinguish the line broadening mechanism.

References

1 T. Joo, Y. Jia, J.-Y. Yu, M. J. Lang, and G. R. Fleming, J. Chem. Phys. 104, 6089 (1996).

2 S. Mukamel, Principles of Nonlinear Optical Spectroscopy. (Oxford University Press, New York, 1995).

3 C. J. Fecko, J. J. Loparo, S. T. Roberts, and A. Tokmakoff, J. Chem. Phys. 122, 054506 (2005).

4 M. Khalil, N. Demirdoven, and A. Tokmakoff, Journal of Physical Chemistry A 107 (27), 5258 (2003).

5 J. Sung and R. J. Silbey, J. Chem. Phys. 115, 9266 (2001).

6 E. L. Hahn, Phys. Today 6, 4 (1953).

7 P. Hamm, M. Lim, and R. M. Hochstrasser, Phys. Rev. Lett. 81, 5326 (1998).

8 W. P. de Boeij, M. S. Pshenichnikov, and D. A. Wiersma, Annu. Rev. Phys. Chem. 49, 99 (1998).

9 C. J. Fecko, J. D. Eaves, J. J. Loparo, A. Tokmakoff, and P. L. Geissler, Science 301, 1698 (2003).

10 D. A. Farrow, A. Yu, and D. M. Jonas, J. Chem. Phys. 118, 9348 (2003).

11 H. Graener, G. Seifert, and A. Laubereau, Chem. Phys. Lett. 172, 435 (1990).

12 R. R. Ernst, G. Bodenhausen, and A. Wokaun, Principles of Nuclear Magnetic Resonance in One and Two Dimensions. (Oxford University Press, Oxford, 1987).

13 M. Khalil, N. Demirdöven, and A. Tokmakoff, Phys. Rev. Lett. 90, 47401 (2003).

14 J. D. Hybl, A. A. Ferro, and D. M. Jonas, J. Chem. Phys. 115, 6606 (2001).

Chapter 3

Acquisition of high fidelity 2D IR line shapes

3.1 Introduction

Chemistry in the condensed phase is determined by the forces between reacting molecules and their interactions with the surrounding solvent. The experimental observation of reaction dynamics in liquids is difficult due to the fast molecular timescales (fs to ps) of most chemical reactions and the need to have a structurally sensitive probe. Multidimensional infrared spectroscopy is becoming a popular technique because of its ability to address these experimental issues. Molecular vibrations are particularly sensitive to their surrounding environment while improvements in ultrafast laser technology allows for routine generation of ~100 fs mid-IR pulses. Vibrational frequencies are determined by intramolecular couplings between vibrations within the same molecule and intermolecular couplings between the vibration of interest and the surrounding solvent or another solute molecule associated with it. Time-dependent changes in frequency are then due to changes in coupling.

As a correlation spectroscopy, two dimensional infrared (2D IR) spectroscopy provides an intuitive way to extract these couplings. Like other vibrational echo spectroscopies, 2D IR probes the third order material response function. Three excitation beams impinge upon the sample, generate a signal field that is overlapped with a fourth local oscillator (LO) field in order to obtain amplitude and phase information. Three time intervals result from the delays between the four pulses as shown in Figure 3.1. These delays are known as the evolution (τ_1), waiting (τ_2) and detection (τ_3) periods. Conceptually, the 2D IR spectrum can be understood as a correlation map relating the frequency labeled in τ_1 with the frequency measured in τ_3 after waiting a time τ_2. Couplings between vibrations are revealed as cross peaks while spectral diffusion resulting from fluctuations of the solvent appear as τ_2 dependent changes in the 2D IR line shapes.

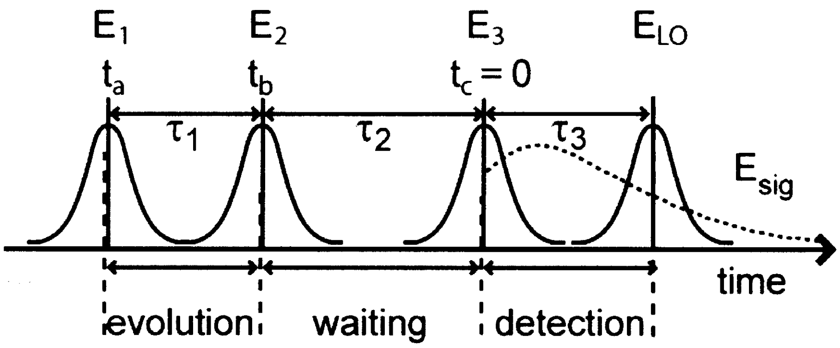

Figure 3.1. Pulse sequence for 2D IR spectroscopy.

Acquisition of high fidelity 2D line shapes is essential in order to obtain useful information from 2D IR experiments. This is especially critical for water where non-Gaussian frequency fluctuations are revealed as asymmetries in the 2D line shape that evolve with the waiting time.[1,2] Accurate extraction of the real part of the material response is essential for quantitatively analyzing these subtle effects. Likewise, for many relevant vibrational systems, the coupling between vibrations is on the order of a few wavenumbers and thus the accurate extraction of frequencies and the frequency splittings between peaks is crucial. Models of vibrational coupling, such as transition dipole coupling, can then be applied to extract information on molecular structure from the experimental 2D spectrum. This procedure has been recently applied to proteins and DNA.[3,4]

Up to this point, 2D IR spectra have been obtained using three different experimental collection schemes. One can scan both the τ_1 and τ_3 time variables, here after referred to as time/time scanning. In this approach, the LO acts to gate the signal field. Double Fourier transformation of the τ_1 and τ_3 axes yields the 2D frequency domain spectrum. In another approach, the Fourier transform of the τ_3 axis can be obtained optically in a monochromator by dispersing the signal/LO beam to measure ω_3 directly (time/frequency scanning) and thus eliminating the need to scan the τ_3 delay. Here one obtains phase information of the signal field through spectral interferometry with the LO.[5,6] Additionally, others have utilized a dual frequency/frequency approach in which ω_1 is set by a narrow pump beam whose frequency is then tuned while ω_3 is measured with a broadband probe that is subsequently dispersed in a monochromator.[7] In this approach the signal is emitted in the same direction as the probe beam and is therefore self-heterodyned. A recent paper by Hamm and coworkers discusses the many similarities between the frequency/frequency approach and the broadband echo methods.[8] While quite powerful, the frequency/frequency approach will not be discussed here because of two limitations compared to its broadband counterparts: (1) the experimentalist must set the frequency resolution (and therefore the time resolution) of the narrowband pump pulse and (2) one can only acquire the real part of the 2D spectrum. In the broadband time/time and time/frequency approaches the frequency resolution is set by the dephasing of the vibration. The time and frequency resolution is limited only by the molecular system, resulting in the highest time resolution possible. Broadband echo spectra are able to view the real and imaginary parts of the rephasing and nonrephasing spectra because time ordering of the excitation pulses allows for the separate collection of different Liouville pathways. As explored in Chapters 5 and 6 frequency memory is quantified in the ratios of these different pathways.

Accurate extraction of the spectral phase from Fourier transform spectroscopy requires phase stability between the pulses used in the experiment and sub-wavelength (i.e. better than $\lambda/10$) control over their time delays. A linear drift in the phase across the 2D surface during data collection results in a frequency shift proportional to the rate at which the phase is changing. This frequency shift appears in the slow scanning dimension. For example, if one were collecting a time/time surface by scanning the τ_3 axis and then stepping τ_1, the frequency shift would appear in ω_1 dimension. Figure 3.2 displays nonlinear response function calculations of 2D IR spectra of the OH stretching transition of HOD in D_2O for $\tau_2=0$ fs. We use our measured frequency correlation function described in Chapter 4, as an input. The top panel of Figure 3.2 depicts the ideal 2D IR spectrum unadulterated by experimental complications. Two peaks are visible, one positive going due to the transient bleach of the 0→1 transition and one negative peak due to the transient absorption of the anharmonically shifted 1→ 2 transition. The diagonal elongation of the line shape is consistent with frequency memory. The middle panel of Figure 3.2 depicts a 2D surface in which a linear phase shift has been applied along the τ_1 dimension. The phase was applied by modulating the τ_1 time axis, $\tau_1^* = \tau_1 + \Delta\tau_1$, where τ_1^* is the measured time axis, τ_1 is the actual time axis, and $\Delta\tau_1$ is the error. A linear phase drift is equivalent to a regular error in the τ_1 step size. We set $\Delta\tau_1 = 0.05$ fs for a 2 fs step, corresponding to 2.5% error over the length of a 3 μm fringe. This results in the 2D line shape being shifted by 85 cm^{-1} in the ω_1 dimension.

Distortions to the line shape arise from nonlinear changes in the phase as a function of time delay. Such changes in the phase can result from systematic changes in the excitation beam pointing or most commonly due to inaccuracy in the time delays between pulses. Even a small but periodic change in the phase can lead to major distortions in the 2D line shape. The bottom panel of Figure 3.2 displays a 2D surface with a periodic error in the time axis with a magnitude of +/- 10% of the carrier periodicity. Clear ghost peaks are observed that are shifted in frequency from the carrier by the periodicity of the error.

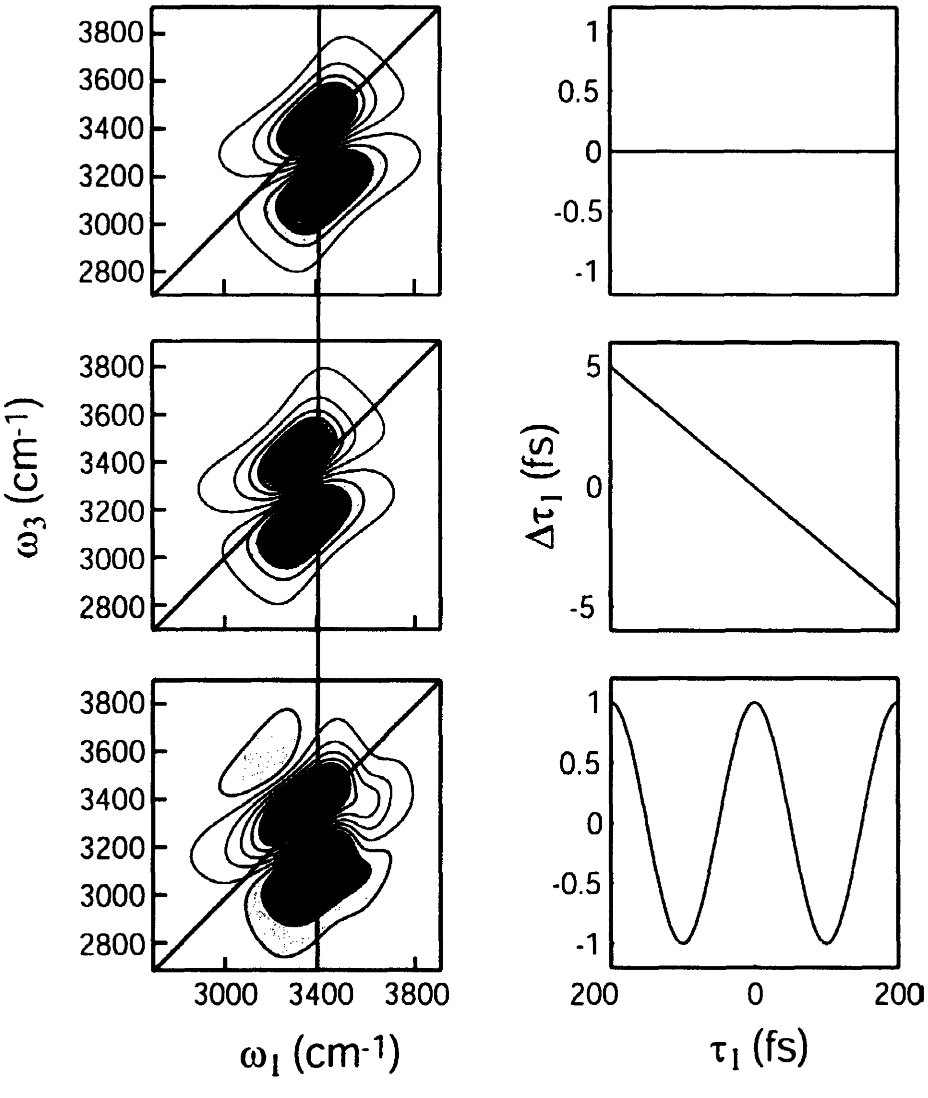

Figure 3.2. (Color) Calculations of 2D IR spectra of the OH stretch of HOD in D_2O with varying phase distortions. The rightmost panels depict the phase applied to the time domain 2D spectra along the τ_1 axis prior to Fourier transformation.

The three excitation beams and the local oscillator field are all derived from the same IR pulse so that they have a well defined phase relationship. Traditionally this has been accomplished in interferometers that rely upon beam splitters to separate the initial IR beam into four replicas. Retroreflecting mirrors mounted on mechanical translation stages are used to control the path lengths each beam travels allowing the user to control the time delays between pulses while compensation plates insure that each beam travels through the same amount of material. A lack of common path between the beams through the interferometer coupled with mechanical vibrations or changes in temperature introduces phase noise into the measurement. Errors in the encoder accuracy of the mechanical translation stages can lead to errors in the time axes. Periodic errors commonly occur with translation stages controlled by rotary encoders. These errors are reproducible because they are dependent on where the encoder is in its rotation. Linear encoders act as a ruler in which the stage reads its position. Errors can arise from the interpolation the stage must do when it is in between marks on the encoder.

It has been observed previously that periodic errors in the step size of motorized translation stages result in ghost peaks or distortions of the 2D line shapes upon Fourier transformation. While most problematic in the visible, this effect has been documented in the mid-IR as well. Recent reports have tackled this problem in a variety of ways. During acquisition of a 2D surface, the groups of Jonas[9] and Tokmakoff[10] collected spectral interferograms between the first two excitation pulses in order to correct the τ_1 axis. The groups of Miller and Fleming have developed diffractive-optic-based strategies employing rotating windows or movable glass wedges to control the time delays.[11,12] Such dispersion based approaches are able to provide extremely high accuracy in the time delay (i.e. a few attoseconds) as the wedge (or window) acts to downshift the mechanical stage. Depending on the pulse bandwidth, however, these approaches can add an unacceptable amount of chirp to the excitation pulse and can be limited in the maximum delay that one can generate. This is potentially problematic for narrow resonances whose signal persists for a long time. The groups of Hamm[13] and Cundiff[14] have recently reported an actively stabilized HeNe based interferometer, similar to approaches used in earlier experiments,[15,16] to insure interferometric phase stability.

Proper acquisition of the real part of the absorptive spectrum requires not only knowledge of the relative delays between time steps of the excitation pulses but also their absolute zero timing. Errors in the zero timing result in the mixing of the real and imaginary components of the spectra. To properly obtain the absorptive spectrum, the dispersive parts of the real rephasing and nonrephasing spectra must cancel upon summation. Thus the correlation spectrum is highly sensitive to any errors in the zero timing. An error in the τ_1 timing results in a line shape that appears too inhomogeneous or homogeneous depending on whether the error is positive or negative. One can understand this by considering how the measured echo peak shift changes with an error in setting the $\tau_1=0$ timing. The echo peak shift is the τ_1 value relative to $\tau_1=0$ that corresponds to the maximum of the echo signal projected onto the τ_1 axis. It is a sensitive measure of frequency memory[17,18] and changes in τ_1 timing correspond to artificial changes in frequency correlation. This effect becomes more significant for systems with relatively small peak shifts such as those with fast dephasing and broad line shapes. Figure 3.3 illustrates how $\tau_1=0$ timing errors show up in 2D spectra. The left topmost panel depicts the frequency domain, $\tau_2=0$ spectrum with no timing error, $\Delta_{\tau1=0}=0$. The panel on the right shows the echo peak shift has a value of ~25 fs. The middle panels show the effect of a timing error of one fringe that increases the peak shift by 10 fs. The 2D line shape is narrower in the antidiagonal direction and the tilt between the 0→1 and 1→2 transition has increased. A τ_1 timing error of one fringe in the opposite direction, which acts to decrease the peak shift to 15 fs, has the opposite effect, the line shape is broader and the tilt of the node is less.

The following sections describe two methods that we have successfully applied to measure high fidelity 2D IR line shapes of the OH stretch of HOD in D_2O. Compared to other methods, the present techniques provide superior signal to noise and data acquisition times. Although this description focuses on applying these methods to probing the OH stretching vibration of HOD in D_2O, the techniques described herein are general and relevant to all phase sensitive infrared experiments.

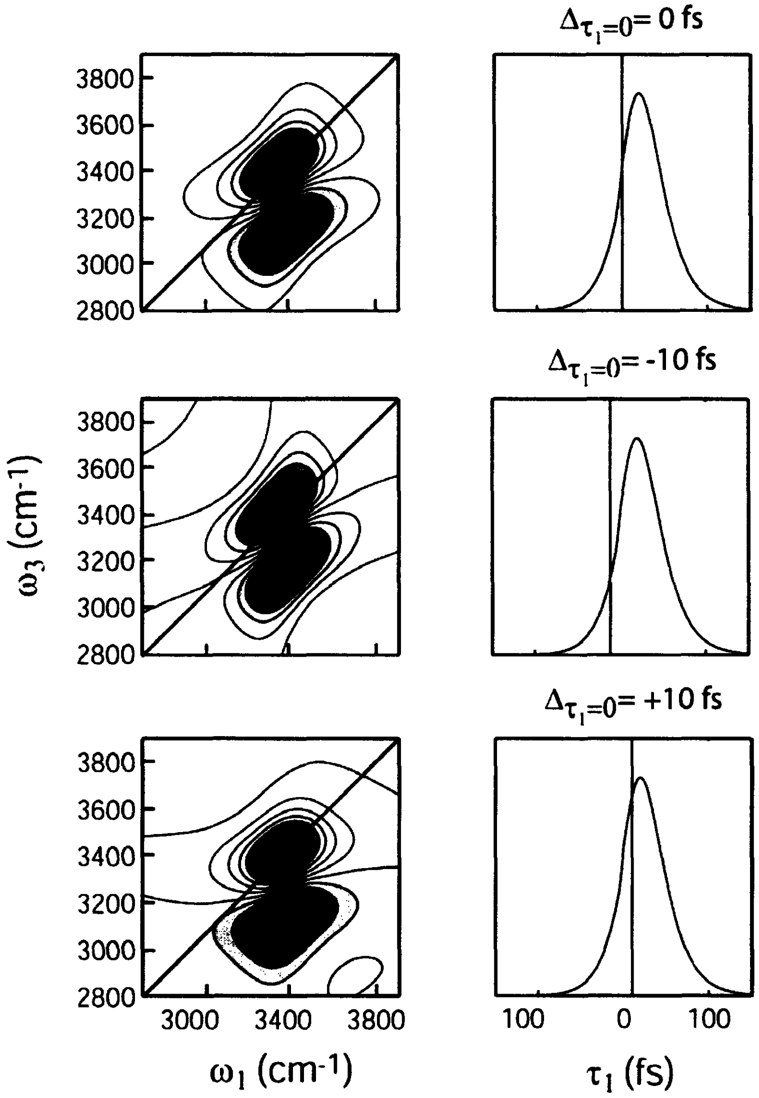

Figure 3.3. (Color) Calculations of 2D IR spectra with τ_2=0 demonstrating the effects of errors in setting the τ_1=0 timing. The rightmost panels depict the vibrational echo peak shift while the line shows where the τ_1=0 point was taken.

3.2 Experimental overview

Figure 3.4 provides an overview of the equipment necessary to collection a 2D IR spectrum. The generation of ultrashort mid-IR pulses is based on Ti:sapphire laser technology. A relatively weak, 5 nJ per pulse, 800 nm pulse train with a repetition rate of 76 MHz, and ~10 fs duration is generated by a Femtolasers Femtosource Scientific Pro Ti:sapphire oscillator pumped by a Nd:YVO_4 Spectra Physics Millennia Vs. The top panel of Figure 3.5 shows the typical oscillator spectrum, which is ~90 nm broad FWHM. However, this spectrum is sensitive to alignment. Before amplification in a Ti:sapphire Femtolasers CompactPro multipass amplifier, the oscillator output is stretched in time to a safe value for amplification by passing through a piece of glass and precompensated for third order dispersion by multiple bounces off of chirped mirrors. Four passes through the amplifier, pumped by a Spectra Physics Evolution X, increases the maximum intensity by a factor 80,000. Further amplification is achieved after pulse picking using a Pockels cell. This reduces the repetition rate to 1 kHz and results in a pulse contrast of >10,000:1. Five additional passes increases the pulse energy to ~ 1 mJ. Gain narrowing in the amplification process reduces the bandwidth of the amplified pulse to roughly ~35 nm, as shown in Figure 3.5. Prior to compression, we spatially filter the beam by focusing into a 50 μm stainless steel wire dye. The spatial filter is placed at the focus of a telescope which increases the beam size to 9 mm and collimates it. The pulse is then compressed by passing through a prism-based compressor. Second harmonic FROG of the output pulse is shown in the middle panel of Figure 3.5. The extracted field and phase is shown in the bottom panel of Figure 3.5 and indicates that the output is approximately 30 fs in duration. A λ/2 waveplate prior to the compressor is used to set the output power by controlling the reflectance loss off of the prisms.

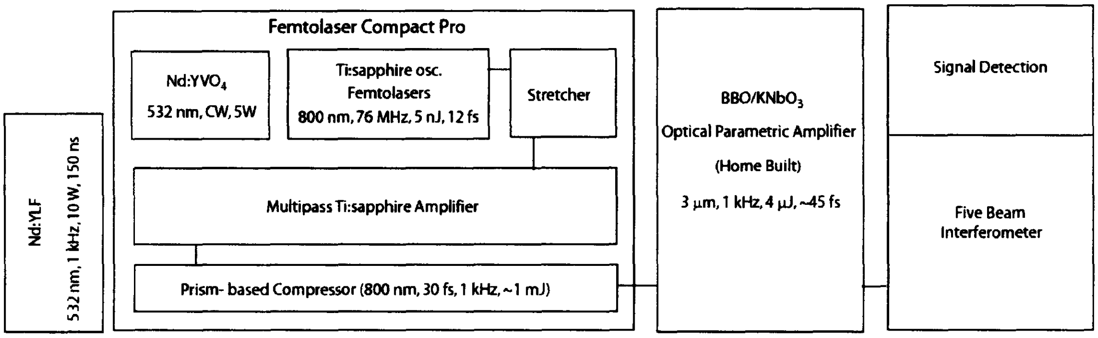

Figure 3.4. (Color) Schematic of the 2D IR experiment. A multipass Ti:sapphire amplifier is used to pump a home-built optical parametric amplifier which generates 45 fs pulses at 3 μm. These IR pulses are then split up into five replicas in the interferometer which allows for the control of their relative time delays and polarizations. These coherent mid-IR pulses are then used to generate and detect a third order signal field emitted from the sample.

2D IR spectroscopy of the OH stretch of HOD in D_2O requires near-transform-limited sub-50 fs pulses to insure enough coherent bandwidth to span the broad OH line shape (~260 cm^{-1} FWHM) and the anharmonically shifted $v=1\rightarrow2$ transition. These ultrafast IR pulses were generated as described previously with a few modifications detailed here.[19] In brief, 540 mW of the Ti:sapphire multipass amplifier was used to pump a home built, two-stage β-Barium Borate/Potassium Niobate (BBO/$KNbO_3$) optical parametric amplifier. Approximately 1% of the 800 nm pump light is focused into a [0001]-cut sapphire plate that generates a white light continuum. The near-IR (i.e. 1.1 μm) from this process is aligned collinearly with ~35% of the 800 nm pump light to generate the first stage of amplification in BBO. BBO was selected due to its high damage threshold and its ease of use. A custom beam splitter designed to transmit 800 nm and reflect the 1.1 μm was used to seed the second pass in $KNbO_3$. The flat tuning curve of $KNbO_3$ near 3 μm results in the large acceptance bandwidth necessary to support short IR pulse durations. However, the relatively large dispersion of $KNbO_3$ limits the crystal length to ~1mm. This dispersion coupled with the flat tuning curve results in a unique property of $KNbO_3$, control of the center wavelength is highly sensitive to the timing between the 800 nm pump beam and the 1.1 μm seed.[20]

The IR beam is collimated at a diameter of 9 mm, which allows for propagation of several meters without significant divergence. A 2 mm thick Ge Brewster plate served to overlap the mid-IR with a mode-matched HeNe alignment beam. It also acts to compress the pulse duration by adding positive second order dispersion that is balanced with the negative dispersion from the remaining optics in the interferometer.[21] Figure 3.6 shows the characterization of the mid-IR light. Second harmonic FROG and autocorrelation measurements indicated that the pulses are ~45 fs in duration, supporting ~400 cm^{-1} of bandwidth (FWHM), and have little higher-order spectral phase. Typical pulse energies are approximately 5 μJ.

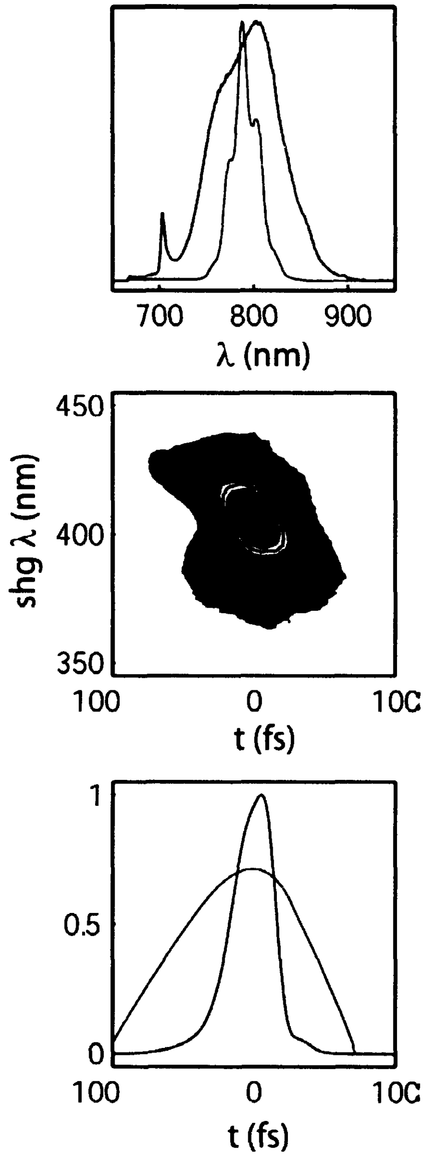

Figure 3.5. (Color) Characterization of the 800 nm excitation. The top panel shows the Ti:sapphire oscillator (blue) and amplifier (green) spectra. The middle panel depicts an SHG-FROG spectrum of the amplified pulse. The bottom panel depicts the extracted amplitude (blue) and phase (green) of the electric field emitted from the amplifier.

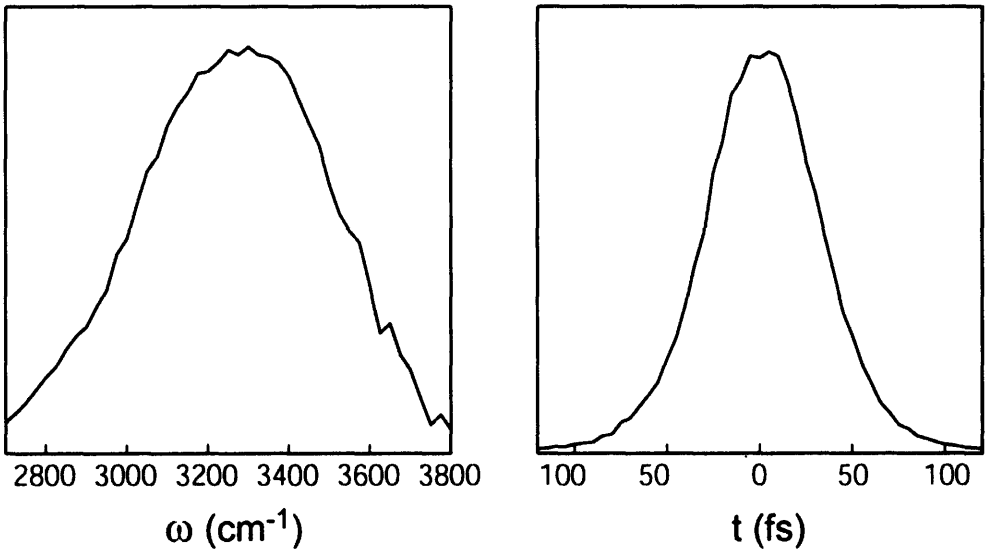

Figure 3.6. Characterization of the mid-IR excitation. The left panel shoes a spectrum of the mid-IR radiation with ~450 cm^{-1} FWHM. The right panel shows a typical second harmonic autocorrelation, corresponding to ~45 fs duration.

3.3 Mach-Zender interferometer

A modified Mach-Zender interferometer with custom 3 μm 50/50 CaF_2 beamsplitters (Thin Film Laboratory), shown in Figure 3.7, served to divide the output of the OPA into three excitation beams, a local oscillator (LO) for heterodyne detection, and a signal tracer beam (T) used for alignment purposes. Each arm contained the appropriate number of CaF_2 compensation plates to balance the material traversed by each beam from the first to final beamsplitter. MgF_2 $\lambda/2$ waveplates (Alphalas) and CaF_2 wire grid polarizers (Molectron) were used to set the polarization of each beam. Gold retroreflecting mirrors mounted on motorized translation stages (Aerotech ANT-25L) controlled the relative pulse delays. Using a 90° bare gold parabolic mirror of 10 cm effective focal length, the three excitation beams were focused in the boxcar geometry to a spot size ($2w$) of 100 μm in the sample, resulting in a signal emitted in the direction of the missing corner of the box ($\boldsymbol{k}_{\mathrm{sig}} = -\boldsymbol{k}_{\mathrm{a}} + \boldsymbol{k}_{\mathrm{b}} + \boldsymbol{k}_{\mathrm{c}}$). Zero timing of the three excitation beams was set by iterative, pairwise, background-free second harmonic autocorrelations, allowing for $\tau_1=0$ and $\tau_2=0$ to be set within ~5 fs. The entire experiment was enclosed and purged with dry air to remove atmospheric water absorption.

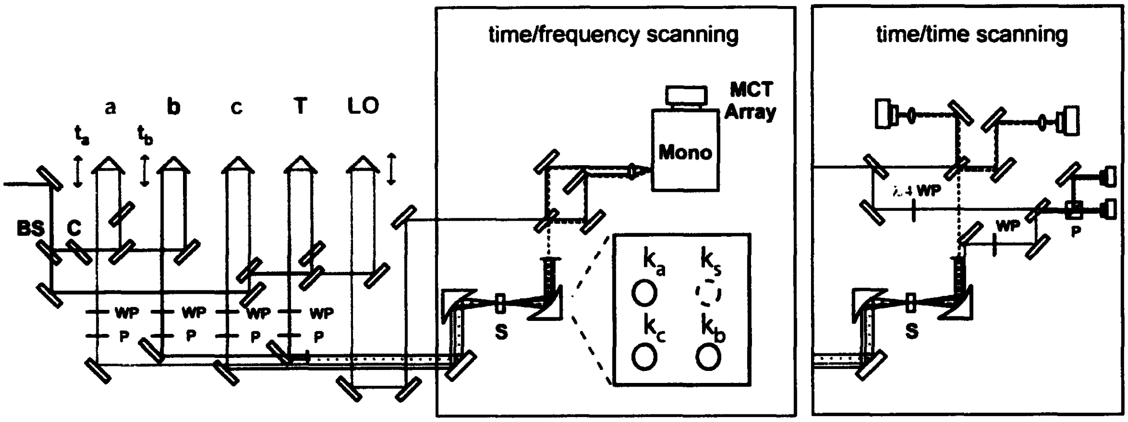

Figure 3.7. (Color) Layout of the five beam interferometer showing the three excitation pulses (**a**, **b**, and **c**), the tracer **T** and the local oscillator field **LO**; BS, 50-50, 3-mm thick CaF_2 thick beam splitter; C, 3-mm thick CaF_2 compensation plate; WP, λ/2 tunable wave plate; P, wire grid CaF_2 polarizer; S, a 50 μm jet of HOD in D_2O; mono, monochromator. The timing of beams **a**, **b**, and **LO** are controlled by calibrated Aerotech translation stages.

Rephasing ($\boldsymbol{k}_R = -\boldsymbol{k}_1 + \boldsymbol{k}_2 + \boldsymbol{k}_3$) and nonrephasing ($\boldsymbol{k}_{NR} = \boldsymbol{k}_1 - \boldsymbol{k}_2 + \boldsymbol{k}_3$) signals were collected separately by controlling the relative pulse time ordering along the $\boldsymbol{k}_a$ and $\boldsymbol{k}_b$ wavevectors. Discrete Fourier transformation (Matlab) of the individually measured 2D spectra yielded the complex rephasing and nonrephasing spectra (S_R and S_{NR}). Subsequent summation gave the complex correlation spectrum ($S_C = S'_C + iS''_C$). Amplitude and phase representations of the 2D IR spectra, defined as $S_A = |S_C|$ and $S_\varphi = \arctan\left(S''_C / S'_C\right)$, were also examined.

The sample of HOD in D_2O was flowed as a 50 μm free-standing jet. The peak optical density of the OH transition was ~0.2, corresponding to roughly a 1% solution of

HOD in D_2O. A jet was used instead of a sample cell to avoid the overwhelming nonresonant response from sample cell windows when all three excitation beams are near time coincident. Previous pump-probe measurements of HOD in D_2O measured in a CaF_2 sample cell are not equal to the signal measured in the jet until a waiting time of 250 fs, an interval equal to five times the pulse duration.[22] A 50 μm pathlength CaF_2 cell was used for measurements with $\tau_2 > 2$ ps.

To correct for ±10 fs zero timing uncertainty and the mixing of real and imaginary components this causes, the spectral phase was adjusted to give a purely absorptive line shape. Before their addition, rephasing and nonrephasing spectra were multiplied by separate phase factors, ϕ, to account for errors in defining $\tau_1=0$ and $\tau_3=0$:

$$\phi_R = \exp(i\omega_1 \Delta\tau_{1,R} + i\omega_3 \Delta\tau_3)$$

$$\phi_{NR} = \exp(i\omega_1 \Delta\tau_{1,NR} + i\omega_3 \Delta\tau_3).$$

Here $\Delta\tau$ is the time-zero positioning error. It has been shown previously that the projection slice theorem equates the projection of the real part of the absorptive 2D IR spectrum onto the $\omega_1 = 0$ axis with the dispersed pump-probe for the same τ_2 value.[9,23] Dispersed pump-probe spectra were collected for each value of τ_2 using the *b* and *c* beams of the interferometer. The above phasing parameters were adjusted to minimize the difference between the projection of the 2D surface and the dispersed pump-probe.

3.4 Collection schemes for 2D IR spectra

3.4.1 Time/Frequency scanning for the acquisition of 2D IR spectra

Previous multidimensional spectroscopy studies have demonstrated the utility of spectrally dispersing the ω_3 axis and detecting all wavelengths at the same time using an array detector. Collecting the whole ω_3 axis at the same time eliminates the possibility of any phase shift occurring in this dimension. While τ_3 no longer needs to be scanned in this collection scheme, one still needs to scan τ_1 and so accurate control of time delays are necessary in order to obtain high quality Fourier transforms. The translation stages used in this study employ linear encoders which are specified to have an accuracy of at least ±150 nm with a reproducibility of 50 nm. While accurate compared to other mechanical stages, the specified accuracy error of $\sim\lambda/10$ at 3 μm can result in distortions of the 2D IR line shape on the ~10% level. To obtain high quality transforms, we exploited the high reproducibility of these stages to correct for systematic error in their linear encoders. Interferograms between alignment HeNe beams ($\lambda = 632.8$ nm) were collected across the entire travel of each translation stage. Fourier transformation of the HeNe interferogram, as shown in Figure 3.8, resulted in significant ghost peaks as the encoder error is $\sim\lambda/3$ at 632 nm. A Fourier transform procedure was used to extract the temporal phase. The procedure is shown pictorially in Figure 3.9. The Fourier transform of the time domain HeNe interferogram was high pass filtered to remove the contribution of components below zero frequency. Filtering makes the frequency domain spectrum asymmetric about the zero frequency point so that inverse Fourier transformation of the filtered HeNe spectrum yields a complex time domain interferogram, $S_{HeNe}(t) = S'_{HeNe} + iS''_{HeNe}$. Taking the arctangent of the ratio of imaginary to real parts of this quantity yields the time domain phase, $\phi = \arctan(S''_{HeNe} / S'_{HeNe})$. If the stage motion were perfect, one would anticipate that the slope of the phase would increase linearly at a rate equal to the HeNe frequency multiplied by the change in the stage's relative position, $\phi = \omega_{HeNe}\Delta\tau$. The residual of a linear fit to the extracted phase is the position-dependent encoder error $\delta\phi = \phi - \omega_{HeNe}\Delta\tau$ and was used to construct a look-up table. A plot of the residual is shown in the inset to Figure 3.8, indicating that the encoder error is very periodic on a 30 μm length of travel (i.e. 200 fs in time delay) and approximately 2 rad (i.e. 0.66 fs) in magnitude. The error table is constructed relative to the absolute encoder position and was used to correct the stage motion at each step of the travel by modifying the step size sent to the translation stage by the error. For example, if the desired step size is 2 fs and the encoder table indicated that $\delta\phi = 0.1$ fs at this absolute encoder position than the stage was instructed to move 1.9 fs. The resulting transform of a HeNe interferogram with the corrected motion is nearly a single point with no periodic error (see bottom panel of Figure 3.8). The compact design of the interferometer and high stability of the jet provided less than a π phase drift between signal and LO over a two hour period. Our approach demonstrates that one can passively achieve the interferometric accuracy and stability necessary to measure high quality 2D line shapes in the mid-IR without introducing feedback loops or additional material dispersion onto the excitation beams.

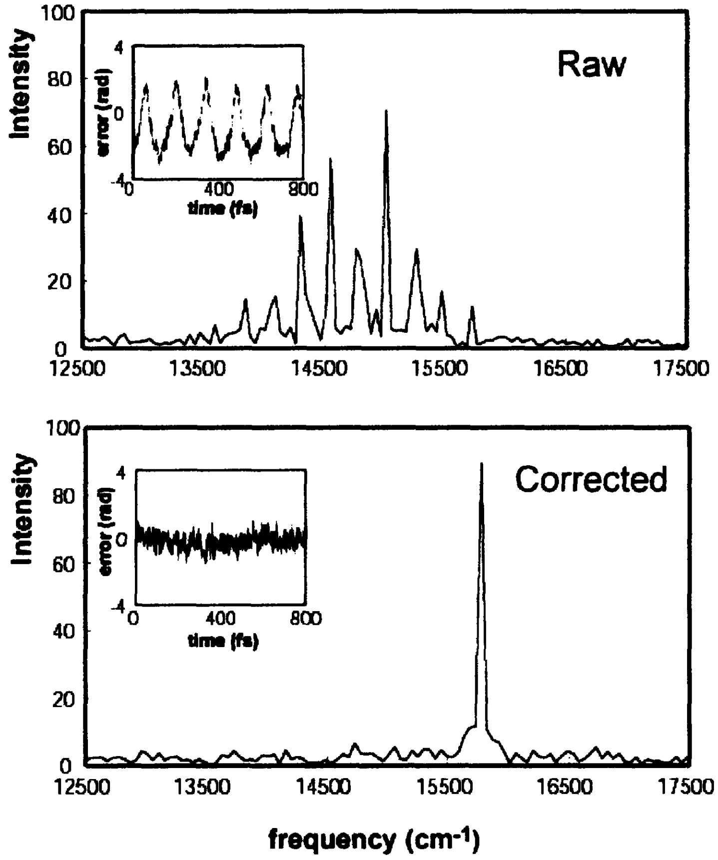

Figure 3.8. Use of HeNe interferometry to characterize translation stage motion before (top) and after (bottom) calibration. The main panels depict the Fourier transform of the HeNe interference while the inset shows the encoder error.

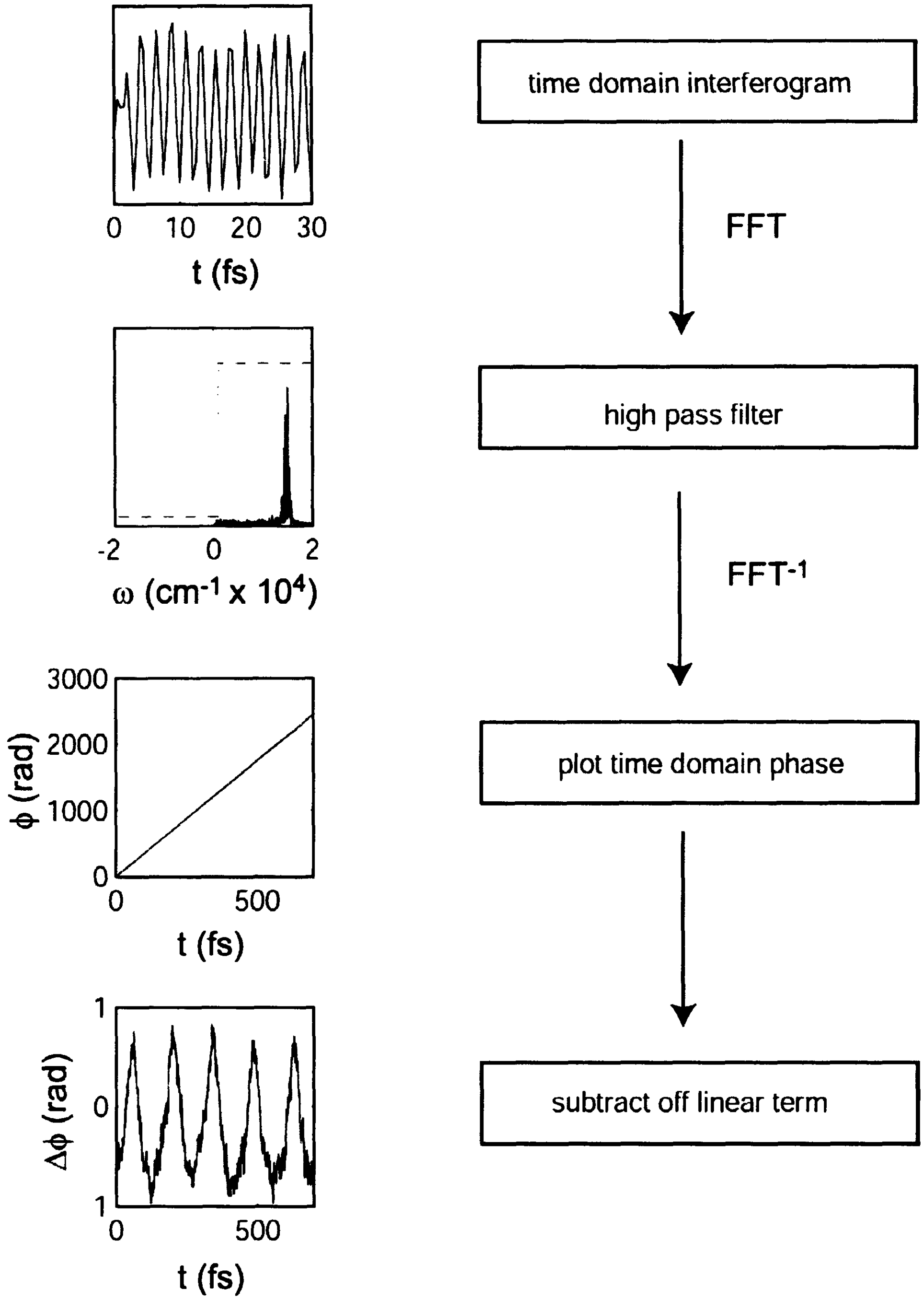

Figure 3.9. Procedure for extracting translation stage error from HeNe interferometry.

Amplitude and phase information of the signal field was determined through spectral interferometry between the emitted signal and LO fields. The approach is a dual channel differential detection method between two phase shifted signals.[24,25] The two fields were combined on a 50/50 beam splitter, giving two matched beams of the combined signal and LO. The beams were aligned parallel but vertically displaced and were focused onto the entrance slit of a 0.19 m Jobin Yvon spectrometer with a 75 groove/mm grating. The two frequency dispersed beams were imaged onto the two stripes of a 64×2 element liquid-nitrogen-cooled MCT (HgCdTe) array detector with high speed signal acquistion (IR Systems Development) that sampled the array at the 1 kHz pulse repetition rate. Each pixel measures 1 mm tall by 0.1 mm wide with a 50 μm gap between pixels and a frequency resolution of ~5 cm^{-1} per pixel. The two stripes are vertically displaced by 5 mm. The phase shift upon reflection off of the beam splitter ensures that the two signal-LO interferograms are π phase shifted, as shown in Figure 3.10. Improper alignment into the spectrometer, however, can reduce this phase shift. To insure that the frequency dispersion onto the two detection channels was in registry, a ~600 fs delay between signal and LO was introduced and the beam alignments were adjusted so that the two signals were π phase shifted. Subtracting the two channels removes any homodyne signals and reduces intensity fluctuations of the LO. A mechanical chopper modulated the *c* excitation beam at 500 Hz allowing for differential detection of the signal-LO interferogram. Variations of the signal level between the stripes at a given frequency were corrected in software by normalizing to the signal level of the LO beam. Such balanced detection resulted in roughly a factor of four improvement in signal-to-noise compared to single stripe detection, and allowed for the collection of a 2D spectrum spanning 200 τ_1 points and 300 cm^{-1} of bandwidth in 20 minutes.

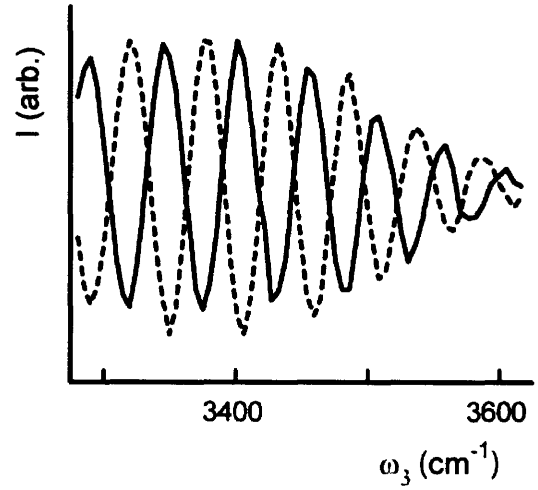

Figure 3.10. Demonstration of balanced spectral detection of the signal/local oscillator signals. Solid and dashed lines are used to distinguish the two interferograms imaged on the two stripe MCT array detector and demonstrate the π phase shift between the two signals.

Two-dimensional data were collected by measuring the interference between signal and LO as a function of ω_3 and τ_1 for a set value of τ_2. The leftmost panel in Figure 3.11 displays the data as it is collected. The detection frequency, ω_3, was calibrated by interferometry between the LO beam and a third-order nonresonant signal from a CaF_2 window at the sample position. Interferograms collected by the array as a function of τ_1 were Fourier transformed to determine the frequency at each pixel.

In order to measure the full absorptive line shape of the combined fundamental and overtone transitions, the grating of the spectrometer was stepped and data was acquired for two overlapping detection frequency ranges. Rephasing and nonrephasing spectra were collected separately and scanned for 200 fs in the τ_1 dimension in steps of 2 fs. Prior to Fourier transform each spectrum was zero padded to 2048 fs. The raw data was then transformed, phased separately and subsequently averaged together in the overlapping region, which was ~20 cm^{-1}. In most cases the phasing parameters were found to be nearly identical with slight timing differences of ~1 fs. To remove the contribution of the finite bandwidth of the excitation pulse from ω_3, the data was normalized to the pulse spectrum in the detection dimension. A 15 cm^{-1} FWHM Gaussian smoothing filter was applied to the transformed and phased data in the ω_3 dimension to reduce pixel noise from the multichannel infrared array detector. The rightmost panel in Figure 3.11 displays the real part of the correlation spectrum for the τ_2=0, OH stretch of HOD in D_2O subsequent to patching.

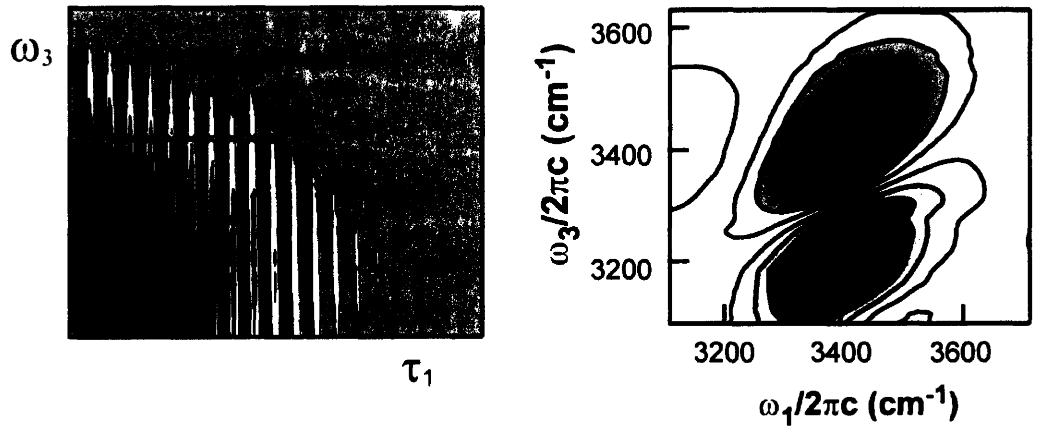

Figure 3.11. (Color) Experimental spectra measured in the mixed time/frequency collection scheme. The leftmost panel shows rephasing data collected on the array detector when the grating of the monochromator was centered on the 0→1 transition (~3650 to 3300 cm^{-1}) of the OH stretch of HOD in D_2O and scanned from τ_1=0 to 200 fs. The line of null intensity is due to a nonfunctioning pixel. The rightmost panel shows the real part of the correlation spectra (τ_2=0) after Fourier transformation of the time/frequency data and subsequent patching of the fundamental and 1→2 parts of the spectrum

3.4.2 Fast time/time scanning for the acquisition of 2D IR spectra

Collecting data by scanning the τ_1 and τ_3 time delays is potentially faster than time/frequency collection when the line shapes are broad in frequency and therefore the signal decays rapidly in the time domain. Here we demonstrate rapid scanning of the τ_3 delay by collecting data as the mechanical translation stage moves at constant velocity. A HeNe tracer is used to track the stage position that is directly related to the τ_3 time axis. This approach is analogous to the operation of most commercial FT-IR instruments but here is applied to the collection of a 2D IR spectrum.

The experimental setup is shown in Figure 3.7. The interferometer and the generation of the signal field is identical to what was described earlier. The signal detection involves two major differences: (1) instead of frequency dispersing the signal/LO, the balanced signals are integrated on two separate single element InSb detectors and (2) we have added a HeNe interferometer to measure the τ_3 timing. A 50/50 beam splitter is used to attenuate the LO and to pick off part of the beam for HeNe interferometry with beam c. We circularly polarize the HeNe tracer overlapped with the picked off LO using a $\lambda/4$ wave-plate. The HeNe beams following beam c and the LO are overlapped on a 50/50 beam splitter while a subsequent polarizing beam cube is used to separate the perpendicular polarization components. The x and y components of the electric field are each detected on separate single element silicon detectors (Thorlabs, det210). Circularly polarizing the LO beam results in a 90 degree phase shift between the x and y components of the electric field, resulting in the two measured signals to be in quadrature (see Figure 3.12). A $\lambda/2$ wave-plate in the beam c arm was used to compensate for any polarization dependent reflectivity of the beam splitter allowing for the balancing of the two signal intensities.

A major advantage of quadrature detection is that the accumulated phase is measured directly:

$$\phi(\tau_{acq}) = \arctan\left(\frac{S_1(\tau_{acq})}{S_2(\tau_{acq})}\right)$$

where ϕ is the phase and S_1 and S_2 refer to two detected HeNe signals and are measured as a function of τ_{acq}, the triggered data acquisition time. The middle panel of Figure 3.12 shows the unwrapped phase when the mechanical stage was commanded to move 1 ps at a constant velocity of 0.058 mm/sec. The accumulated phase is directly related to the relative change in the translation stage's position:

$$\Delta x = x - x_o = \phi * \frac{\lambda_{HeNe}}{\pi}$$

Where x_o is the initial stage position and the HeNe wavelength, λ_{HeNe}, is 632.8 nm. Position can then be readily converted to the stage timing: $\Delta t = \frac{\Delta x}{2c}$. The derivative of the unwrapped phase is the velocity of the translation stage, $\mathrm{v}(\tau_{acq}) = \frac{\partial \phi}{\partial \tau_{acq}}$, shown in the bottom panel of Figure 3.12. One is clearly able to resolve the acceleration and deceleration of the translation stage as it begins moving and slows down as it nears its end position. Excluding the regions of acceleration and deceleration, the stage velocity is not constant. The velocity has a clear periodicity on a similar length scale to the position error measured in the previous section. Both arise from encoder error.

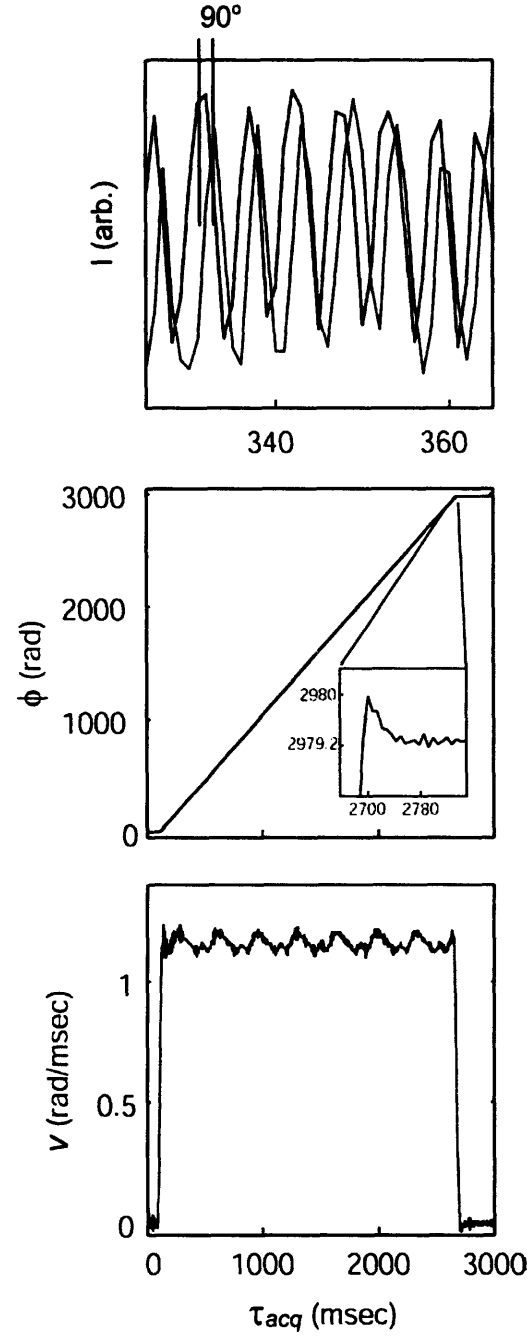

Figure 3.12. (Color) Velocity and position tracking of a translation stage moving at constant velocity using HeNe interferometry. The top panel depicts S_1 and S_2, the in quadrature HeNe interferogram signals. The middle panel shows the extracted phase while the inset reveals that the stage slightly overshoots its position before backtracking and stopping. The bottom panel depicts the stage velocity as a function of the data acquisition time.

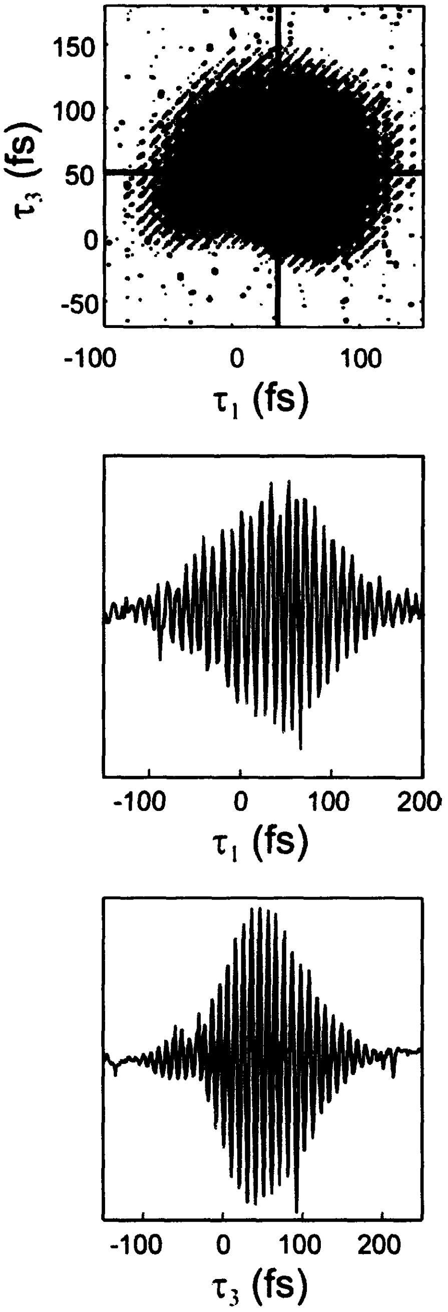

Figure 3.13. (Color) Time/time surface for OH stretch of HOD in D_2O with τ_2=0 fs (top panel). Solid lines indicate where the τ_1 and τ_3 slices, shown in the second and third panels, were taken.

In order to collect a 2D spectrum both the τ_1 and τ_3 axes need to be collected. For a given τ_1, we rapidly scan the τ_3 axis and then step τ_1 on the order of ~λ/5 (i.e. 2 fs at μm). The balanced IR signals and the HeNe signals can be measured simultaneously using a low end, 250 kilo-samples per second DAQ card (National Instruments). Acquisition is triggered off the kHz repetition rate of our Ti:sapphire amplifier. The scanning velocity of the τ_3 axis is limited by our need to sufficiently sample the HeNe fringe (i.e. ~6 samples per fringe) and the laser repetition rate. At 1 kHz this corresponds to a velocity of $\mathrm{v}(\tau_{acq}) = 0.35\text{fs/msec}$, resulting in ~30 samples of the IR fringe at a wavelength of 3 microns. We find that the stage motion and data acquisition is highly reproducible. Therefore we can forgo correcting the τ_3 axis in real time and instead apply an averaged τ_3 time axis to every τ_1 time point. Collection of a 2D spectrum took roughly 6 minutes, a factor 5 faster than if the spectrum were collected by stepping both the τ_1 and τ_3 dimensions. This significant improvement in speed results from eliminating the acceleration, deceleration and equilibration time of the translation stage associated with each time step.

The measured 2D surface in the τ_3 dimension is interpolated and binned to 10 evenly spaced points per fringe (i.e. 1 fs intervals at 3 microns). Figure 3.13 displays a time/time 2D surface of the OH stretch of HOD in D_2O. Slices through the τ_1 and τ_3 dimensions, shown in the second and third panels of Figure 3.13 show the high signal to noise possible using this method. The balanced detection, accomplished by taking the difference of the 180 degree phase shifted signals on the single shot level, resulted in ~10 fold increase in the signal to noise compared to single channel detection.

It is often desirable to average 2D surfaces together to increase the signal to noise. Increasing the data acquisition time of a single 2D surface is not desirable as it is more likely to result in phase instabilities during data collection. Direct averaging of time domain surfaces is also not particularly viable, as any phase shifts in the data will result in the averaging out of the signal field. To circumvent these problems, we average the time domain envelopes of the collected surfaces before reapplying the carrier and subsequently processing the data in a similar fashion as the time/frequency data.[26] Rephasing and nonrephasing spectra were transformed separately. Prior to Fourier transformation both time axes were zero padded to 2048 fs and the τ_3 axis was wrapped around the $\tau_3=0$ point. The envelope extraction procedure is depicted in Figure 3.14. First, the collected time domain surface is half-wave rectified and Fourier transformed. This results in the aliasing of the envelope to zero frequency. The spectral data is low pass filtered to isolate the zero frequency component and inverse transformed back to the time domain. The extracted envelopes of multiple surfaces can be averaged together. Carrier oscillations can be reapplied in each dimension at the mean frequency of oscillation, which is determined through Fourier transformation of the raw data. The real part of the Fourier transform of an averaged time domain envelope is shown in Figure 3.15.

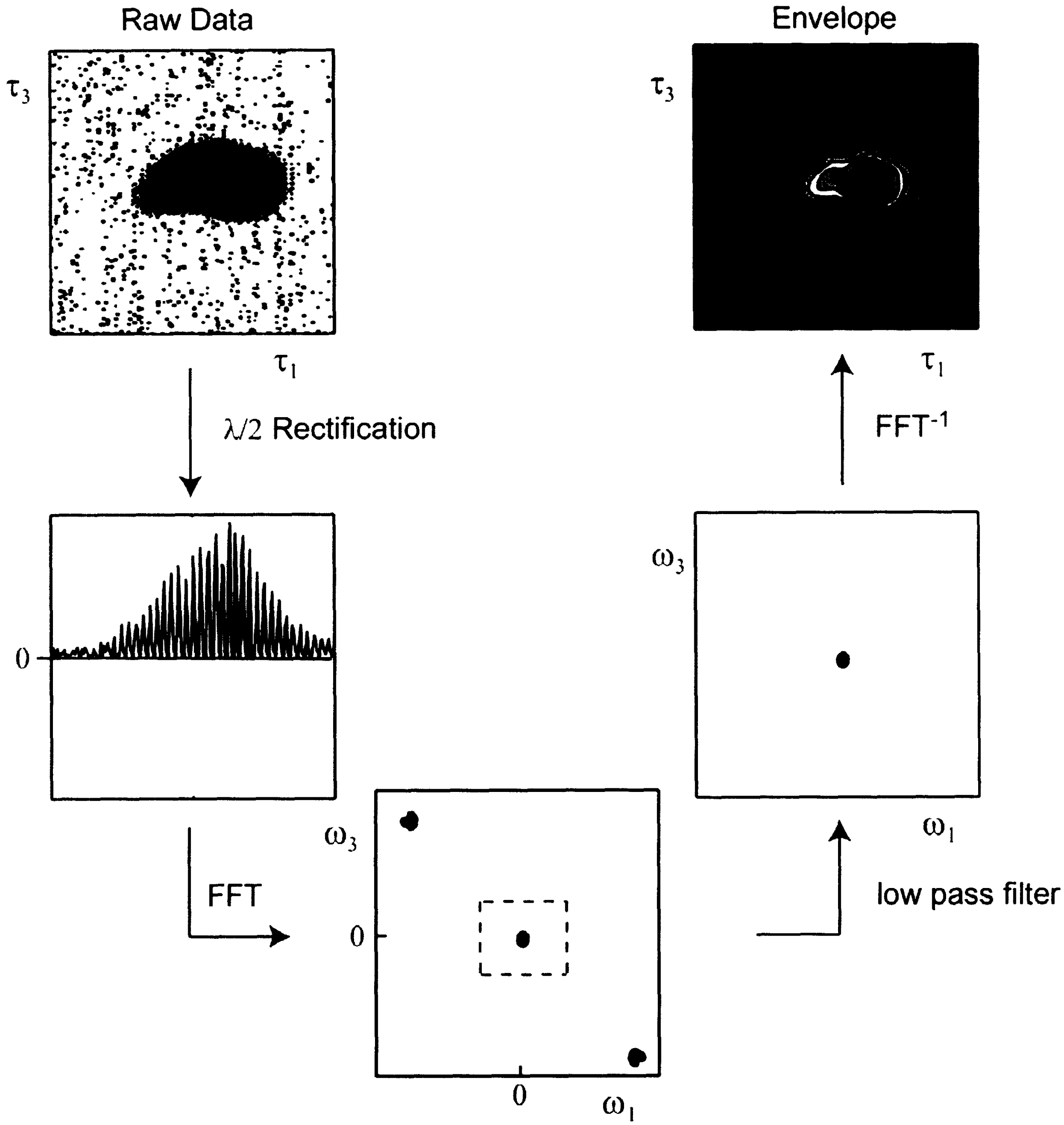

Figure 3.14. Envelope extraction procedure for the averaging of time domain surfaces acquired through fast scanning.

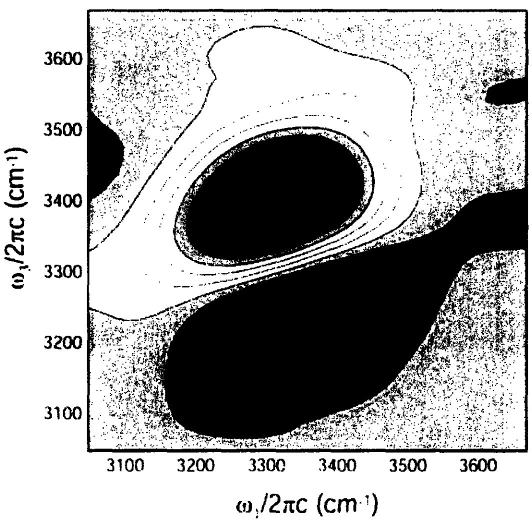

Figure 3.15. Real part of the τ_2 = 200 fs correlation spectrum collected using the fast scanning time/time collection scheme.

3.5 Conclusions

We have demonstrated two methods to acquire high fidelity 2D IR line shapes. In the first, we presented a mixed time/frequency collection scheme with calibrated translation stage motion and balanced spectral interferometry using a 2 by 64 channel MCT array detector. In the second approach, the τ_1 by τ_3 time domain surface is measured by rapidly scanning the τ_3 delay while collecting the integrated signal on two single channel detectors. Both approaches rely on a HeNe reference to accurately control time delays between the excitation pulses, resulting in accurate frequencies upon Fourier transformation. In the time/frequency approach this is accomplished passively, in that the translation stages only have to be calibrated once while in the time/time scheme the velocity of the stage motion has to be measured for each surface collected.

Mixed time/frequency approaches are the most powerful when used with array detection as done in this current work. However, IR arrays are significantly behind their silicon counterparts. Typical linear IR arrays that can acquire at the required 1 kHz repetition rates cost on the order of $50,000 with the 2x64 model used here costing $80,000. The second stripe is important because it allows for balanced spectral interferometry, which greatly enhances the signal to noise for weakly absorbing species like the OH dipoles studied here. Comparatively, balanced detection in the time/time collection scheme requires only two single channel detectors, greatly reducing the cost compared to array detection. Recently, techniques have been developed to eliminate the need for IR arrays by upconverting the IR signal in a nonlinear crystal and then using established silicon array technology.[27] This greatly increases the pixel density and reduces the cost, yet it is still more expensive than two single channel IR detectors.

The greatest argument for the time/frequency approach is the multiplexing advantage that comes with collecting the ω_3 axis in a single shot. This advantage is emphasized for narrow spectral features that would require further scanning of the τ_3 time delay in the time/time collection scheme. For broad line shapes, like those investigated here, acquisition rates for time/time scanning are faster than the time/frequency approach. Integrating the signal on a single detector element greatly improves the signal to noise as the light detected by a single pixel in the array detection is greatly reduced due to the breadth of the OH line shape. Increasing the laser repetition rate, which allows for even faster scanning in the time/time approach, will make this collection scheme desirable for even molecular systems with narrower lines, such as those found in proteins and peptides.

References

[1] T. Steinel, J. B. Asbury, S. A. Corcelli, C. P. Lawrence, J. L. Skinner, and M. D. Fayer, Chem. Phys. Lett. **386**, 295 (2004).

[2] J. D. Eaves, J. J. Loparo, C. J. Fecko, S. T. Roberts, A. Tokmakoff, and P. L. Geissler, Proceedings of the National Academy of Sciences of the United States of America **102**, 13019 (2005).

[3] A. W. Smith, H. S. Chung, Z. Ganim, and A. Tokmakoff, Journal of Physical Chemistry B **109** (36), 17025 (2005).

[4] A. T. Krummel and M. T. Zanni, J. Phys. Chem. B **110**, 13991 (2006).

[5] L. Lepetit, G. Cheriaux, and M. Joffre, J. Opt. Soc. Am. B **12**, 2467 (1995).

[6] S. M. Gallagher, A. W. Albrecht, J. D. Hybl, B. L. Landin, B. Rajaram, and D. M. Jonas, J. Opt. Soc. Am. B **15**, 2338 (1998).

[7] P. Hamm, M. Lim, and R. M. Hochstrasser, J. Phys. Chem. B **102** (31), 6123 (1998).

[8] V. Cervetto, J. Helbing, J. Bredenbeck, and P. Hamm, J. Chem. Phys. **121**, 5935 (2004).

[9] J. D. Hybl, A. A. Ferro, and D. M. Jonas, J. Chem. Phys. **115**, 6606 (2001).

[10] M. Khalil, N. Demirdoven, and A. Tokmakoff, Journal of Physical Chemistry A **107** (27), 5258 (2003).

[11] M. L. Cowan, J. P. Ogilvie, and R. J. D. Miller, Chem. Phys. Lett. **386**, 184 (2004).

[12] T. Brixner, I. V. Stoipkin, and G. R. Fleming, Opt. Lett. **29**, 884 (2004).

[13] V. Volkov, R. Schanz, and P. Hamm, Optics Letters **30**, 2010 (2005).

[14] T. Zhang, C. N. Borca, X. Li, and S. T. Cundiff, Optics Express **13**, 7432 (2005).

[15] N. F. Scherer, R. J. Carlson, A. Matro, M. Du, A. J. Ruggiero, V. Romero-Rochin, J. A. Cina, G. R. Fleming, and S. A. Rice, J. Chem. Phys. **95**, 1487 (1991).

[16] W. P. de Boeij, M. S. Pshenichnikov, and D. A. Wiersma, Chem. Phys. Lett. **238**, 1 (1995).

[17] T. Joo, Y. Jia, J.-Y. Yu, M. J. Lang, and G. R. Fleming, J. Chem. Phys. **104**, 6089 (1996).

[18] W. P. de Boeij, M. S. Pshenichnikov, and D. A. Wiersma, Annu. Rev. Phys. Chem. **49**, 99 (1998).

[19] C. J. Fecko, J. J. Loparo, and A. Tokmakoff, Opt. Commun. **241**, 521 (2004).

[20] J. A. Gruetzmacher and N. F. Scherer, Rev. Sci. Inst. **73** (6), 2227 (2002).

[21] N. Demirdöven, M. Khalil, O. Golonzka, and A. Tokmakoff, Optics Letters **27** (6), 433 (2002).

[22] C. J. Fecko, J. J. Loparo, S. T. Roberts, and A. Tokmakoff, J. Chem. Phys. **122**, 054506 (2005).

[23] M. Khalil, N. Demirdöven, and A. Tokmakoff, Phys. Rev. Lett. **90**, 47401 (2003).

[24] G. L. Abbas, V. W. S. Chan, and T. K. Yee, J. Lightwave Technology **LT-3**, 1110 (1985).

[25] E. C. Fulmer, F. Ding, and M. T. Zanni, J. Chem. Phys. **122**, 034302 (2005).

[26] A. Ambardar, *Analog and digital signal processing*. (Brooks/Cole Publishing, 1999).

[27] M. F. DeCamp and A. Tokmakoff, Optics Letters **30**, 1818 (2005).

Chapter 4

Reorientational and configurational fluctuations in water

4.1 Introduction

The unique physical and chemical properties of water originate from the hydrogen bond rearrangements that make transient intermolecular geometries appear, fluctuate, and disappear. Since the early 1970's, researchers have used molecular dynamics (MD) simulations to explore the connection between hydrogen bonding interactions and the bulk and transport properties of water. The pioneering work of Rahman and Stillinger explained much of the available experimental data for liquid water with classical mechanics on simple empirical potentials.[1] Inspired by the success of these models, researchers have applied them to elucidate the microscopic mechanisms of hydrogen bond breaking and forming. These studies have found that intermolecular dynamics span time scales from roughly 50 femtoseconds for motions on molecular length scales, to picoseconds for cooperative molecular reorganization of the liquid. It is only recently, with the ability to generate optical and infrared pulses that are faster than the intermolecular motions of water, that femtosecond spectroscopies have been able to experimentally probe the dynamics of water molecules and hydrogen bonds. Here, we present a unified analysis of infrared vibrational echo and polarization-selective pump-probe experiments that reveal the short time molecular reorientation and hydrogen bond dynamics in water prior to collective reorganization. This provides new experimental data for comparison to predictions from molecular dynamics simulation based on empirical classical potentials.

Infrared spectroscopy is an ideal technique to study hydrogen bonding liquids because the frequency of the OH stretch is sensitive to the hydrogen bonded environment. Spectroscopists have commonly used an isotopically dilute sample of HOD in D_2O as a model system because the OH vibration is a localized probe, free of vibrational coupling between neighboring OH oscillators that complicates the spectroscopy of pure water. Recent molecular dynamics studies have shown that there is a fairly strong correlation between the OH frequency of HOD in D_2O and the O-H···O hydrogen bond length.[2-4] However, the angular variation of hydrogen bonds in the liquid reduces this correlation. More generally, we have shown that the molecular electric field at the proton in the direction of the OH bond vector determines the frequency ω.[4] The configuration of the hydrogen bond acceptor molecule with respect to the OH bond determines the majority of the field strength. Structural evolution of the hydrogen bonding network changes the electric field felt by the OH oscillator and results in time-dependent shifts in the OH stretching frequency $\delta\omega(t)$. Transient infrared spectroscopy is capable of measuring these OH frequency shifts, or spectral diffusion. The characteristic timescales and amplitudes of spectral diffusion can then be related to hydrogen bond configurational changes and reorganization of the hydrogen bonding network.

In most studies to date, spectrally narrow pulses have excited a part of the OH absorption line shape of HOD in D_2O and the relaxation of this sub-ensemble was probed as it re-equilibrated.[5-7] These transient hole burning (THB) experiments have characterized sub-picosecond time scales, but the narrow spectral bandwidth required in these measurements has limited the time resolution to roughly 150 fs. This prevented them from observing water's fastest intermolecular motions. Vibrational echo experiments have accessed the sub-100 fs time scales of spectral diffusion in water, although with varying results.[4] [8-12]Our vibrational echo peak shift (PS) measurement with 50 fs pulses, shown in Figure 4.1a, has a rapid 60 fs decay and a weak beat peaking at 160 fs, before dropping into a 1.2 ps decay.[4] Here we report a series of polarization-dependent pump-probe (PP) experiments with even shorter pulses, which show new signatures of librational motions predicted by MD simulations and further support the observation of underdamped hydrogen bond motion. A self-consistent modeling of the PP and the PS data yields three dynamical quantities that provide a quantitative description of spectral diffusion, vibrational population relaxation, and molecular reorientation: $C(\tau)$, T_1, and $p_2(\tau)$. The OH frequency autocorrelation function is $C(\tau)=\langle\delta\omega(\tau)\delta\omega(0)\rangle$, $1/T_1$ is the rate for relaxation of the OH vibration, and $p_2(\tau)=P_2\langle\hat{\mu}(\tau)\cdot\hat{\mu}(0)\rangle$ is the second Legendre polynomial of the reorientational correlation function for the unit vector of the OH transition dipole. Because the short temporal duration of the excitation pulse provided enough frequency bandwidth to span the fundamental and most of the anharmonically shifted overtone of the OH stretch of HOD/D_2O, these pulses averaged over all molecular environments. The measurements allow for direct comparison of the

IR spectroscopy of HOD/ D_2O to models and simulations of vibrational dephasing, lifetime and reorientation based on correlation functions.

4.2 Acquisition of polarization-selective pump-probes

Experiments used 45 fs pulses generated with a dual stage BBO/$KNbO_3$ optical parametric amplifier pumped by a 30 fs Ti:sapphire amplifier. The pulses typically had a spectral bandwidth of 400 cm^{-1} with flat spectral phase (<0.2 rad variation) when characterized by SHG-FROG. The center frequency was set to 3300 cm^{-1} to span the entire fundamental absorption lineshape and much of the anharmonically shifted $v = 1 \rightarrow 2$ transition. The sample was an HOD in D_2O water jet formed by a 50 μm sapphire nozzle with a total peak optical density of ~0.4. We have found that experiments taken in sample cells show a strong nonresonant response from the cell window that masks the short time dynamics observed in the jet. The polarization of the beams was controlled with wire-grid polarizers. Data was acquired by measuring the pump-induced transmission change on the probe pulse, normalized to the transmission of a third reference pulse. To reduce $v = 2$ induced absorption signals in PP experiments, the transmitted probe beam passed through a 50 cm^{-1} bandpass filter centered at line center (3400 cm^{-1}) before detection.

4.3 Results and discussion

Polarization-selective pump-probe measurements can be used to separate the dynamics of reorientation from dephasing and lifetime relaxation. When combined with PS experiments, polarization-dependent PP experiments can isolate each contribution.

Figure 4.1b shows PP measurements for parallel $S_{\parallel}$, perpendicular $S_{\perp}$, and magic angle S_{MA} polarization geometries. The polarization measurements differ in both the profile of the sub-500 fs transients and the time scales of their long time decays. S_{MA} is free of reorientational effects and shows an asymptotic single exponential decay due to the OH lifetime with T_1 = 700 fs. This value can be compared with values of 650[6], 740[13], and 1000 fs[7] from THB. On time-scales long compared to T_1, PP measurements reveal a 3% percent offset (inset Figure 4.1b). This offset is similar to long time signals observed in IR THB and narrow-band PS experiments, which are ascribed to vibrational-relaxation-induced changes in the excitation of intermolecular motions leading to a "hot-ground state" differential absorption signal.[9,13] This offset remains constant for more than 50 ps, which is consistent with heating and re-equilibration of the sample via thermal diffusion.

The reorientational correlation function of the OH dipole $p_2(\tau)$ is obtained from the parallel and perpendicular pump-probe measurements though the anisotropy $r(\tau)=\left(S_{\parallel}-S_{\perp}\right)/\left(S_{\parallel}+2S_{\perp}\right)$, shown in Figure 4.1c. The anisotropy has an initial value of 0.38, and decays biexponentially with 50 fs and 3 ps components. The 50 fs component has not been observed previously in IR measurements, but follows the time scale associated with molecular libration. The long time component is similar to experimental time scales observed by IR hole-burning and NMR.[14-16]

The influence of vibrational dephasing on the PP transient is apparent by subtracting the effects of reorientation and population relaxation, as shown in the inset to Figure 4.1d. This short time transient should follow the correlation function for the system[17], and shows a rapid decay followed by a weak recurrence at ~180 fs. This transient is similar to the short time behavior of the PS measurement, and provides further evidence for underdamped modulation of the OH frequency during dephasing.

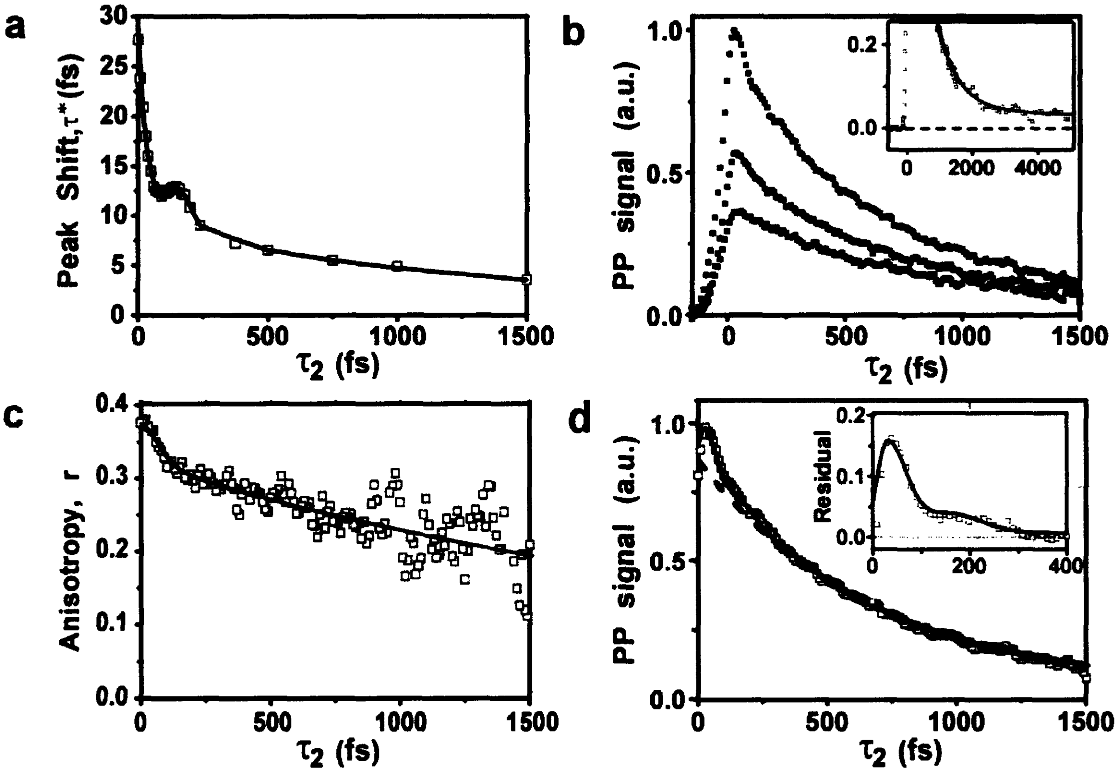

Figure 4.1. Data is represented as points while fits from a unified analysis of the data are solid lines. (a) The vibrational echo peak shift. (b) Polarization-selective pump-probe. $S_{\parallel}$, S_{MA} and $S_{\perp}$ are shown from top to bottom. Inset shows the offset present in the long time tail of the pump-probe signal. (c) Anisotropy $r(\tau)$ determined from $S_{\parallel}$ and $S_{\perp}$. (d) $S_{\parallel}$ with exponential fit to the long time tail. The inset shows the residual when the exponential fit is subtracted from the data.

The PP and PS data can be described self-consistently with a third-order nonlinear response function $\bar{\mathbf{R}}^{(3)}$ that is expressed in terms of frequency correlation functions for the splitting between vibrational levels, the vibrational lifetime for v = 1, and orientational correlation functions for the OH vector. The formalism is similar to methods we have described previously[18], and draws on the multilevel nonlinear response function described by Sung and Silbey.[19] We account for vibrational relaxation phenomenologically by adding vibrational lifetimes for the different levels, while reorientation is expressed in terms of $p_1(\tau)$ and $p_2(\tau)$. Correlation functions for the energy gaps, the transition moments, and the vibrational lifetime involving the v = 2 state are related to expressions involving v = 1 through harmonic scaling relationships to reduce the number of free parameters. For the orientational correlation function we assume that the OH transition moments for μ_{10} are parallel to μ_{21}, and use the scaling factor for diffusive orientation $p_1(\tau)=p_2(\tau/3)$. In order to account for the observed offset in the experimental data at times longer than the vibrational lifetime, we use a response function that accounts for spectroscopic changes on relaxing to a hot ground state. This approach is similar to schemes used to model previous experiments.[9,13] Good fits to both the long time PS and the offset observed in the PP required a 12 cm^{-1} relaxation-induced blue shift in the fundamental transition energy and a 5% decrease in the transition moment. This is consistent with the spectral changes observed in FTIR spectra of HOD in D_2O when the temperature increases. The experiments are simulated by convoluting $\bar{\mathbf{R}}^{(3)}$ with the electric field of the pulses, taking into account all possible time-ordered signal contributions into the wavevector matched direction. The solid lines plotted along with the data in Figure 4.1 are the best fits obtained with this formalism. The fit reproduces the short, intermediate and long time features of the PS and PP data.

The underlying dynamics of vibrational dephasing, lifetime, and reorientation, expressed as $C(\tau)$, T_1, and $p_2(\tau)$ are shown in Figure 4.2a. From these quantities one can construct a picture of the underlying dynamics of water's hydrogen bonding network. The correlation time for frequency fluctuations of $\tau_C = 340$ fs, calculated by integrating $C(\tau)$ and dividing by $C(0)$, serves as a convenient way to divide the dynamics. Times shorter than τ_C reflect the dynamics of structural fluctuations within relatively fixed intermolecular configurations, whereas longer time scales characterize the kinetics of collective configurational changes in the hydrogen bond network.

At short times the dynamics are dominated by two fast time scales: the 50 fs decay component of the reorientational correlation function and the underdamped oscillation with the 180 fs time period in the frequency correlation function. Both timescales are due to fast intermolecular motions that occur over molecular length scales. These reflect hindered rotations and translations, intermolecular fluctuations that, according to MD simulations, lead to hydrogen bond breaking.[20] The oscillatory behavior in $C(\tau)$ largely reflects the intermolecular motion between the HOD and the hydrogen bonding partner for the proton. While the OH frequency shift reflects the electric field of all D_2O molecules acting on the OH coordinate, the displacement and angular changes between the two molecules results in the dominant fluctuations of the molecular electric field projected onto the OH coordinate.[4] The oscillation shows that the hydrogen bond is not overdamped as previous IR THB studies had concluded.[5,6] The fast decay in $p_2(\tau)$ is consistent with the librational motion of water. Unlike Raman measurements that probe the many-body polarizability, the infrared measurement presented here is an observation of the hindered rotational motion of individual OH dipoles. The cosine transform of the frequency correlation function (not shown) has a very small contribution at 400 cm^{-1} suggesting that librations do not contribute significantly to the rapid decay of the $C(\tau)$.

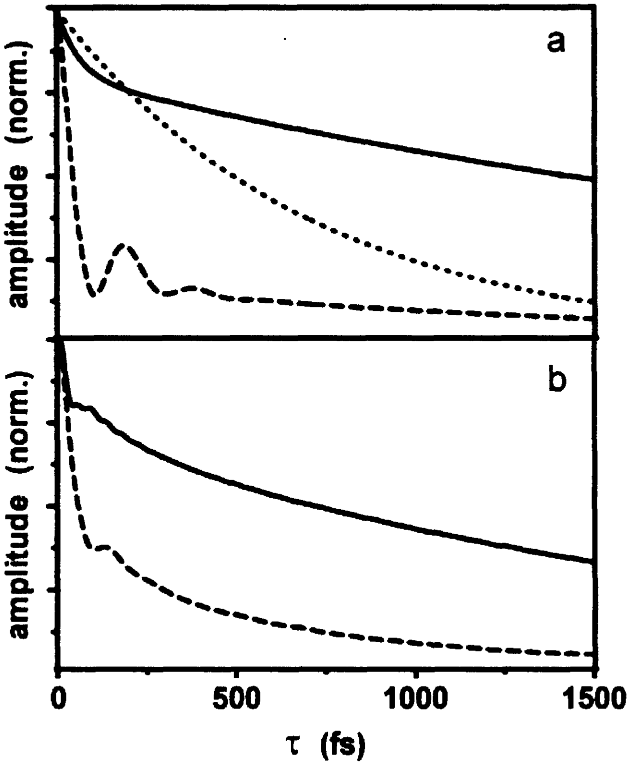

Figure 4.2. (a) Plots of the normalized $C(\tau)$ (dashed), $p_2(\tau)$ (solid), and OH vibrational lifetime decay ($exp(-\tau/T_1)$; dotted). The zero-time amplitude of the correlation function was found to be $C(\tau) = 5.7 \times 10^{-4}$ fs^{-2}. (b) $C(\tau)$ and $p_2(\tau)$ derived from MD simulation of HOD in D_2O using the SPC/E model for water.[4] The long time decays of $C(\tau)$ and $p_2(\tau)$ are 0.6 ps and 2.6 ps respectively.

At times longer than τ_C, the frequency correlation function and the anisotropy decay on 1.4 and 3 ps time scales respectively. As shown previously by simulations, a variety of relaxation mechanisms occur on the picosecond time scale including the collective rearrangement of the hydrogen bonding network, as well as density and polarization fluctuations on length scales greater than a molecular diameter. Contrary to the dynamics at early times that are well described by the OH oscillator and its hydrogen bonding partner, these processes involve the motions of many molecules and are therefore inherently collective. Molecular reorientation is also collective, occurring with the structural reorganization of the hydrogen bonding network as a molecule must break multiple hydrogen bonds to rotate. On a similar timescale of 700 fs, the combination of these intermolecular forces act on the OH coordinate leading to fast vibrational relaxation.

The frequency and reorientational correlation functions presented here demonstrate remarkable agreement with over thirty years of MD simulations. In $C(\tau)$ we observe an oscillation corresponding to the intermolecular vibration in the oxygen velocity autocorrelation function for water[2,21], first calculated by Rahman and Stillinger. Likewise, Stillinger's calculation of $p_2(\tau)$ showed biexponential relaxation with comparable time scales to those measured by our experiment.[1] Only recently have MD simulations attempted to calculate the frequency correlation function for the OH stretch.[2-4] Figure 2b shows simulation results for $C(\tau)$ and $p_2(\tau)$ of HOD in D_2O derived from the SPC/E model for water. Calculations like these by Lawrence and Skinner give similar results regarding the fast and slow time scales.[3] The qualitative agreement between simulation and experiment indicates that relatively simple fixed point charge water potentials capture the essential reorientational and dephasing dynamics measured in the present experiments. The fact that the experimental timescales are consistently longer than that obtained from this model argue that more sophisticated models for the intermolecular interactions in water could lead to better quantitative agreement. For instance, including polarizable effects, where molecular charges respond dynamically to the environment, show slower reorientational diffusion and hydrogen bond breaking times.[22,23]

The vibrational and orientational motions reported here represent an average over all possible initial intermolecular configurations, each of which may in fact experience different dynamical environments on subtly different time scales. While there is evidence that sub-ensemble dynamics are spectrally heterogeneous[11,24], we have made approximations in our analysis that do not describe a heterogeneous system. Specifically, our model assumes the fluctuations are Gaussian, and does not properly treat systems where molecules prepared on the red or blue side of the OH lineshape relax differently. Nonetheless, our observation of a fast correlation time τ_c and simple exponential relaxation on longer time scales suggest a small degree of heterogeneity in reorientation and lifetime on picosecond time scales. This is consistent with the finding of two-dimensional infrared spectroscopy described in Chapter 6. Our analysis provides an averaged description of hydrogen bonding dynamics within the traditional pictures of spectroscopy, and gives a self-consistent description of the many time-dependent relaxation phenomena of HOD in D_2O.

References

[1] A. Rahman and F. H. Stillinger, J. Chem. Phys. 55, 3336 (1971).

[2] R. Rey, K. B. Moller, and J. T. Hynes, J. Phys. Chem. A 106 (50), 11993 (2002).

[3] C. P. Lawrence and J. L. Skinner, J. Chem. Phys. 118, 264 (2003).

[4] C. J. Fecko, J. D. Eaves, J. J. Loparo, A. Tokmakoff, and P. L. Geissler, Science 301, 1698 (2003).

[5] S. Woutersen and H. J. Bakker, Phys. Rev. Lett. 83, 2077 (1999).

[6] G. M. Gale, G. Gallot, F. Hache, N. Lascoux, S. Bratos, and J.-C. Leicknam, Phys. Rev. Lett., 1068 (1999).

[7] R. Laenen, K. Simeonidis, and A. Laubereau, J. Phys. Chem. B 106 (408-417) (2002).

[8] J. Stenger, D. Madsen, P. Hamm, E. T. J. Nibbering, and T. Elsaesser, Phys. Rev. Lett. 87, 027401 (2001).

[9] J. Stenger, D. Madsen, P. Hamm, E. T. J. Nibbering, and T. Elsaesser, J. Phys. Chem. A 106 (10), 2341 (2002).

[10] S. Yeremenko, M. S. Pshenichnikov, and D. A. Wiersma, Chem. Phys. Lett. 369, 107 (2003).

[11] T. Steinel, J. B. Asbury, S. A. Corcelli, C. P. Lawrence, J. L. Skinner, and M. D. Fayer, Chem. Phys. Lett. 386, 295 (2004).

[12] J. B. Asbury, T. Steinel, C. Stromberg, S. A. Corcelli, C. P. Lawrence, J. L. Skinner, and M. D. Fayer, J. Phys. Chem. A 108, 1107 (2004).

[13] H. K. Nienhuys, S. Woutersen, R. A. v. Santen, and H. J. Bakker, J. Chem. Phys. 111, 1494 (1999).

[14] G. Gallot, S. Bratos, S. Pommeret, N. Lascoux, J.-C. Leicknam, M. Kozinski, W. Amir, and G. M. Gale, J. Chem. Phys. 117, 11301 (2002).

[15] D. W. G. Smith and J. G. Powles, Mol. Phys. 10, 451 (1966).

[16] H.-K. Nienhuys, R. A. van Santen, and H. J. Bakker, J. Chem. Phys. 112 (19), 8487 (2000).

[17] D. A. Farrow, A. Yu, and D. M. Jonas, J. Chem. Phys. 118, 9348 (2003).

[18] M. Khalil, N. Demirdoven, and A. Tokmakoff, J. Phys. Chem. A 107 (27), 5258 (2003).

[19] J. Sung and R. J. Silbey, J. Chem. Phys. 118 (5), 2443 (2003).

[20] A. Luzar and D. Chandler, Phys. Rev. Lett. 76, 928 (1996).

[21] U. Balucani, J. P. Brodholt, and R. Vallauri, J. Phys. : Condens. Matter 8, 6139 (1996).

[22] H. Xu, H. A. Stern, and B. J. Berne, J. Phys. Chem. B 106, 2054 (2002).

[23] E. Harder, J. D. Eaves, A. Tokmakoff, and B. J. Berne, Proc. Nat. Acad. Sci. 102, 11611 (2005).

[24] J. D. Eaves, J. J. Loparo, C. J. Fecko, S. T. Roberts, A. Tokmakoff, and P. L. Geissler, Proc. Natl. Acad. Sci. USA 102, 13019 (2005).

Chapter 5

Multidimensional infrared spectroscopy of water. Vibrational dynamics in 2D IR line shapes

5.1 Introduction

The ability to form hydrogen bonds profoundly impacts water's physical properties. The hydrogen bonding interaction, in conjugation with water's small molecular size and weight, leads to an extended network of interconnected molecules. Many of water's unique properties can be explained by static or average quantities that describe the structure or energetics of this network. Aqueous reactivity, however, is largely determined by hydrogen bond dynamics, the fluctuations and rearrangements of hydrogen bonds, which lead to the ultrafast stabilization of nascent charge[1] and the rapid shuttling of protons through solution.[2] Viewed from the perspective of motion on a corrugated free energy landscape,[3,4] hydrogen bond dynamics include distortions about stable structures, defined by minima on the free energy landscape, and the thermally activated switching between these states. Unlike time-averaged or instantaneous structural variables, it remains difficult to obtain definitive experimental evidence for the mechanism of dynamic processes, such as the switching of hydrogen bonding partners.

In this and the following chapter, I describe the use of two-dimensional infrared (2D IR) spectroscopy to study the fluctuations, structural reorganization kinetics, and the reaction dynamics of hydrogen bond switching. Ultrafast infrared spectroscopy is a powerful tool to investigate the rearrangements of water's hydrogen bonding network because the OH stretching frequency, ω_{OH}, is sensitive to the local hydrogen bonding environment. Commonly studied in a dilute solution of HOD in D_2O to avoid the intermolecular energy transfer that accompanies near-degenerate oscillators in the neat liquid, ω_{OH} is sensitive to hydrogen bonding interactions and dielectric fluctuations felt by the proton.[5-7] Generally speaking, stronger hydrogen bonding interactions act to red shift (or lower) ω_{OH}. From the gas to liquid, ω_{OH} red shifts 300 cm^{-1} and the line shape broadens significantly (~260 cm^{-1} FWHM). Recent studies have established that ω_{OH} is correlated with the total electric field projected onto the proton along the OH bond vector.[7-11] The nearest neighbor to the proton of HOD is the largest contributor to the total electric field felt by the proton, explaining the dependence of ω_{OH} on the hydrogen bonding distance, R_{oo},[12] and the weak correlation with hydrogen bonding angle, α.[5,6]

If correlations between OH frequency and hydrogen bonding structure are established, then time-resolved studies of ω_{OH} can be used to report on hydrogen bonding dynamics and kinetics. Such observations motivated IR transient holeburning and mixed IR/Raman measurements which have provided important insight into the timescales of vibrational relaxation and reorientation of the OH stretch of HOD in D_2O and suggested frequency dependent spectral relaxation dynamics.[13-18] However, the required trade off between frequency and time resolution (>150 fs) in these experiments has left open questions, since they are unable to resolve the fastest timescales of water's hydrogen bonding network. Recent broadband echo experiments have allowed for greater time resolution resulting in the observation of both a fast (~100 fs) and a slow (~1 ps) timescale to spectral diffusion.[19-22] Analysis of broadband vibrational echo measurements to extract dynamical information using a nonlinear response function typically relies on a Gaussian approximation for the statistics of the time-dependent fluctuations of the vibrational energy gap $\delta\omega(\tau) = \omega(\tau) - \langle \omega \rangle$.[23-25] Then, the spectral evolution within the experiments can be uniquely described through a two-point frequency correlation function

$$C(\tau) = \langle \delta\omega(\tau)\delta\omega(0) \rangle . \tag{1}$$

Using 50 fs pulses, we previously observed the intermolecular dynamics of hydrogen bond stretching on a period of 180 fs in the $C(\tau)$ extracted from vibrational echo peak shift measurements.[7,26] The drawback in analyzing the data in terms of two-point correlation functions is that one cannot distinguish spectrally varying dynamics underneath the broad OH line shape.

As a full characterization of the third-order material polarization, 2D IR spectroscopy provides the frequency resolution missing in broadband echo experiments while avoiding the trade-off between time and frequency resolution inherent in transient hole burning techniques. An absorptive 2D IR spectrum is in essence a correlation map between the vibrational frequency of oscillators resonantly excited at an initial frequency (ω_1) and the distribution of final frequencies detected (ω_3) after a waiting time τ_2. The frequency, intensity, and time dependence of the 2D IR line shape in the ω_1 and ω_3 dimensions serve as spectral observables that shed light on how different hydrogen bonded configurations evolve and interchange.[22,27-29] Changes in the 2D IR line shape as a function of τ_2 result from the spectral diffusion of OH oscillators. As a Fourier transform technique and given that the excitation pulse is broader than the vibrational transition of interest, the experimental timescale is not set by the pulse duration. Instead, it is dictated by the molecular response of the system and is approximately equal to the dephasing induced decay of the signal field.

In this pair of chapters, I present an analysis of the waiting time dependence of 2D IR line shapes of the OH stretch of HOD in D_2O. Here I concentrate on the frequency-averaged characterization of the signal arising from these dynamics and kinetics, quantified through $C(\tau)$. I show how changes in the 2D IR line shape and intensity as a function of waiting time result from a number of molecular relaxation processes including spectral diffusion, molecular reorientation, vibrational relaxation and the subsequent thermalization of this excess energy by the bath. From a previous analysis of broadband vibrational echo and pump-probe experiments, we have concluded that a separation of time scales exists between femtosecond configurational fluctuations of hydrogen bonded molecules and picosecond kinetics of collective hydrogen bonding reorganization.[7,21,26] Prior to a waiting time of ~1 ps, changes in the 2D IR line shape predominately reflect spectral diffusion. Similar to homodyne echo experiments, the spectral evolution of ω_{OH} is encoded in Fourier transform 2D IR experiments as the relative amplitudes of the rephasing and non-rephasing components of the 2D spectrum. I discuss the analysis of several metrics of these amplitudes and relate them to $C(\tau)$. 2D spectra at long waiting times ($\tau_2 \geq 2$ ps) are dominated by the effects of vibrational relaxation and the subsequent thermalization of vibrational energy. These processes are adequately described by a single phenomenological vibrational relaxation time constant and a spectroscopically distinct hot ground state absorption.

Modeling based on $C(\tau)$ is able to predict the gross changes observed in the experiment but fails to describe the asymmetry of the experimental line shapes. In the following chapter I analyze the frequency-dependent spectral relaxation present in the 2D IR line shapes. The spectral relaxation of specific hydrogen bonded configurations, particularly those excited near the hydrogen bond switching transition state, provide a way of testing long standing questions about the free energy landscape of water.

5.2 2D IR results for HOD in D_2O

A waiting time series of experimentally measured 2D IR spectra of HOD in D_2O is shown in Figure 5.1. Two representations of the data are plotted, the real part of the correlation spectrum, S'_C and the phase spectrum S_φ. Correlation spectra are the sums of their respective complex rephasing (S_R) and nonrephasing (S_{NR}) spectra, with S'_C or S''_C measuring changes in absorption or refractive index in ω_3 induced by excitation at ω_1, respectively. The various representations of the complex 2D IR data for τ_2 = 100 fs is presented in Figure 5.2.

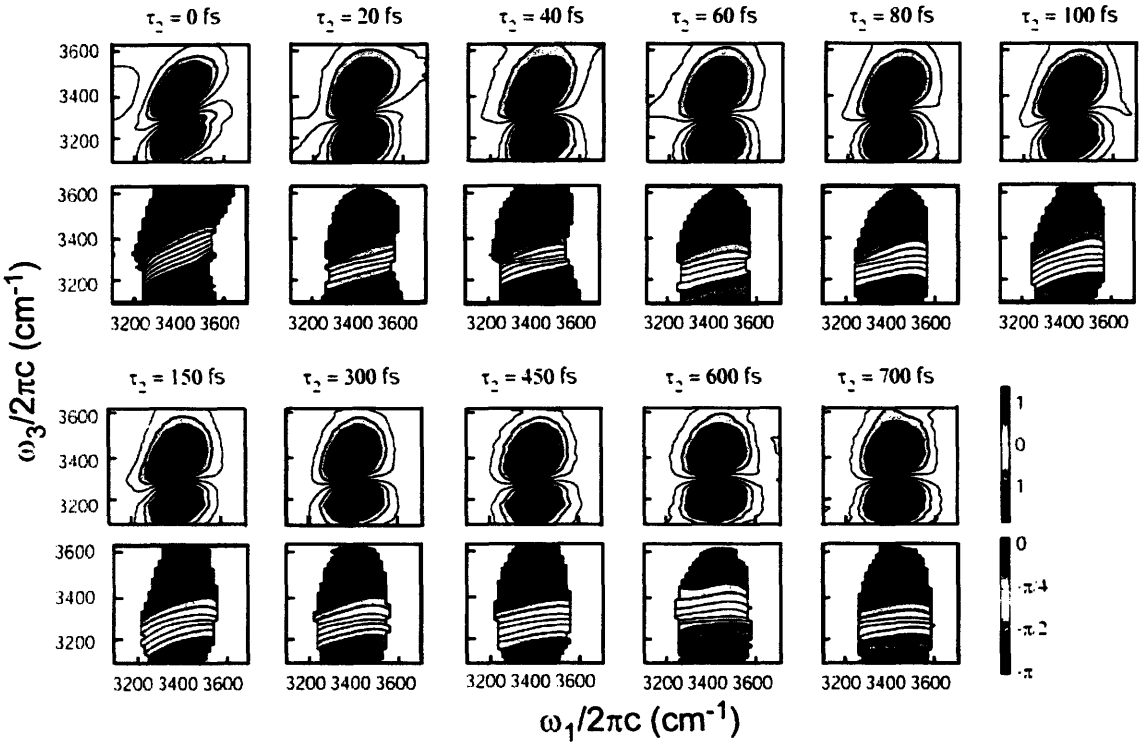

Figure 5.1. (Color) Measured 2D IR absorptive (S'_C) and phase (S_φ) spectra for the OH stretch of HOD in D_2O for waiting times up to the vibrational lifetime. Absorptive spectra were plotted with fifteen evenly spaced contours while contours for the phase span from $-\pi$ to 0 degrees in 12 evenly spaced increments. Positive amplitudes in the absorptive spectra (red) reflect bleaches of the fundamental transition ($-\Delta$OD) whereas negative peaks (blue) reflect v = 1→2 induced absorption.

The absorptive spectrum S_C' shows two peaks, a positive peak due to a transient bleach of the v = 0 → 1 (fundamental) transition and an anharmonically shifted, negative peak due to the v = 1 → 2 induced absorption. The S_C' line shapes undergo changes in both their relative tilt and width as a function of τ_2. The 2D IR spectra at early waiting times are diagonally elongated indicating that memory of the excitation frequency exists during the waiting time. With increasing waiting time this elongation disappears and the slope of the node separating the fundamental and overtone transitions rotates, becoming nearly parallel with the ω_1 axis by $\tau_2 = 700$ fs. The broadening along the antidiagonal axis of the 2D line shapes is a result of spectral relaxation during the waiting time, indicating fluctuations about hydrogen bonded structures and the exchange of hydrogen bonding environments.

Being dependent on the ratio of S_C'' to S_C', lines of constant phase in S_φ reflect how relative amplitudes vary in the correlation spectrum and therefore reveal the overall shape of the spectra. The node in S_C' corresponds to the $\varphi(\omega_1,\omega_3) = -\pi/2$ constant phase line, and the nodes in S_C'' correspond to $\varphi = 0$ and $-\pi$. Phase spectra reveal a $\sim\pi$ phase shift across the 2D line shapes. Although qualitatively different in appearance than S_C', S_φ exhibits similar behavior as a function of τ_2. Lines of constant phase are initially elongated along the diagonal and rotate down with waiting time.

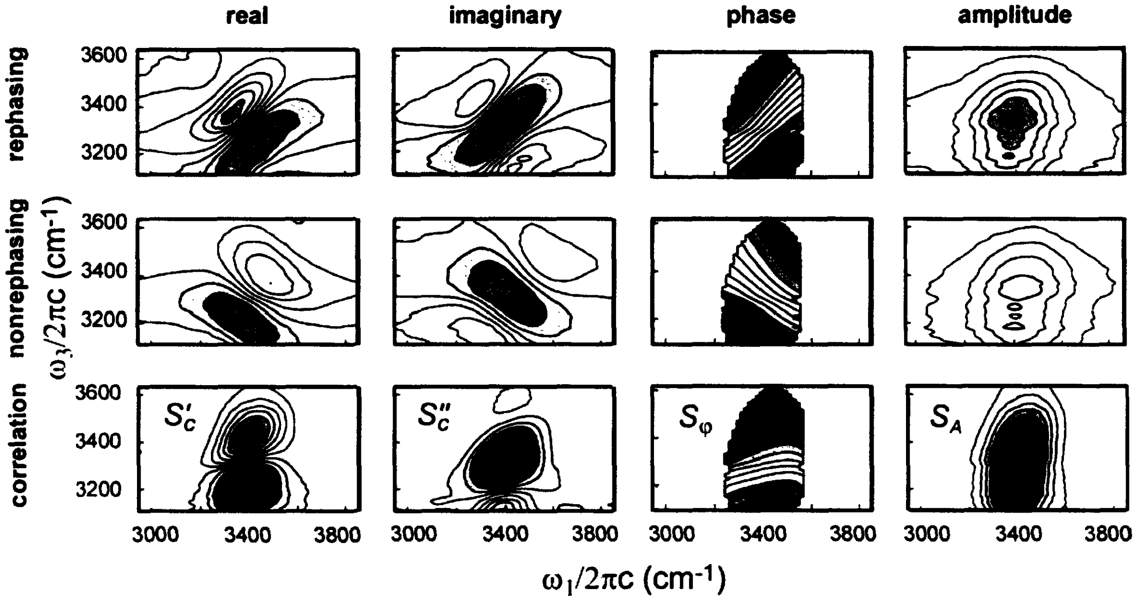

Figure 5.2. (Color) A comparison of real/imaginary and phase/amplitude representations of 2D IR spectra for a waiting time of 100 fs. To illustrate how the intensities between the rephasing and nonrephasing spectra vary, all real, imaginary and absolute value spectra are plotted relative to the maximum intensity of the absolute value correlation spectrum.

For waiting times longer than 700 fs, the thermalization of excess energy deposited through vibrational relaxation becomes the dominant source of observed spectral changes. We have investigated this process with dispersed pump-probe (DPP) (Figure 5.3) and 2D IR experiments (Figure 5.4). Signatures of population relaxation and reorientation are most clearly observed in the DPP spectrum as a function of τ_2 (see Figure 5.3a). The DPP contains two main spectral features: a positive going transient bleach centered initially at 3415 cm^{-1} due to the 0→1 transition and a negative going transient absorption at 3150 cm^{-1} due to the 1→2 transition. For times up to ~1.3 ps the relative scaling between fundamental and overtone intensity remains equal with the amplitude of both transitions decaying with τ_2 at a rate given by 660 fs due to vibrational relaxation and molecular reorientation. As this scaling changes with time delay, the maximum of the fundamental transition begins to shift to lower frequency. A plot of the frequency of the signal maximum as a function of τ_2 is shown in Figure 5.3b. The dotted line is the decay of the excited state population and indicates that the DPP spectral relaxation dynamics are roughly a factor of two slower than the vibrational lifetime. By ~3 ps the overtone transition has disappeared but a positive going signal due to the ground state hole remains (see Figure 5.3a). This signal, the offset observed in earlier pump-probe measurements, is centered at ~3360 cm^{-1}.[21,26,30,31]

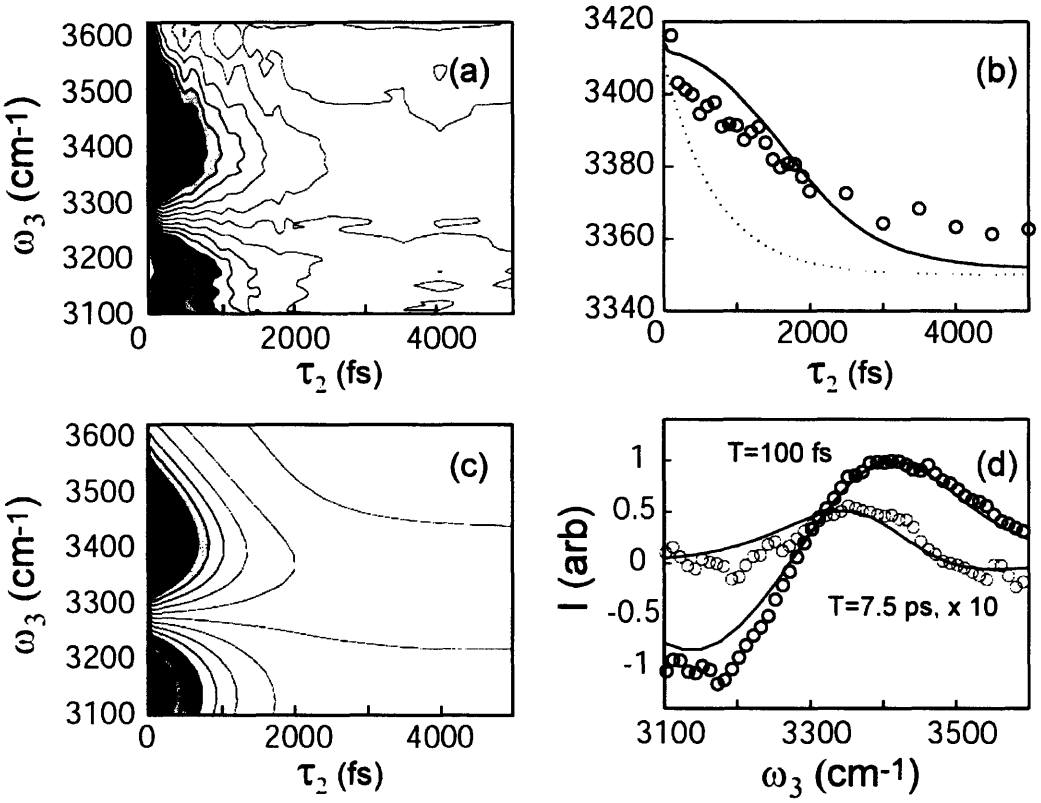

Figure 5.3. (Color) Dispersed pump-probe spectra for HOD in D_2O. Unfilled circles represent the measured data while the solid line shows the result predicted from nonlinear response function calculations. (a) The measured dispersed pump-probe spectra of HOD in D_2O as a function of time delay between the pump and the probe beams. (b) The shift in ω_{10} as a function of the pump-probe delay time. The shift in the maximum of fundamental occurs on a longer timescale than the vibrational lifetime (~700 fs, dashed line). (c) Calculated dispersed pump-probe signal from the nonlinear response function calculation. (d) Slices through the dispersed pump-probe spectrum for waiting times of 100 fs and 7.5 ps.

2D IR spectra for τ_2 = 2.0 and 7.5 ps are shown in Figure 5.4. At 2 ps, the overtone remains, although the intensity has decreased by over a factor of 2 relative to the fundamental intensity. The node between fundamental and overtone is flat indicating a lack of frequency correlation. 2D IR spectra at these long waiting times most clearly resemble the homogeneous limit in which oscillators have had the opportunity to sample the breadth of the frequency distribution before they are detected in τ_3. By 7.5 ps the 2D IR spectrum appears qualitatively different. The overtone has disappeared due to population relaxation out of the excited state and the absorptive spectrum is a single positive going peak centered at roughly 3400 cm^{-1} in ω_1 and ~3360 cm^{-1} in ω_3.

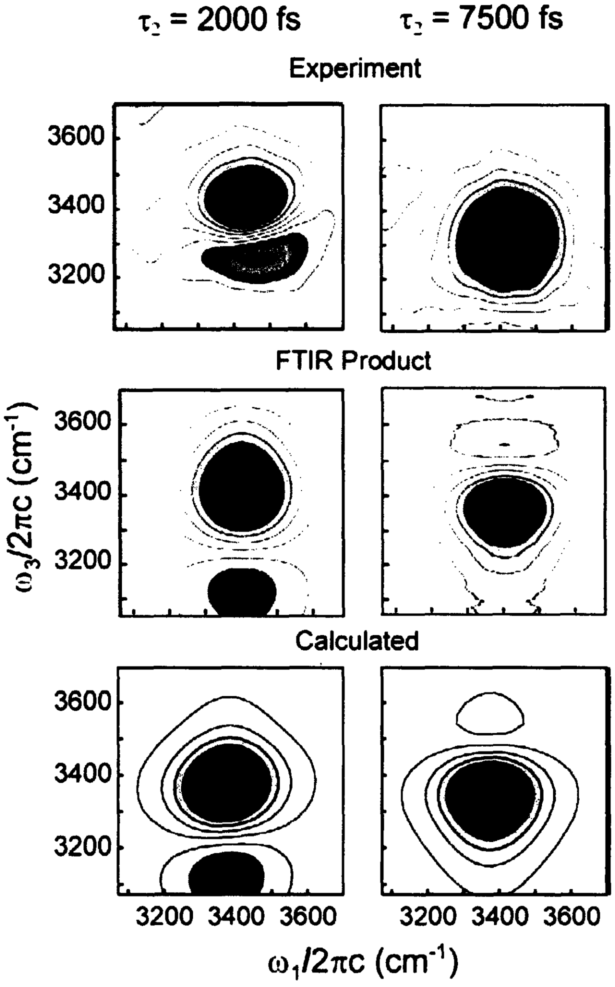

Figure 5.4. (Color) 2D IR spectra for waiting times beyond the vibrational lifetime. The top panels depict the experimentally measured 2D IR spectra of HOD in D_2O for waiting times of 2.0 and 7.5 ps. The middle panels show the two-dimensional product spectra constructed from the FTIR OH line shape of HOD. The bottom panels show the calculated 2D IR spectra from the nonlinear response function formalism using the parameters described in the text.

5.3 Discussion

5.3.1 Interpretation of 2D IR line shapes

Information on changing hydrogen bonding configurations is encoded in 2D IR spectroscopy in terms of time-dependent changes to the OH vibrational frequency. As a starting point to understanding the waiting evolution of 2D IR line shapes, Figure 5.2 compares various representations of the complex 2D IR correlation spectrum for HOD in D_2O taken at τ_2 = 100 fs.[32] Rephasing and nonrephasing spectra are elongated along the diagonal ($\omega_1=\omega_3$) and anti-diagonal ($\omega_1+\omega_3$=constant) axes, respectively. The spectral phase representation shows that this is due to the difference in the sign of the phase accumulated between τ_1 and τ_3. In the rephasing processes, coherences oscillate in conjugate frequencies during τ_1 and τ_3, leading to an echo signal at $\tau_1 = \tau_3$ when frequency memory persists through the waiting time. Conversely, nonrephasing pathways oscillate in phase during the two periods and closely resemble a free induction decay in both dimensions. It is this difference in phase that results in the canceling of the dispersive wings of S_{NR} and S_R in S_C. As evident in Figure 5.2, the intensities of the S_R outweigh S_{NR} because $C(\tau)$ has not decayed fully by 100 fs. Thus S'_C is preferentially elongated along the diagonal, with a tilt of the nodal line. While the absolute value correlation spectrum S_A remains largely structureless, the slope of the lines of constant spectral phase in S_φ capture the diagonal elongation of the real and imaginary correlation spectra.[28] Assuming sufficient spectral bandwidth, the Kramers-Kronig relationship relates the real and imaginary parts of the 2D spectrum, allowing one to construct the phase and absolute value parts of the 2D spectrum from the real part.[33,34]

Formally, the 2D IR spectrum is directly related to a three-time correlation function for the OH dipole operator.[35] Taking only dephasing into account, the response functions for rephasing (–) and nonrephasing (+) processes can be written as[24,35]

$$R_{\pm}(\tau_1,\tau_2,\tau_3)=\sum_{a,b,c,d}\left\langle \exp[\pm i\int_0^{\tau_1} dt'\omega_{ab}(t')+i\int_{\tau_1+\tau_2}^{\tau_1+\tau_2+\tau_3} dt'\omega_{cd}(t')]\right\rangle. \qquad (3)$$

Here $\omega_{ab}=(E_a-E_b)/\hbar$, and *a*, *b*, *c*, and *d* are summed over the 0, 1, and 2 vibrational levels of the OH stretch, leading to terms that differ by the interaction-sequence of the three level system with the pulses. These expressions characterize the frequency memory of a time-varying trajectory between τ_1 and τ_3, and differ only in the phase relationship between the time intervals.

Examining limiting expressions for these response functions gives an indication of the changes one can expect to see in the 2D line shape with waiting time. In the inhomogeneous limit, in which the frequencies are constant during τ_1 and τ_3, the response functions are $R_{inhom}=\sum\left\langle \exp\left[\pm i\omega_{ab}\tau_1-i\omega_{cd}\tau_3\right]\right\rangle$ and the Fourier transformed 2D spectrum is a joint probability distribution

$$S'_{inhom}(\omega_1,\tau_2,\omega_3)=\sum_{a,b,c,d}\left\langle \delta(\omega_1\pm\omega_{ab})\delta(\omega_3-\omega_{cd}(\tau_2))\right\rangle \qquad (4)$$

where the detection frequency depends on any change during τ_2. In the limit $\tau_2 = 0$, there has been no change in frequency during the waiting period, and ensemble averaging will lead to a line shape elongated along the diagonal axis. The other important limit, the homogeneous limit, is the case when vibrational dephasing is rapid compared to τ_2, here the frequencies in τ_1 and τ_3 are uncorrelated and the response function is expressed as the product of free induction decays in τ_1 and τ_3:

$$\lim_{\tau_2 \to \infty} R_{\pm} = \sum_{a,b,c,d} \left\langle \exp[\pm i \int_0^{\tau_1} dt' \omega_{ab}(t')] \right\rangle \left\langle \exp[i \int_0^{\tau_3} dt' \omega_{cd}(t')] \right\rangle . \qquad (5)$$

In this limit, the 2D IR spectrum simplifies to a product of one dimensional line shapes in the ω_1 and ω_3 dimensions. This line shape is symmetric with respect to the diagonal and antidiagonal axes, indicating that the initial excitation at ω_1 is detected at ω_3 with a probability given by the equilibrium probability distribution. On the basis of these limits, we expect that as the waiting time is increased, the 2D IR line shape will evolve from a diagonally elongated form to a symmetric form in a manner dictated by the frequency fluctuations and spectral diffusion of the system.

The transformation of the absorptive correlation spectrum from the inhomogeneous to homogeneous limits is determined by the balance of intensities between the rephasing and nonrephasing spectra. Examples for a fluctuating two-level system are pictured in Figure 5.5. For waiting times shorter than the frequency correlation time ($\tau_2 << \tau_c$), frequency memory is largely preserved and the rephasing signal is emitted as an echo peaked at τ_3 equal to τ_1, as evident in the 2D time domain surface shown in Fig. 5.5a. The nonrephasing signal, plotted for negative τ_1 delays, is symmetric in τ_1 and τ_3. Before the correlation function has decayed significantly, the amplitude of the rephasing signal outweighs the nonrephasing contribution. This imbalance of intensity occurs because inhomogeneity acts to damp the signal field during τ_3 in the nonrephasing response, while its presence is necessary for the rephasing process. Double Fourier transformation of this time domain surface leads to a diagonally elongated absorptive line shape, indicating that the spectral holes burned during τ_1 are largely unchanged when they are probed in τ_3. For $\tau_2 >> \tau_c$, frequency memory is destroyed, the signal maximum occurs near τ_3=0 regardless of the value of τ_1, and the amplitude and shape of the rephasing and nonrephasing signals are nearly equal (see Figure 5.5b). In the frequency domain the 2D line shape is no longer elongated. Instead its symmetric shape indicates that the spectral holes burned in τ_1 have had enough time to sample the whole frequency distribution.

Homodyne echo experiments have commonly exploited the imbalance between rephasing and non-rephasing signals as a means to quantify spectral diffusion. This principle serves as the basis for the echo peak shift (PS) measurement.[7,19,36-39] In Figure 5.5, we also show the projection of the time-domain signal field onto the τ_1 axis, the integrated echo signal. The change in ratio between rephasing and non-rephasing signals is characterized by the shift of the echo peak maximum from positive values of τ_1 to $\tau_1 = 0$ as τ_2 is increased beyond τ_c. Under certain approximations the PS is directly proportional to $C(\tau)$.[24,25]

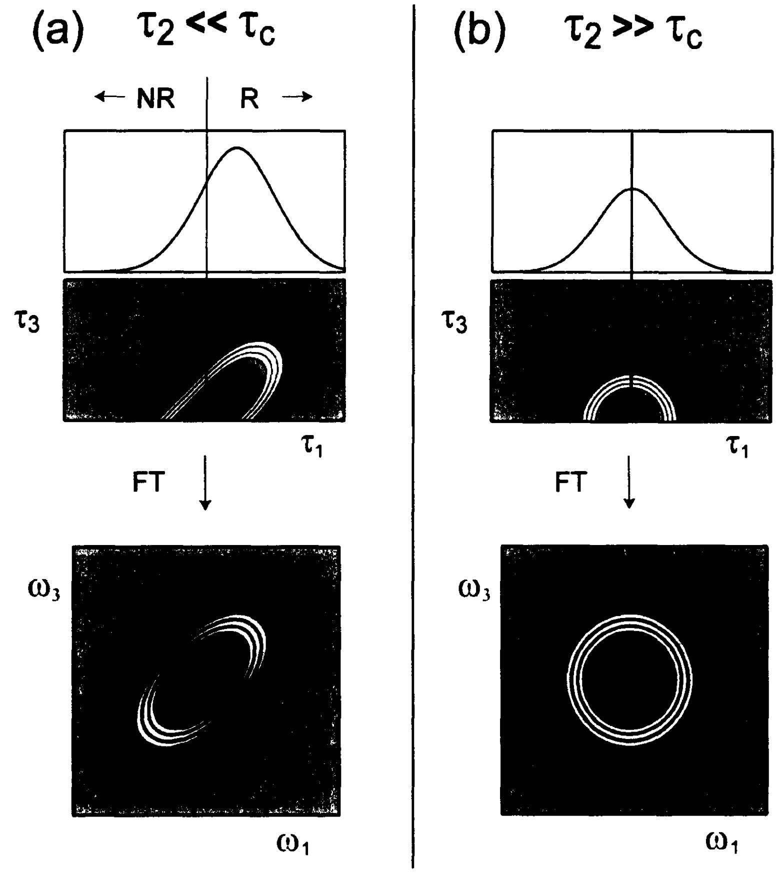

Figure 5.5. (Color) (a) Time domain representation of the 2D surface for a waiting time well before the correlation time. The projection onto the τ_1 axis, shown above the time domain surface, shows the non-zero peak shift. The diagonal elongation of the frequency domain line shape is a consequence of the diagonal elongation of the echo signal in the time domain. (e) Time domain 2D surface for a waiting time well after the correlation time. The rephasing and nonrephasing signals are equivalent resulting in a zero peak shift. The symmetric frequency domain 2D line shape shows that there is no frequency correlation between the evolution and detection time periods, instead the frequency distribution of oscillators is given by the equilibrium frequency distribution.

One can quantify the loss of frequency correlation as a function of waiting time through the 2D spectrum by choosing any number of measures related to the imbalance between the rephasing and nonrephasing intensities. In Figure 5.6, we specifically examine four examples of τ_2-dependent signals that are also proportional to $C(\tau)$ under approximations similar to those used for the analysis of PS measurements, and are not influenced by population relaxation. We have justified the choice of these quantities as selective measures of frequency fluctuations and spectral diffusion in a separate paper.[40]

One measure that is not influenced by population relaxation is the inhomogeneity index

$$I = (A_R - A_{NR})/(A_R + A_{NR}) \qquad (6)$$

where A_R and A_{NR} refer to the integrated signal amplitude under the absolute value rephasing and nonrephasing 2D spectra at a particular τ_2. For a massively inhomogeneous line shape, I approaches one, but as frequency correlation is lost at long waiting times this ratio asymptomatically approaches zero. Figure 5.6 shows $I(\tau_2)$, where the volume was integrated between 3350 and 3450 cm^{-1}, the center of the fundamental transition, in both the ω_1 and ω_3 dimensions.

A consequence of the equalizing of the rephasing and non-rephasing spectra is the broadening of the 2D line shape along the anti-diagonal axis. At $\tau_2 = 0$, the width of an antidiagonal slice through the center of the fundamental 2D line shape is twice as narrow as a slice along the diagonal axis. This ellipticity is characteristic of inhomogeneous line shapes. Recently Pschenichnikov has proposed defining the ellipiticity of the line shape as[41]

$$E = \left(a^2 - b^2\right) / \left(a^2 + b^2\right) \tag{7}$$

where a and b are the characteristic diagonal and antidiagonal full widths at half the maximum intensity of the line shape, respectively. The decrease in this asymmetry with τ_2 can be formally related to $C(\tau)$.[40] We also plot $E(\tau_2)$ in Figure 5.6.

With waiting time, one also observes the slope of the node between 0→1 and 1→2 transitions in S_C gradually aligns with the ω_1 axis.[34,42,43] For a massively inhomogeneous system one would expect a diagonal node with a maximum angle of 45° with respect to the ω_1 axis. At $\tau_2 = 0$, the slope has already rotated to 26° indicating that frequencies already evolve significantly during τ_1 and τ_3 and the line shape is intermediate to the homogeneous and inhomogeneous limits. This "rotation" of the node, the $\varphi = -\pi/2$ line of constant phase, with increasing τ_2 is directly related to the imbalance of rephasing and nonrephasing amplitudes, and therefore contains equivalent information content to $I(\tau_2)$ and $E(\tau_2)$. This can be seen by expressing the lines of constant spectral phase in S_φ (Figure 5.2) in terms of a linear combination of diagonal phase lines in rephasing spectra and anti-diagonal phase lines in nonrephasing spectra. To quantify the slope of phase lines as a function of waiting time, slices through $S_\varphi(\tau_2)$ for ω_3 = 3350 to 3450 cm^{-1} were fit to a line over the range of ω_1 = 3350 to 3450 cm^{-1}. The decay of the slope of the phase lines,

$$\beta(\tau_2, \Omega) = \left.\frac{\partial \varphi(\tau_2)}{\partial \omega_1}\right|_{\omega_1 = \omega_3 = \Omega}, \tag{8}$$

with τ_2 is also related to $C(\tau)$, and is pictured in Fig. 5.6.[40]

Finally, one can also calculate the peak shift from the heterodyned measurement by taking the absolute value squared of the 2D IR surface projected onto the τ_1 axis. To facilitate finding the peak signal delay $\tau^*(\tau_2)$, we filter the carrier oscillations out of the measured time domain response and fit a Gaussian to the resulting time domain envelope. Figure 5.6 contains a plot of the peak shift extracted from our measured 2D IR surfaces.

The four measures described above: I, E, β, and τ^* all show similar behavior as a function of the waiting time and are closely related to one another. Each measure exhibits a fast decay, has an apparent oscillation around ~130 fs and a slower decay component. Qualitatively, the observed dynamics are similar to what we have observed previously in vibrational echo peak shift and pump-probe measurements.[21] As in the homodyne peak shift, however, the spectral observables reported here do not equal $C(t)$ on the timescale less than the correlation time (~340 fs for this system).

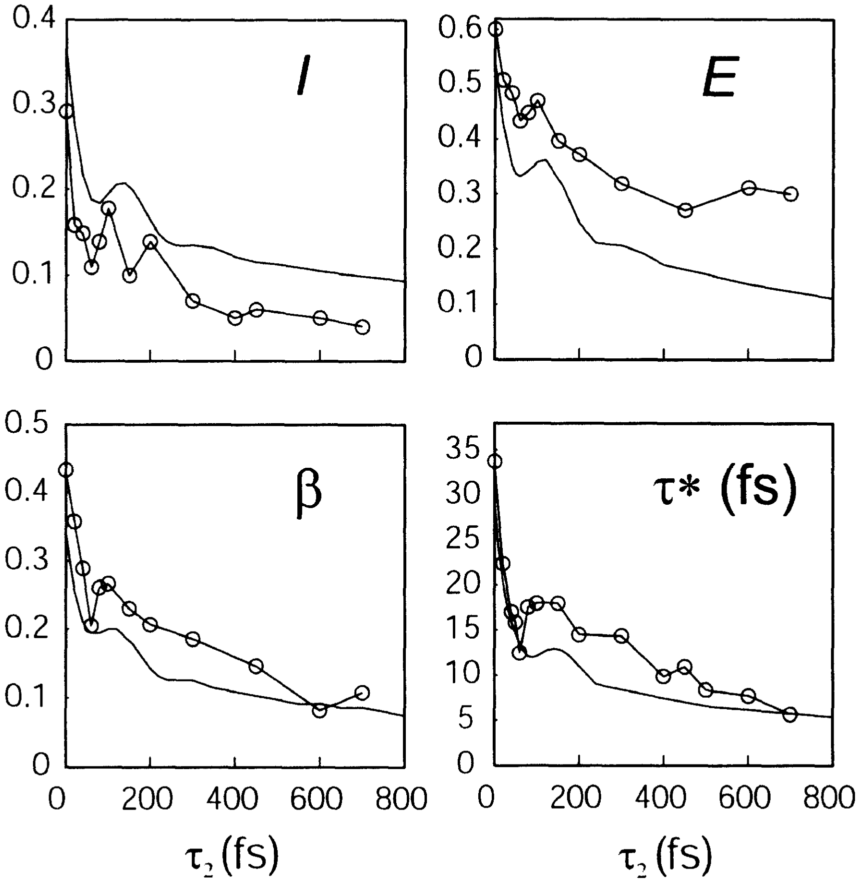

Figure 5.6. Quantifying the loss of frequency correlation in 2D IR spectra through a series of experimental metrics that measure the imbalance in intensity between rephasing and nonrephasing spectra.

5.3.1 Comparison to calculations with Gaussian fluctuations

Calculations with nonlinear response functions provide a direct comparison between the various spectroscopic observables measured here and $C(\tau)$.[35,44] 2D IR observables can be directly calculated from two-point frequency correlation functions, providing one makes two crucial assumptions: (1) The frequency fluctuations of the system are well-represented by Gaussian statistics (second order cumulant approximation), and (2) the transition dipole moment is a constant (Condon approximation). The primary objective of Chapters 6 and 7 is to quantify frequency-dependent vibrational dynamics to test these assumptions. In this chapter we build upon the formalism described in Ref. 21 that uses these assumptions to calculate nonlinear spectroscopic signals for the OH stretch of HOD in D_2O.

For the purpose of comparison, we calculate 2D spectra based on the $C(\tau)$ extracted from a unified analysis of vibrational echo peak shift measurements and polarization pump-probe experiments incorporating spectral diffusion, reorientation and vibrational relaxation as an input.[21] $C(\tau)$ was characterized by a 50 fs decay, a 180 fs beat associated with underdamped hydrogen bond vibrations and an exponential decay of 1.4 ps. Contributions from the $v=1 \rightarrow 2$ transition are modeled using an anharmonicity of 250 cm^{-1} extracted from dispersed pump-probe measurements and harmonic scaling of the frequency correlation functions. Vibrational relaxation is included by a single exponential lifetime of 700 fs, a value that many studies have reported for experiments conducted at room temperature.[13,26,45,46] Guided by changes in the FTIR spectrum of HOD upon heating, we account for thermalization effects by including a hot ground state absorption, which is blue-shifted relative to the $v=0 \rightarrow 1$ transition by $\Delta\omega = 12$ cm^{-1} and whose transition dipole is lowered by $\Delta\mu = 0.05$.[21] Reorientation of the OH dipole is described by a biexponential $P_2<\mu(t)\mu(0)>$ with both a fast 50 fs component arising from the librations of individual OH dipoles and a much slower 3 ps diffusive component.[26] Calculation of the experimental observables includes a four-fold convolution of the response function over finite duration input and local oscillator pulses. The electric fields used in the calculation were transform-limited with a duration of 45 fs and centered at 3400 cm^{-1}. The resulting 2D time domain surface is finally Fourier transformed and processed like the experimental data.

Calculated 2D IR spectra up to 700 fs can be found in Figure 5.7. Similarities between the measured data and the calculated spectra are evident. The calculated 2D line shapes have a similar waiting time behavior; surfaces at early times are diagonally elongated with the node rotating down towards the ω_1 axis with waiting time. We have analyzed the calculated 2D with the same metrics used for the experimental 2D data. The solid black lines in Figure 5.6 show the results from these calculations. Such agreement gives further evidence that $C(\tau)$ provides an average description of the spectral diffusion of the OH stretch of HOD that arises due to the structural fluctuations of the hydrogen bonding network.

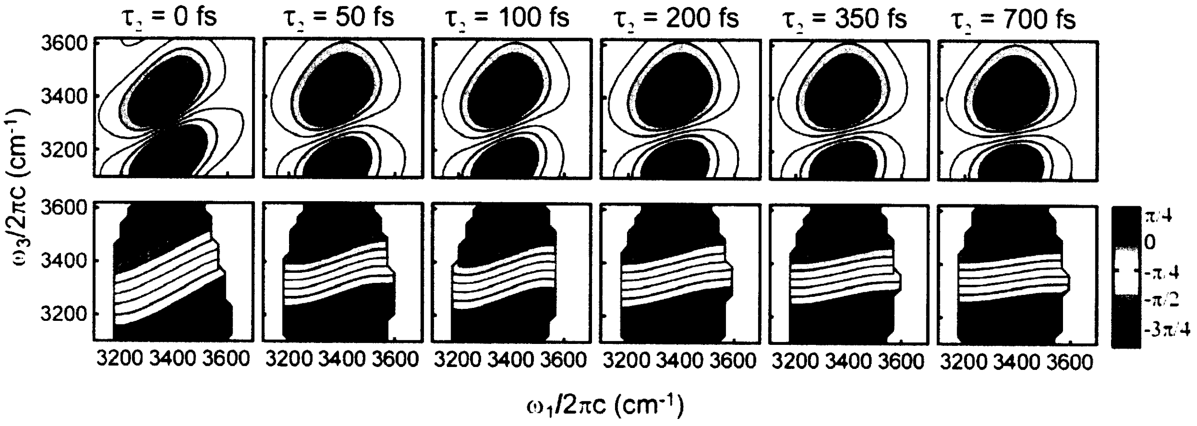

Figure 5.7 (Color) Absorptive (S'_C) and phase (S_φ) spectra for the OH stretch of HOD in D_2O calculated from the nonlinear response function formalism described in the text.

In conjunction with MD studies, the amplitudes and timescales of the decay of $C(\tau)$ can be related to fluctuations in the hydrogen bonding network that lead to spectral diffusion. At short times the dynamics of the hydrogen bonded network are dominated by fluctuations that occur on molecular length scales. The rapid dephasing observed in $C(\tau)$ arises from hindered translations and rotations of the hydrogen bond while the oscillation occurring at 180 fs illustrates that the hydrogen bond is underdamped. MD simulations confer that R_{oo}, the distance between neighboring oxygen atoms participating in a hydrogen bond, is modulated on this timescale.[4,5,7,47,48] On time scales longer than the correlation time of ~340 fs, the motions of the hydrogen bonded network begin to involve the many-body reorganization of the liquid. These are large scale motions that involve the switching of hydrogen bonded partners and diffusion. One cannot assign a well defined relaxation process to this timescale, instead MD simulations show that a number of structural order parameters, including the loss of tetrahedrality, hydrogen bond coordination, R_{oo} and the total electric field projected onto the OH bond vector decay on a ~1 ps timescale.[7]

Numerous studies have provided a characterization of the OH frequency fluctuations for HOD in D_2O. While there is not quantitative agreement between these studies, certain qualitative trends have been reproduced. In general, echo experiments have noted a time scale separation for $C(\tau)$ with ~100 fs and ~1 ps components.[7,19,20] The data presented here supports the three characteristic features of our previously extracted $C(\tau)$, a fast 60 fs decay, a damped oscillation with a 180 fs period and a long time monotonic decay of 1.4 ps. In Ref. 21, we have reviewed how our $C(\tau)$ compares to those obtained by others. Recent 2D IR experiments on the OD stretch of HOD in H_2O by Fayer and coworkers have extracted a $C(\tau)$ with decay components of 48 fs, 400 fs and a 1.4 fs.[49] While the weightings of decay components differ between the two studies the qualitative shape of 2D IR line shapes and the time scales seem to be in reasonable agreement. The comparable spectral diffusion dynamics of the HOD in D_2O and H_2O systems shows that the hydrogen bond dynamics of D_2O and H_2O are very similar. This has been commonly assumed given the near identical thermodynamic properties of the two liquids.

A comparison of the experimental 2D line shapes and those calculated in the cumulant limit shows certain differences. Deviations from Gaussian fluctuations are clearly observed as frequency-dependent broadening of the line shape as a function of waiting time. The blue (high frequency) side of the experimental line shape is broader than the red (low frequency) side. These deviations are not entirely surprising given the inability of $C(\tau)$ to predict the asymmetric 1D line shape. By the nature of the cumulant approximation, both the calculated 1D and 2D line shapes are Gaussian and therefore miss the asymmetry present in the experimental spectra. All three experimental metrics differ by a nearly constant offset from the nonlinear response function calculation. Both the experimental $I(\tau_2)$ and the slope of the node are highly sensitive to the area of integration and range in which the phase line is fit, respectively. Heterogeneous relaxation effects make these experimental observables frequency dependent. Such deviations from the Gaussian limit detail how the spectral relaxation of different hydrogen bonded configurations vary. We explore how these effects are manifestations of water's free energy landscape in Chapter 6.

5.3.2 Vibrational relaxation and thermalization

While the spectra displayed in Figure 5.1 are each normalized, the total signal intensity decays with the vibrational lifetime and as the OH dipole rotates away from the parallel polarization used in the experiments. This decay in total intensity is captured in the sum of the integrated amplitude of the absolute value rephasing and nonrephasing spectra as a function of τ_2,

$$A(\tau_2) = A_R(\tau_2) + A_{NR}(\tau_2)\,. \tag{9}$$

This amplitude, depicted in Figure 5.8, decays with a single time constant of 660 fs, tracking the loss of population as OH oscillators relax. $A(\tau_2)$ relaxes faster than the 700 fs vibrational lifetime of the OH stretch due to molecular reorientation which contributes to the relaxation in the all parallel beam geometry used in this study. Integrating over the line shape greatly suppresses the coherent signal in $A(\tau_2)$, as compared to narrowband pump-probe experiments, allowing for easier extraction of the population relaxation.

For large waiting times, the 2D line shape is well represented by the product of the linear absorption spectrum in the ω_1 and ω_3 dimensions spectrally filtered by the finite bandwidth of the excitation pulses. Figure 5.4 displays a 2D spectrum constructed from the FTIR absorption spectrum of the OH stretch of HOD in D_2O. The $v=1\rightarrow2$ spectrum has been approximated by assuming its line shape is equal to the fundamental spectrum, although shifted in frequency by the anharmonicity. Drawing on eq. 5, we have calculated the 2D line shape by incorporating the $v=1\rightarrow2$ spectrum with negative sign and adjusting the anharmonicity and the transition intensity of the v=0→1 line shape so that the projection onto the ω_1=0 axis matches the dispersed pump-probe spectrum.

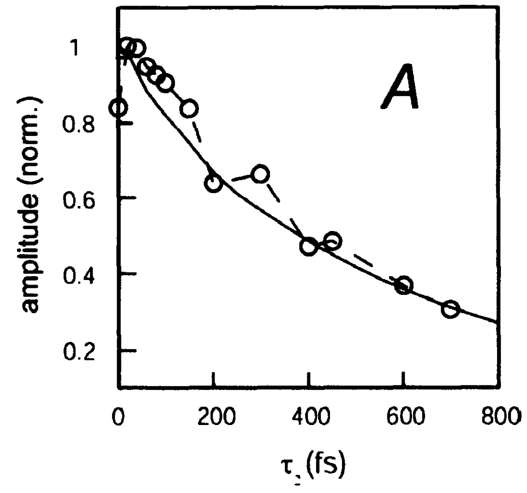

Figure 5.8 Plot of $A(\tau_2)$ tracking the decrease in the intensity of 2D IR spectra as a function of waiting time. Data is represented with open circles while the prediction from a nonlinear response function calculation is the solid line.

By 7.5 ps the 2D IR spectrum appears qualitatively different to spectra measured at earlier waiting times. Previous studies have shown that population relaxation does not refill the ground state hole, instead a spectroscopically distinct "hot ground state" (HGS) absorption is observed. The signals arising from the v=0→1 transitions of the equilibrium and hot ground state are out of phase so that the HGS absorption probed during the detection period is closely related to a temperature difference spectra. A spectrum constructed from the product of the absorption spectrum at 25°C in the ω_1 dimension with a temperature difference spectrum between absorption spectra at 25°C and 27°C in the ω_3 dimension is shown in Figure 5.4. The qualitative agreement between the 7.5 ps spectrum and the product spectrum show that 2D spectra at these waiting times are most sensitive to spectral changes resulting from the relaxation of excess energy into the surrounding medium.

Calculations of dispersed pump-probe spectra and 2D IR spectra at 2.0 and 7.5 ps drawing on our prior studies of spectral and vibrational relaxation in this system can be found in Figs. 5.3 and 5.4.[21,26] The five level system response function formalism captures the major features present in the two measurements at long waiting times: the disappearance of the v=1→2 transition, the lack of frequency correlation in 2D IR spectra and the subsequent appearance of the HGS absorption. The calculation is also able to capture more subtle features as well. A comparison of measured and calculated dispersed pump-probe spectra for waiting times of 100 fs and 7 ps can be found in Figure 5.3d. The agreement is quite good with the calculation capturing the shape and amplitude of both spectra. The solid line through Figure 5.3b shows that the calculation largely captures the shift in the maximum of the dispersed pump-probe as a function of delay time. Calculated 2D spectra are nearly identical with the product spectra in Figure 5.4 but are not in perfect agreement with the experimental surfaces. However, these differences are largely on the single contour level. Given the low amount of signal at these waiting times, differences on the ~10% should not be over interpreted.

Vibrational relaxation of HOD in D_2O is particularly well studied yet many points of contention remain. Reports of the vibrational lifetime have varied from a single time constant with values from 700 fs[13,26,46] to ~ 1 ps [50,51] to frequency dependent lifetimes that vary fairly dramatically across the band.[18] A frequency dependent lifetime should be observable in 2D IR measurements where one can distinguish between changes in frequency (spectral diffusion) as a function of waiting time and changes in intensity due to vibrational relaxation and reorientation. Although we cannot completely rule out a frequency dependent lifetime, our data shows that the effect would have to be weak. The rapid spectral diffusion measured in the 2D IR line shapes show that frequencies are scrambled within hundreds of femtoseconds, a timescale faster than the lifetime. At times greater than 2 ps, the observed signals are dominated by the response of the HGS. Failure to properly account for this response could lead to frequency dependent effects as the HGS signal varies with frequency.

Previous time-resolved studies have indicated that vibrational relaxation leads to changes in the optical properties of OH or OD transitions resulting from the heating of surrounding molecules.[19,21,26,30,31,46,52,53] Bakker and coworkers proposed that the dynamics observed in their pump-probe experiments on water could be understood in terms of a five level kinetic model in which relaxation of the excited vibrational state leads to a hot ground state that is spectroscopically distinct from the equilibrium ground state.[30] Subsequent PS experiments by Stenger et al. found a large reoccurrence in the PS at 2 ps when the excitation pulses were tuned to the red edge of the OH line shape relative to the blue.[19] These results could be modeled by extending the standard three-level response function formalism to the proposed five level system. We have adopted a similar approach for the modeling of our experiments with a slight extension to include for the decrease of the transition dipole of ω_{OH} that occurs upon heating.

Given its simplicity, our model does an excellent job of reproducing a large collection of experiments including homodyne PS, integrated PP[21] and the DPP and 2D IR measurements presented here. It should be noted that although our model captures the majority of the relevant physics it is undoubtedly too simplistic. Firstly, it only accounts for the spectral response of the HOD chromophore. Recent work by Pshenichnikov and coworkers has emphasized the nonresonant contribution from the D_2O bath molecules for timescales much greater than the vibrational lifetime.[54] These effects contribute most significantly to homodyne measurements, such as the PS, but should be present even in the absorptive signals measured here if the D_2O response is not π phase shifted from the on resonance HOD signal. In addition, our model assumes that relaxation from the OH stretch directly heats the solvent bath. Many studies have suggested that the relaxation pathway passes through at least one intermediate intramolecular state, commonly believed to be the HOD bend, before the initial excitation energy is dumped to the surrounding solvent.[51,55] We have tried adding such a state to our model but the results are inconclusive, and we are unable to suggest an effective rate constant for this process.

Comparing to studies on the OD stretch of HOD in H_2O is instructive to understanding the pathway of energy relaxation. The timescales of vibration relaxation out of the OH stretch is a factor of 2 faster than OD stretch relaxation. Given that the solvent induced forces captured by $C(\tau)$ are nearly identical, the origin of this difference must be the energy splittings between the intramolecular modes of HOD. After relaxation out of the OD stretch (1.4 ps), Steinel et al. observed an 800 fs delay in the transfer of this energy to the low frequency modes of H_2O.[31] Likewise, we observe a ~800 fs lag, as compared to the timescale of vibrational relaxation of the OH stretch, in the shift of the maximum of the fundamental transition in DPP measurements. This similarity in timescales suggests that the final transfer of energy from HOD to the surrounding solvent is largely insensitive to the isotopic mixture. Finally, it is important to note that vibration relaxation in pure H_2O is much faster than what is observed in the isotopic mixtures due to rapid energy hopping between near degenerate OH oscillators.[56-58]

5.4 Summary and conclusions

We have presented a comprehensive set of 2D IR spectra of the OH stretch of HOD in D_2O for a series of waiting times spanning the timescales of spectral diffusion and vibrational relaxation. Prior to ~1 ps the overall relaxation of the 2D IR spectra as a function of waiting time is a manifestation of the loss of frequency correlation. This global loss of frequency memory for the ensemble was analyzed with four metrics that quantify the imbalance in intensity between the rephasing and nonrephasing pathways. The inhomogeneity index, ellipticity of 2D line shapes, slope of spectral phase lines and PS were found to decay on similar timescales. Calculations of 2D IR spectra using finite duration pulses and our previously measured $C(\tau)$ were shown to evolve in the same manner as the experimental 2D surfaces with waiting time. As a measure of the timescales and amplitudes of frequency fluctuations, $C(\tau)$ can be related to the dynamics of the hydrogen bonded network. On a few hundred fs timescale, the OH oscillator experiences rapid frequency fluctuations due to hindered translations and rotations about a hydrogen bonded structure. On roughly the 1 ps timescale the hydrogen bond network rearranges through an activated barrier crossing resulting in the switching of neighboring molecules. The former process reflects the dynamics of fluctuations within a free energy minimum for a hydrogen bonded pair, whereas the latter represents the kinetics of hydrogen bonding rearrangements.

For time scales longer than the vibrational lifetime, changes in DPP and 2D IR spectra reflect the kinetics of vibrational relaxation and the subsequent thermalization of this energy by the local solvent environment. In agreement with previous measurements we found that the 1→2 transition disappeared on a ~700 fs timescale yet a positive signal shifted to lower frequency remained.[21] The lack of frequency correlation in 2D IR spectra at waiting times of 2 ps and greater indicate that this vibrational hot ground state absorption provides no insight into the equilibrium hydrogen bond dynamics of water. This is contrary to previous studies which have suggested long-lived frequency correlation in water.[19,59] Instead, the absorptive changes measured in the real part of the 2D IR spectrum and dispersed pump-probe spectra are well modeled by a simple extension to the nonlinear response function formalism to account for the shifted absorption of the HGS.

While vibrational relaxation seems to be well described by a single frequency independent lifetime, spectral diffusion is more complex. Analyzed merely in terms of a two-point frequency correlation function, the 2D IR surfaces provide roughly the same information compared to more easily implemented nonlinear experiments such as the homodyne PS. Although such integrated measurements contain contributions from both the fundamental and overtone transitions, the relative good agreement between the observables extracted from the experimental 2D IR surfaces presented here and the calculated results show that harmonic scaling is a reasonable approximation of the frequency fluctuations of the v=1→2 transition. In many ways this is not surprising as third order experiments should not be particularly sensitive to the frequency fluctuations of the overtone transition because a coherence can only evolve in this state during the detection period. The 2D IR spectra shown here also show clear signatures of frequency-dependent spectral diffusion that cannot be observed with simpler experiments and is not explained by Gaussian dynamics.[29,60] I quantify these effects as a function of waiting time in Chapter 6 and interpret them in terms of the dynamics of different hydrogen bonded environments.[61]

References

[1] R. Jimenez, G. R. Fleming, P. V. Kumar, and M. Maroncelli, Nature 369, 471 (1994).

[2] N. Agmon, Chem. Phys. Lett. 244, 456 (1995).

[3] P. G. Debenedetti and F. H. Stillinger, Nature 410, 259 (2001).

[4] I. Ohmine and S. Saito, Acc. Chem. Res. 32, 741 (1999).

[5] R. Rey, K. B. Moller, and J. T. Hynes, J. Phys. Chem. A 106 (50), 11993 (2002).

[6] C. P. Lawrence and J. L. Skinner, Chem. Phys. Lett. 369, 472 (2003).

[7] C. J. Fecko, J. D. Eaves, J. J. Loparo, A. Tokmakoff, and P. L. Geissler, Science 301, 1698 (2003).

[8] J. D. Eaves, A. Tokmakoff, and P. Geissler, J. Phys. Chem. A 109, 9424 (2005).

[9] S. A. Corcelli, C. P. Lawrence, and J. L. Skinner, J. Chem. Phys. 120, 8107 (2004).

[10] K. B. Moller, R. Rey, and J. T. Hynes, J. Phys. Chem. A 108, 1275 (2004).

[11] T. Hayashi, T. l. C. Jansen, W. Zhuang, and S. Mukamel, J. Phys. Chem. A 109 (1), 64 (2005).

[12] W. Mikenda, J. Mol. Struct. 147, 1 (1986).

[13] S. Woutersen, U. Emmerichs, H.-K. Nienhuys, and H. J. Bakker, Phys. Rev. Lett. 81, 1106 (1998).

[14] S. Woutersen, U. Emmerichs, and H. J. Bakker, Science 278, 658 (1997).

[15] G. M. Gale, G. Gallot, F. Hache, N. Lascoux, S. Bratos, and J.-C. Leicknam, Phys. Rev. Lett., 1068 (1999).

[16] R. Laenen, K. Simeonidis, and A. Laubereau, J. Phys. Chem. B 106 (408-417) (2002).

[17] Z. Wang, A. Pakoulev, Y. Pang, and D. D. Dlott, J. Phys. Chem. A 108, 9054 (2004).

[18] G. M. Gale, G. Gallot, and N. Lascoux, Chem. Phys. Lett. 311, 123 (1999).

[19] J. Stenger, D. Madsen, P. Hamm, E. T. J. Nibbering, and T. Elsaesser, J. Phys. Chem. A 106 (10), 2341 (2002).

[20] S. Yeremenko, M. S. Pshenichnikov, and D. A. Wiersma, Chem. Phys. Lett. 369, 107 (2003).

[21] C. J. Fecko, J. J. Loparo, S. T. Roberts, and A. Tokmakoff, J. Chem. Phys. 122, 054506 (2005).

[22] J. B. Asbury, T. Steinel, C. Stromberg, S. A. Corcelli, C. P. Lawrence, J. L. Skinner, and M. D. Fayer, J. Phys. Chem. A 108, 1107 (2004).

[23] W. de Boeij, M. S. Pshenichnikov, and D. A. Wiersma, Chem. Phys. Lett. 253, 53 (1996).

[24] A. Piryatinski and J. L. Skinner, J. Phys. Chem. B. 106, 8055 (2002).

[25] M. Cho, J.-Y. Yu, T. Joo, Y. Nagasawa, S. A. Passino, and G. R. Fleming, J. Phys. Chem. 100, 11944 (1996).

[26] J. J. Loparo, C. J. Fecko, J. D. Eaves, S. T. Roberts, and A. Tokmakoff, Phys. Rev. B 70, 180201 (2004).

[27] M. Khalil, N. Demirdoven, and A. Tokmakoff, J. Phys. Chem. A 107 (27), 5258 (2003).

[28] J. D. Hybl, A. Yu, D. A. Farrow, and D. M. Jonas, J. Phys. Chem. A 106 (34), 7651 (2002).

[29] J. D. Eaves, J. J. Loparo, C. J. Fecko, S. T. Roberts, A. Tokmakoff, and P. L. Geissler, Proc. Natl. Acad. Sci. USA 102, 13019 (2005).

[30] A. J. Lock, S. Woutersen, and H. J. Bakker, J. Phys. Chem. A 105, 1238 (2001).

[31] T. Steinel, J. B. Asbury, J. Zheng, and M. D. Fayer, J. Chem. Phys., 108, 10957 (2004).

[32] M. Khalil, N. Demirdöven, and A. Tokmakoff, Phys. Rev. Lett. 90, 47401 (2003).

[33] H. Kano and T. Kobayashi, Opt. Commun. 178, 133 (2000).

[34] J. D. Hybl, A. A. Ferro, and D. M. Jonas, J. Chem. Phys. 115, 6606 (2001).

[35] S. Mukamel, *Principles of Nonlinear Optical Spectroscopy*. (Oxford University Press, New York, 1995).

[36] T. Joo, Y. Jia, J.-Y. Yu, M. J. Lang, and G. R. Fleming, J. Chem. Phys. 104, 6089 (1996).

[37] W. P. de Boeij, M. S. Pshenichnikov, and D. A. Wiersma, Annu. Rev. Phys. Chem. 49, 99 (1998).

[38] P. Hamm, M. Lim, and R. M. Hochstrasser, Phys. Rev. Lett. 81, 5326 (1998).

[39] K. Ohta, H. Maekawa, and K. Tominaga, J. Phys. Chem. A 108, 1333 (2004).

[40] S. T. Roberts, J. J. Loparo, and A. Tokmakoff, J. Chem. Phys. 125, 084502 (2006).

[41] K. Lazonder, M. S. Pshenichnikov, and D. Wiersma, Pacific Grove, 2006 (unpublished).

[42] T. Brixner, I. V. Stoipkin, and G. R. Fleming, Opt. Lett. 29, 884 (2004).

[43] K. Kwac and M. Cho, J. Chem. Phys. 119, 2256 (2003).

[44] J. Sung and R. J. Silbey, J. Chem. Phys. 115, 9266 (2001).

[45] S. Woutersen and H. J. Bakker, Phys. Rev. Lett. 83, 2077 (1999).

[46] M. S. Pshenichnikov, S. Yeremenko, and D. A. Wiersma, in *Ultrafast Phenomena XIV*, edited by T. Kobayashi, T. Okada, T. Kobayashi, K. A. Nelson, and S. DeSilvestri (Springer Verlag, Berlin, Niigata, Japan, 2005), pp. 404.

[47] A. Rahman and F. H. Stillinger, J. Chem. Phys. 55, 3336 (1971).

[48] C. P. Lawrence and J. L. Skinner, J. Chem. Phys. 118, 264 (2003).

[49] J. B. Asbury, T. Steinel, K. Kwak, S. A. Corcelli, C. P. Lawrence, J. L. Skinner, and M. D. Fayer, J. Chem. Phys. 121, 12431 (2004).

[50] R. Laenen, C. Rauscher, and A. Laubereau, J. Phys. Chem. B 102, 9304 (1998).

[51] J. C. Deak, S. T. Rhea, L. K. Iwaki, and D. D. Dlott, J. Phys. Chem. A 104, 4866 (2000).

[52] M. S. Pshenichnikov, S. Yeremenko, and D. A. Wiersma, in *Femtochemistry and Femtobiology: Ultrafast Events in Molecular Science*, edited by M. M. Martin and J. T. Hynes (Elsevier, Amsterdam, 2004).

[53] J. B. Asbury, T. Steinel, C. Stromberg, K. J. Gaffney, I. R. Piletic, and M. D. Fayer, J. Chem. Phys. 119 (24), 12981 (2003).

[54] S. Yeremenko, M. S. Pshenichnikov, and D. Wiersma, Phys. Rev. A 73, 021804 (2006).

[55] C. P. Lawrence and J. L. Skinner, J. Chem. Phys. 119 (3), 1623 (2003).

[56] S. Woutersen and H. J. Bakker, Nature 402, 507 (1999).

[57] M. L. Cowan, B. D. Bruner, N. Huse, J. R. Dwyer, B. Chugh, E. T. J. Nibbering, T. Elsaesser, and R. J. D. Miller, Nature 434 (2005).

[58] J. Linder, P. Vohringer, M. S. Pshenichnikov, D. Cringus, D. Wiersma, and M. Mostovoy, Chem. Phys. Lett. 421, 329 (2006).

[59] T. l. C. Jansen, T. Hayashi, W. Zhuang, and S. Mukamel, J. Chem. Phys. 123, 114504 (2005).

[60] T. Steinel, J. B. Asbury, S. A. Corcelli, C. P. Lawrence, J. L. Skinner, and M. D. Fayer, Chem. Phys. Lett. 386, 295 (2004).

[61] J. J. Loparo, S. T. Roberts, and A. Tokmakoff, J. Chem. Phys. 125, 194522 (2006).

Chapter 6

Multidimensional infrared spectroscopy of water. Hydrogen bond switching dynamics

6.1 Introduction

In ice the positions of each water molecule are well defined by the hexagonal crystalline unit cell and the local tetrahedral symmetry of oxygens that results from the formation of hydrogen bonds. In the liquid, the first solvent shell to any molecule remains tetrahedral on average but lacks ~10% of the hydrogen bonds formed in the crystal.[1-3] The liquid's fluid properties are governed by intermolecular fluctuations on femtosecond (fs) time scales and hydrogen bonding rearrangements on a roughly 1 picosecond time scale.[4-9] The dynamics of water's hydrogen bonding network complicate the ability to experimentally reveal information on water's structure, the nature of broken hydrogen bonds, and the mechanism by which molecules switch hydrogen bonding partners. As of yet no experimental technique is able to provide a statistical description of water's time-evolving hydrogen bonding structure with atomistic detail.

Conceptual views of water's structure, drawn from decades of experiments and computer simulations, have often been broken into two classes, mixture and continuum models.[1,10] Mixture models conceive of liquid water as composed of two or more stable species that differ in their hydrogen bonding configurations.[11-13] Continuum models do not identify different species, but conceive of the structure as a continuous distribution of geometries or large distortions about an average structure.[3,14-16] While these models have existed for a century or more, debate regarding their validity still persists. Interpretations based on mixture models are omnipresent in spectroscopic studies of water. It is assumed when fitting components to spectra (each of which is a stable component with a minimum lifetime given by the inverse of the linewidth),[17-28] when interpreting isosbestic points in the temperature dependent spectroscopy of water,[12,26,28]and in the perspective that liquid water can be conceived as isomers of water clusters[29]. Recently, debate over the analysis of x-ray absorption experiments is a poignant example of the arguments presented for and against these two different perspectives.[10,25,30]

Analysis of molecular dynamics (MD) simulations has been used to argue various perspectives. Hydrogen bond kinetics are often analyzed in terms of a two state description in which the presence or absence of a hydrogen bond is defined through geometrical or energetic criteria.[31-34] The instantaneous snapshots of water's evolving structure in MD characterize the distribution of hydrogen bonding configurations,[23,35] but interpretations vary about the chemical relevance of different instantaneous structures. MD has also emphasized that hydrogen bonding and inherent structures must be understood collectively.[6,36,37]

Explicitly or implicitly, the conceptual pictures of water structure and hydrogen bond rearrangements differ in the assignment of intermolecular configurations to stable states: those defined by minima on a free energy surface and separated from each other by a barrier >kT. For this reason, the discussion of hydrogen-bond dynamics is crucial to the interpretation of water structure. Hydrogen bonded water molecules experience fs translational and orientational fluctuations that lead to significant but short-lived distortions of local structure. The finite lifetime of these strained configurations means that instantaneous observations of intermolecular structure cannot be used to interpret their stability. On the other hand dynamical measures that characterize the persistence time of configurations relative to the intermolecular fluctuations of the liquid provide a measure of stability useful in characterizing the presence of barriers and describing water's fluctuating structure.[1,38,39]

As an example of how dynamics and stability are critical to understand water's hydrogen bond network, consider the mechanism by which a water molecule breaks a hydrogen bond with one molecule and forms a new bond with a neighboring molecule. To illustrate, consider two limiting perspectives which differ by their interpretation of non-hydrogen bonded configurations (NHB), the strained intermolecular configurations whose geometry would not conventionally be termed a hydrogen bond. In one limit, the NHB represents a metastable configuration. A thermal fluctuation ruptures a hydrogen bond, but the disorder of the liquid means a new hydrogen bond acceptor is not readily available. This NHB is entropically stabilized and referred to as a dangling hydrogen bond. As an alternative picture, the NHB state appears (and subsequently disappears) due to fluctuations about a hydrogen bond or in a concerted switching of hydrogen bonded partners. These two pictures do not differ in terms of instantaneous structures, but rather by whether the NHB persist longer or shorter than the time scale for intermolecular fluctuations.

Infrared spectroscopy of the OH stretching vibration of HOD in D_2O provides an avenue to distinguish these scenarios. As a sensitive probe of its local environment, the intramolecular OH stretching frequency, ω_{OH}, depends on the hydrogen bond coordination of the proton. OH oscillators in solvents incapable of forming hydrogen bonds possess a free OH resonance similar in width and frequency to the gas phase value while hydrogen bonding leads to a weakening of the OH force constant and a significant red shift and broadening of the absorption spectrum.[40-42] As shown in Figure 6.1a, configurations from MD simulations confirm that the 10% of molecules that lie outside of geometrical hydrogen bonding criteria absorb preferentially on the high frequency (blue) side of the spectrum, while the low-frequency (red) side arises from the molecules in strong, linear hydrogen bonds with its neighboring acceptor molecule (HB).[39,43]

In principle, femtosecond IR spectroscopies that probe the time evolution of ω_{OH} should be able to follow the exchange between HB and NHB environments and shed light on the mechanism of hydrogen bond switching and the stability of NHB species. Figures 6.1b and 6.1c show two free energy surfaces that describe the changes in ω_{OH} during the exchange of hydrogen bonding partners for the two models described above. These pictures can be classified as the step-wise and concerted mechanisms for hydrogen bonding rearrangements, and are closely related to mixture or continuum descriptions of water. In Figure 6.1b, NHB configurations represent a metastable state that exchanges with the HB state at a rate given by the free energy barrier. HB and NHB would be distinguished by a separation of timescales for fast fluctuations within wells and the crossing of the barrier between them. On the other hand if the NHBs are intrinsically unstable as in Figure 6.1c, they will return to a hydrogen bonded configuration on the timescale of intermolecular motions. Therefore, the persistence time of NHB species relative to the fastest fluctuations of the system serves as an experimental measure of their stability.

The persistence time of NHBs can be characterized with two dimensional infrared spectroscopy (2D IR). 2D IR is able to follow the frequency evolution of OH oscillators as they convert between HB and NHB with a time resolution set by the fastest motions of the liquid. A 2D IR correlation spectrum, displayed as a function of two frequency axes (ω_1 and ω_3), is closely related to the joint probability that a molecule has an initial excitation frequency, ω_1, and arrives at a target frequency, ω_3, after a waiting time, τ_2. 2D IR spectra as a function of τ_2 probe the stability of hydrogen bonded species by measuring the spectral relaxation of OH oscillators initially located at different parts of the line shape.

Utilizing the 2D line shapes presented in the preceeding chapter, I examine the molecular origins of the frequency dependent spectral evolution of the OH line shape of HOD, and use it to resolve the distinct relaxation of HB and NHB species. In conjugation with molecular dynamics (MD) simulations, the experimental 2D IR surfaces and their waiting time dependence are interpreted in terms of the interconversion of HB and NHB environments. I find that 2D IR line shapes that are preferentially broader on the blue (high frequency) side are a clear indication of barrierless relaxation from NHB configurations back to the HB state. These results argue for the perspective portrayed in Figure 6.1c, and have clear implications for water structure, the mechanism of hydrogen bond rearrangements in water, and working definitions for what determines a hydrogen bond.

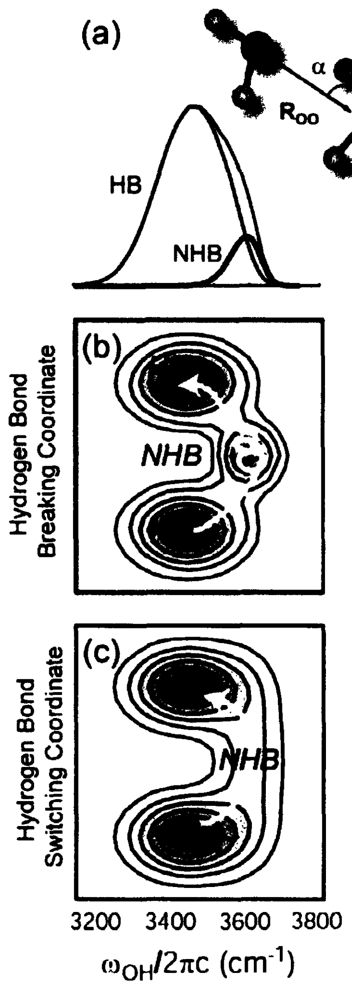

Figure 6.1. (Color) (a) OH stretching frequency distribution calculated from MD simulations. Geometric criteria ($R_{oo} < 3.5$ Å and $\theta < 30°$) are used to distinguish instantaneous HB and NHB configurations. Free energy landscapes describing hydrogen bond switching where the NHB state occupies a local minimum (b) or is a transition state (c). Free energy surfaces were constructed so that the projection onto the ω_{OH} axis is equal to the free energy of the OH frequency distribution.

6.2 Methods

A full description of the experimental acquisition of absorptive 2D IR spectra is detailed in Chapter 3.

To help interpret the microscopic origin of the experimentally characterized vibrational dynamics, molecular dynamics (MD) simulations employing the conventional SPC/E water potential were carried out. The strategies employed during these simulations have been described previously[43,44], however the salient details are briefly recounted here. 1.5 ns long trajectories of a single HOD molecule surrounded by 107 D_2O molecules were computed using the Velocity-Verlet algorithm[45], periodic boundary conditions, and a 3 fs time step. Periodic rescaling of the velocities was performed to ensure that the temperature did not significantly deviate from 298K. The MD trajectories were used to calculate 2D IR spectra using an atomistic model that has recently been described.[39] The model employs a Hamiltonian, $H = H_S + H_{SB} + H_B$, which describes the interaction of a single quantum mechanical degree of freedom, the OH vibration (H_S), with the classical translational and rotational degrees of freedom of the simulation (H_B). H_S is taken from the gas phase potential of Reimers and Watts.[46] Since the bath coordinates are much slower motions than the vibration of the OH bond, we make an adiabatic separation between the system and bath coordinates. For any given configuration of the bath molecules the coupling between the system and the bath, H_{SB}, is only a function of the system coordinate. We can then calculate H_{SB}, which gives the time-dependent OH frequency shifts from the gas phase value, by using second order perturbation theory.

With an OH frequency trajectory it is then possible to calculate 2D IR spectra and other nonlinear spectroscopic signals based on four-point correlation functions of the dipole operator. Within the Condon approximation, where the magnitude of each of the transitions dipoles is assumed to be constant, the rephasing and nonrephasing response functions for a single anharmonic system vibration can be written as[47,48]:

$$R_{\pm}\left(\tau_1,\tau_2,\tau_3\right)=2\left|\mu_{10}\right|^4\left\langle \exp\left[\pm\int_0^{\tau_1} dt\omega_{10}(t)+\int_{\tau_1+\tau_2}^{\tau_1+\tau_2+\tau_3} dt'\omega_{10}(t')\right]\right\rangle \\ -\left|\mu_{10}\right|^2\left|\mu_{21}\right|^2\left\langle \exp\left[\pm\int_0^{\tau_1} dt\omega_{10}(t)+\int_{\tau_1+\tau_2}^{\tau_1+\tau_2+\tau_3} dt'\omega_{21}(t')\right]\right\rangle , \qquad (1)$$

where the "+" sign refers to nonrephasing and the "–" sign to rephasing response functions. Here $\omega_{nm} = (E_n(t)-E_m(t))/\hbar$. For the purposes of this paper, response functions were obtained from ten separate 1.5 ns MD trajectories and averaged together. Two dimensional Fourier transformation of the averaged time domain signal with respect to τ_1 and τ_3 gives the complex 2D spectrum.

Frequency trajectories were also used to calculate the joint probability of being at a particular initial frequency ω_1 and reaching a target frequency ω_3 after a time τ_2

$$P\left(\omega_3,\tau_2\middle|\omega_1\right)=\left\langle\delta\left(\omega_{10}(\tau_2)-\omega_3\right)\delta\left(\omega_{10}(0)-\omega_1\right)\right\rangle . \qquad (2)$$

As discussed in Chapter 5 this is equivalent to the 2D line shape in the limit that there is no change of frequency during τ_1 and τ_3.[49]

6.3 Results and analysis

6.3.1 Frequency-dependent spectral relaxation

Figure 6.2 shows OH stretching absorptive correlation spectra for waiting times between 0 and 700 fs. The spectra show two features, a positive going peak due to the transient bleach of the 0→1 transition and an anharmonically shifted negative going induced absorption due to the 1→2 transition. The 2D IR spectra show signs of frequency-dependent line broadening, indicating a deviation from Gaussian OH frequency fluctuations. This can be seen by comparing to the line shapes predicted on the basis of Gaussian statistics in Figure 5.8. Inspection of the $\tau_2=0$ 2D IR surface indicates that in addition to the diagonal elongation characteristic of an inhomogeneous system, the oscillators prepared on the red and blue sides of the line shape undergo qualitatively different frequency relaxation. For an inhomogeneous 2D line shape, the diagonal ($\omega_1=\omega_3$) and anti-diagonal ($\omega_1+\omega_3=2\Omega$) widths are related to the inhomogeneous frequency distribution and homogeneous linewidth, respectively.[50] For a heterogeneous system, one in which the microscopic dephasing varies with environment and resonance frequency, one expects that the antidiagonal linewidth will also vary across the line shape.[51] Anti-diagonal slices taken on the red (Ω_{red} =3290 cm^{-1}) and blue (Ω_{blue} =3520 cm^{-1}) sides of the line shape through the $\tau_2=0$ surface are shown in Figure 6.3. Slices from the diagonal outward are shown to avoid interference from the negative 1→2 transition. Half widths of the antidiagonal slices are broader for the blue side than the red indicating that the dynamics on the blue side are faster. These frequency dependent linewidths are not observed in models with Gaussian statistics (see Figure 5.8).

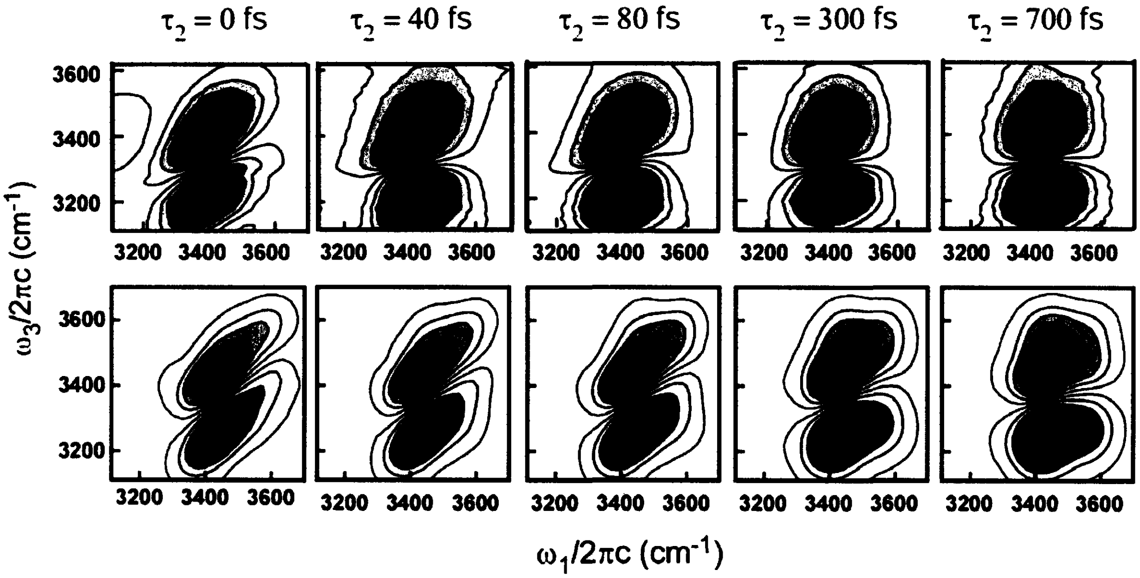

Figure 6.2 (Color) Experimental (top) and simulated (bottom) absorptive 2D IR correlation spectra, $S_C^{'}$, for the listed waiting times.

The antidiagonal slices for the τ_2=0 surface also quantify the intrinsic measurement timescale of the experiment. Even with infinitely fast pulses, the spectral relaxation is averaged over an experimental timescale set by the underlying dynamics and the persistence times of hydrogen bonding configurations. This is approximately equal to the sum of τ_2 and the time for the signal to decay in τ_1 and τ_3. The projection slice theorem of 2D spectroscopy[52] indicates that the decay of the time-domain signal, longest along the echo ridge τ_1=τ_3, is inversely related to the linewidth of the 2D spectrum projected onto the antidiagonal frequency axis. Thus, in a heterogeneous system, antidiagonal slices at a given frequency Ω can be related to the minimum average time scale for which oscillators persist at that frequency. In the present case, the antidiagonal linewidth of the projected τ_2=0 spectrum is 45 cm^{-1} (HWHM) indicating a time resolution of 185 fs. Asymmetry in the τ_2=0 2D line shape indicates that this time scale varies from 275 fs at Ω_{red} = 3290 cm^{-1} to 150 fs at Ω_{blue} = 3520 cm^{-1}.

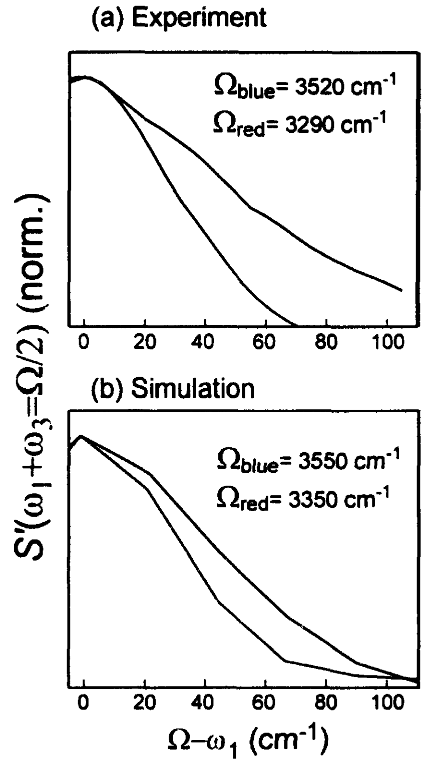

Figure 6.3. (Color) Anti-diagonal slices taken through the (a) experimental and (b) simulated τ_2 = 0 2D IR surface. Half widths are plotted from the diagonal outwards to avoid the interference from the v = 1→2 transition. The frequencies in which the slices were taken were chosen so that they would correspond to roughly equal intensity level on the red and blue sides of the line shape.

When the waiting time is nonzero, the intrinsic timescale of the 2D IR experiment increases as the system is allowed to evolve during τ_2 and molecules exchange environments. The frequency dependent broadening of the 2D IR line shape with waiting time provides the most intuitive measure of the exchange of molecules between different hydrogen bonding environments. Slices through the absorptive 2D spectrum for $\omega_1 = \Omega$, shown in Figure 6.4, can be roughly interpreted as the OH frequency distribution observed after excitation at Ω and waiting a time τ_2. One dimensional slices for $\omega_1 = 3530$ cm^{-1} through the 2D spectra as a function of τ_2 show the fast spectral diffusion of oscillators on the blue side of the line shape. Prior to $\tau_2 = 100$ fs, the blue side of the 2D line shape undergoes significant change while the red side remains largely the same (see Figure 6.4). As already noted, at $\tau_2=0$ the 2D line shape is elongated along the diagonal, thus the slice is centered at roughly 3530 cm^{-1}. By a waiting time of 40 fs this distribution has rapidly broadened and shifted toward band center. The evolution of the blue side of the line shape is largely complete by a waiting time of 80 fs as the distribution of oscillators originally at 3530 cm^{-1} has nearly returned to band center (~3400 cm^{-1}). Slices taken at longer waiting times remain largely unchanged. Qualitatively different behavior is observed for slices taken through the red side of the 2D line shape at $\omega_1 = 3250$ cm^{-1}. These slices show little evolution from $\tau_2=0$ to 80 fs. By $\tau_2 = 300$ fs the slice has moved back toward band center with only small changes observed afterward.

The waiting time dependence of these slices can be quantified by calculating the first moment of the positive signal distribution, which is shown in Figure 6.5. The first moment for slices taken from the blue side of the 2D IR line shape decays monotonically with an approximate time constant of 60 fs, reaching its asymptotic value by τ_2=100 fs. The first moment for slices from the red side is much different, exhibiting a large oscillation observed at ~130 fs and a slower return to the band center. These observations indicate that molecules prepared at high frequencies in strained or non-hydrogen-bonding configurations relax rapidly toward the equilibrium hydrogen bonded distribution. The molecules excited on the red (hydrogen bonding) side, show underdamped oscillations of the hydrogen bond prior to a longer decay. The marked differences in spectral relaxation behavior can be compared to the predictions based on the model with Gaussian fluctuations (Figure 5.8), which show the same relaxation on either side of line center for $\tau_2 > 30$ fs.

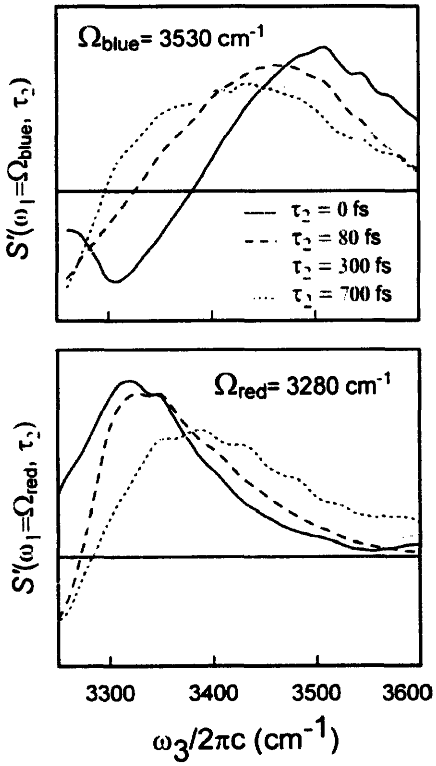

Figure 6.4. Slices through the experimental 2D IR correlation spectrum for $\omega_1 = \Omega$ on the red and blue edges of the line shape and the specified values of τ_2. Slices were normalized to the positive area under each from the zero crossing outward.

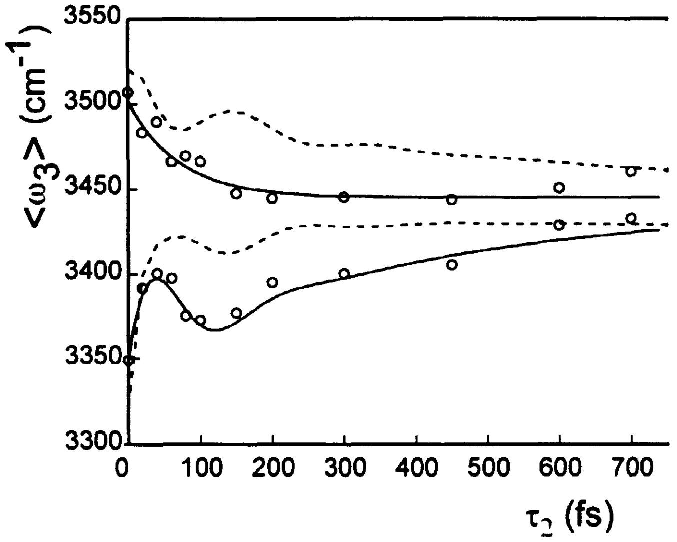

Figure 6.5. (Color) First moment for ω_1 slices as a function of τ_2. Circles depict the data points, the solid lines are guides for the eye while the dashed lines are the anticipated result from nonlinear response function calculations described in Chapter 5.

In Chapter 5 we showed how the equalizing of rephasing and nonrephasing intensities as a function of τ_2, accompanied the loss of frequency memory.[49,53] To quantify heterogeneity in these spectral dynamics, we can extend these metrics to look at their frequency dependence. Figure 6.6 displays a contour plot of the inhomogeneity index across the 2D IR spectrum for τ_2=0. This plot illustrates the fairly significant change in I across the 2D line shape as anticipated from the asymmetric line shape described above. Averaging a small area about the red and blue edges of the 2D line shape along the diagonal axis yields $I(\Omega,\tau_2)$:

$$I(\Omega,\tau_2)=\frac{A_R(\omega_1,\tau_2,\omega_3)-A_{NR}(\omega_1,\tau_2,\omega_3)}{A_R(\omega_1,\tau_2,\omega_3)+A_{NR}(\omega_1,\tau_2,\omega_3)} \qquad (3)$$

where A is the rephasing or nonrephasing absolute value spectrum and Ω refers to the frequency range in ω_1 and ω_3 over which I is averaged. On the blue side of the line shape,

$I(\Omega_{blue},\tau_2)$ is near 0 for all values of τ_2, indicating that there is little to no frequency correlation between the evolution and detection periods. This is characteristic of homogeneous line broadening. In contrast, on the red side the initial value of $I(\Omega_{red},\tau_2)$ = ~0.35 indicates a modest frequency memory between τ_1 and τ_3 that is intermediate to the homogeneous ($I = 0$) and inhomogeneous ($I = 1$) limits. This measure decays away with τ_2, decaying to 0.05 by $\tau_2 = 400$ fs.

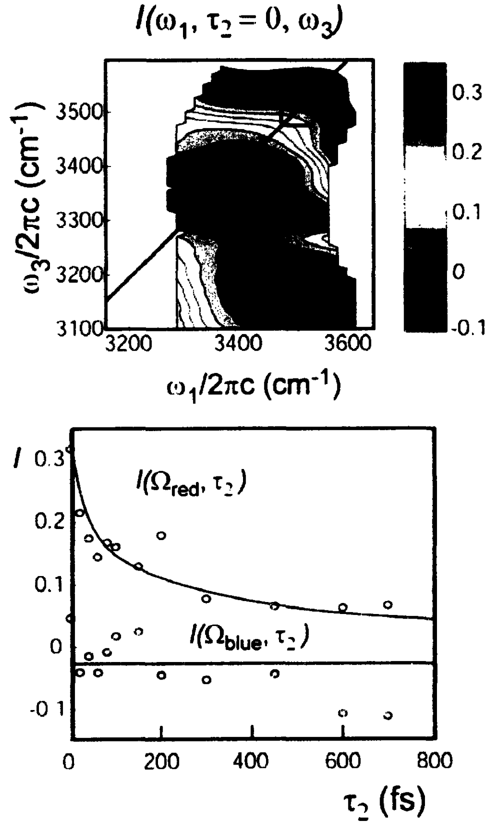

Figure 6.6. (Color) A 2D surface (top) depicting $I(\omega_1, \tau_2 = 0, \omega_3)$. Black boxes indict areas of integration used to determine $I(\Omega, \tau_2)$ plotted below. Integration on the red side of the line was from 3285-3335 cm^{-1} in both the ω_1 and ω_3 dimensions while the blue side was integrated from 3485-3515 cm^{-1}. The bottom panel depicts the τ_2 dependence of these integrated areas. The solid lines are to guide the eye.

Similarly, we can probe relaxation heterogeneity by evaluating the slope of phase lines $\beta = \partial\phi/\partial\omega_1$ at $\omega_1=\omega_3=\Omega_{red}$ and $\omega_1=\omega_3=\Omega_{blue}$ as a function of τ_2. The top panel of Figure 6.7 shows the phase spectrum for $\tau_2 = 0$. The lines on this contour plot indicate constant values of spectral phase while the curvature of these lines, with higher slopes on the red than the blue, is another indicator of increasingly fast spectral relaxation as the initial OH frequency is increased. The dashed lines depict where slices where taken through the phase spectrum. Similar to *I*, the relaxation of β with τ_2, shown in the bottom panel of Figure 6.7, is essentially complete from the earliest moments on the blue side, but relaxes monotonically over the course of a few hundred femtoseconds on the red side.

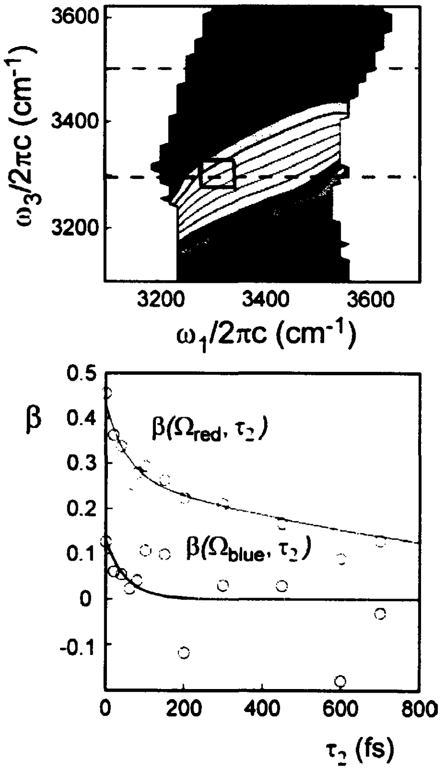

Figure 6.7. (Color) The top panel depicts the phase representation of the τ_2 = 0 fs spectrum.[49] Dashed lines represent the direction in which slices were taken while the black boxes depict the frequency range (Ω_{red} = 3285-3335 cm^{-1} and Ω_{blue} = 3485-3515 cm^{-1}). The average slope of these phase lines is plotted in the bottom panel as a function of τ_2. The solid lines are to guide the eye.

6.3.2 Origins of spectral relaxation

To better understand the differences observed on the red and blue side of the line shape in terms of the underlying hydrogen bond rearrangements, one needs to first examine the origin of the HB and NHB frequency distribution plotted in Figure 6.1a. A number of recent theoretical studies drawing on MD simulations have concluded that ω_{OH} is determined by the total electric field that surrounding molecules project onto the OH bond vector.[8,43,54-56] Of all molecules, the hydrogen bond accepting oxygen is the prominent contributer to the total electric field, allowing the OH frequency imposed by the hydrogen bond acceptor configuration to be approximated in terms of the position of the hydrogen bonding distance R_{OO} and angle α.[43] Because ω_{OH} is determined by $\cos \alpha$, angular fluctuations lead to only small changes in frequency. Through reorientation, a NHB cannot change frequency more than ~2% without assuming an HB configuration. Therefore the significant shift of frequency observed from the blue side of the line toward band center must involve motion into a hydrogen-bonded configuration. The formation of a hydrogen bond orients the partial negative charge of the acceptor oxygen towards the proton and narrows the range of hydrogen bonding angles. Here, hydrogen bond stretching strongly influences ω_{OH}; a change of R_{OO} by 0.3Å can result in an 8% (~250 cm^{-1}) change in ω_{OH}. Thus molecules that are prepared and persist in strongly-hydrogen bonded configurations are expected to show an OH frequency modulated by hydrogen bond vibrations, as seen in our data.

If one neglects the underlying differences in dynamics, the observation that the blue side of the 2D line shape is broader than the red is a counterintuitive result. Experimental studies over several decades have revealed a correlated red shift of ω_{OH} and broadening of the FWHM of the linewidth, Γ_{FWHM}, for a variety of species as hydrogen bond strength to the solvent increases.[40,41] We confirm this explicitly for the OH stretching vibration of HOD in Figure 6.8. The OH absorption spectrum was measured for a dilute solution of HOD in D_2O added to solvents with varying hydrogen bond interaction strengths. As the interaction strength between solvent and HOD decreases, the OH frequency and linewidth approaches the limiting gas phase value. This is observable in Figure 6.8a where the absorption spectra of HOD in D_2O, tetrahydrofuran and chloroform-*d* are plotted.

The quadratic relationship between ω_{OH} and Γ_{FWHM} observed in Figure 6.8b can be understood simply when the frequency shifts originate in the electric field. In this case the mean absorption frequency $\langle\omega_{OH}\rangle$ is linearly proportional to the electric field acting on the coordinate, as is the anharmonicity $\Delta = \omega_{10} - \omega_{21}$.[57] Examining Γ_{FWHM} within a Gaussian-stochastic model with a correlation time τ_c, Γ_{FWHM} is proportional either to $\langle\delta\omega_{OH}^2\rangle\tau_c$ in the homogeneous limit, or just $\langle\delta\omega_{OH}^2\rangle$ in the inhomogeneous limit. The mean square value of fluctuations is directly proportional to $\langle E^2\rangle$. This leads to a quadratic dependence of Γ_{FWHM} on frequency, which may be somewhat moderated by changes in the individual liquid's dynamics.

These observations allow us to predict the 2D IR spectrum for a hydrogen bonding system with a continuous distribution of stable environments that differ in the strength of hydrogen bonding interaction. This model would apply to the case where strong hydrogen bonding environments interchange with weaker or broken hydrogen bonding environments through activated processes on time scales longer that the intermolecular motions or frequency correlation time. This is an extension of the trajectory pictured in Figure 6.1b to the case with multiple wells with barrier heights greater than kT. In this limit, the IR line shape and $\tau_2 = 0$ 2D IR line shapes can be expressed in terms of a sum over independent contributions from each microstate weighted by their probability density: $S(\omega) = \Sigma_i P_i S_i(\omega)$. Such models are widely used to express the broadened OH stretching line shape in terms of constituent species.[18,19,26,28,58] The relationship between ω_{OH} and Γ_{FWHM} for each state is plotted in Figure 6.8b. The Gaussian distribution of states is chosen so that the resulting sum over states approximately reproduces the absorption maximum and linewidth of the FTIR line shape (see top panel of Figure 6.8c). A calculation of the 2D IR spectrum proceeds similarly, but accounting for the fourth order scaling of the amplitude in the dipole moment and including a linear dependence of anharmonicity on frequency and harmonic scaling of the $v=1\rightarrow2$ amplitudes. The resulting line shape is pictured in Figure 6.8c. The continuous distribution of stable species with varying hydrogen bond strength leads to a 2D line shape that is preferentially broadened on the red side relative to the blue. This is in contrast to the experimental 2D line shape which observes the opposite trend.

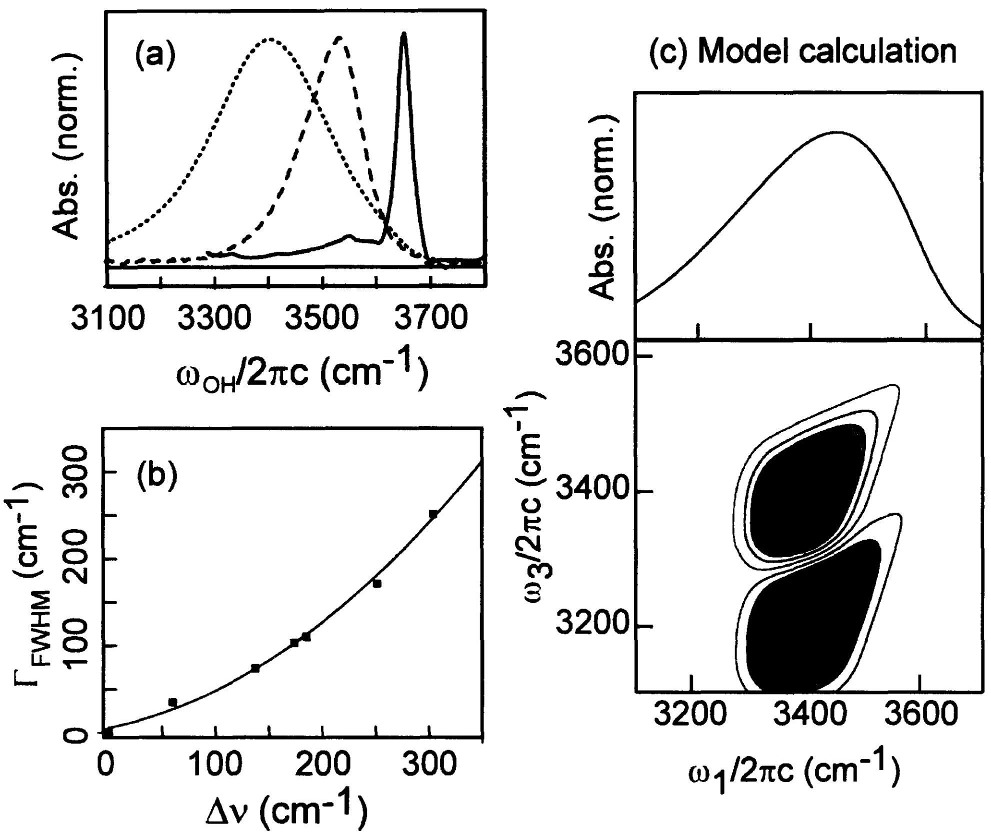

Figure 6.8. (Color) FTIR spectra of the OH stretch region of HOD in various solvents. Spectra were collected by mixing a 5% HOD in D_2O stock solution with the listed solvents to make a 2% HOD/D_2O in solvent solution. The solvents used in order of increasing $\Delta\nu$: parahydrogen matrix[59], chloroform-*d*, acetonitrile, diethyl ether, tetrahydrofuran, dimethyl-sulfoxide, and D_2O. Spectra were collected in a 100 μm pathlength CaF_2 sample cell. (a) Three representative spectra depicting the ω_{OH} region of HOD in $CDCl_3$ (solid line), THF (dashed line) and D_2O (dotted line). (b) A plot of the Γ_{FWHM} of the OH line shape as a function of the shift of the mean frequency from the gas phase value of 3710 cm^{-1}, $\Delta\nu = 3710 - \langle \omega_{OH} \rangle$. The FWHM was determined by fitting a half Gaussian through the high frequency half of the experimental line shape. This was done to minimize the effects of the low frequency wing resulting from the small population of HOD/D_2O dimers. The solid line is the quadratic fit: $\Gamma_{FWHM}[cm^{-1}] = 0.002\Delta\nu^2 + 1$. (c) Given these empirical observations, we can calculate a 2D line shape assuming a distribution of stable hydrogen bonding environments of varying strengths. The 1→ 2 anharmonicity is determined assuming Δ varies linearly with $\Delta\nu$. Given the gas[46] and liquid[49] phase anharmonicity of HOD we set $\Delta[cm^{-1}] = 0.3\Delta\nu + 157$.

The analysis of spectral relaxation indicates that molecules prepared on the blue side of the OH absorption line relax rapidly toward line center within 100 fs, whereas molecules prepared on the red equilibrate more slowly and show evidence of hydrogen bond oscillations. Since the red side of the line shape is associated with HOD molecules in which the proton is in a hydrogen bonded configuration (HB) while the blue side arises from protons that are in non-bonded or strained configurations (NHB), this observation is consistent with the description of hydrogen bond switching in water pictured in Figure 6.1c. Molecules exist only stably in a HB, although with large configurational fluctuations, whereas the NHB species are intrinsically unstable and return to the HB state within the time scale of water's fastest intermolecular motions.

6.3.3 Molecular dynamics simulation of 2D IR spectra

Multidimensional spectra calculated from simulated frequency trajectories are compared with the measured experimental data in Figure 6.2. Although they somewhat overestimate the inhomogeneity of the $\tau_2=0$ line shape, the computed 2D IR spectra capture the asymmetry of the experimental line shapes that indicates frequency dependent relaxation dynamics (see Figure 6.3b). Previously we showed how the slope of the node as a function of waiting time tracks the loss of frequency memory and follows the general behavior of the experiment.[39] As a measure of $C(\tau)$, the slope of the node extracted from MD simulations differs in the weighting of the beat and the slow decay component. Recent studies have highlighted the quantitative failings between MD simulations and ultrafast infrared experiments, and have attributed these failings to the form of the intermolecular water potential used.[60,61] However, the qualitative agreement between the experimental and theoretical 2D line shapes allows one to turn to the MD simulations to further explore the molecular origin of the observed spectral features.

Molecular dynamics simulations provide a direct route for interpreting 2D IR experiments in terms of microscopic dynamics of the hydrogen bonding network because ω_{OH} is simply a function of instantaneous atomic positions. To address the importance of hydrogen-bond dynamics and frequency evolution in the τ_1 and τ_3 time periods, we compare two-dimensional joint probability distributions $P(\omega_3,\tau_2|\omega_1)$ with the calculated 2D IR line shape $S'(\omega_1,\tau_2,\omega_3)$ in Figure 6.9. For comparison, the 2D IR line shape in this case are presented without contributions from the v=1→2 transitions. The joint probability P describes how molecules initiating from an environment with instantaneous frequency ω_1 evolve to ω_3 after waiting τ_2. In the limit that there is no frequency evolution during τ_1 and τ_3, P and S' should be equal. Casual examination of Figure 6.9, shows that the two are clearly different and highlight the importance of the inherent dynamical evolution present in the spectroscopy.

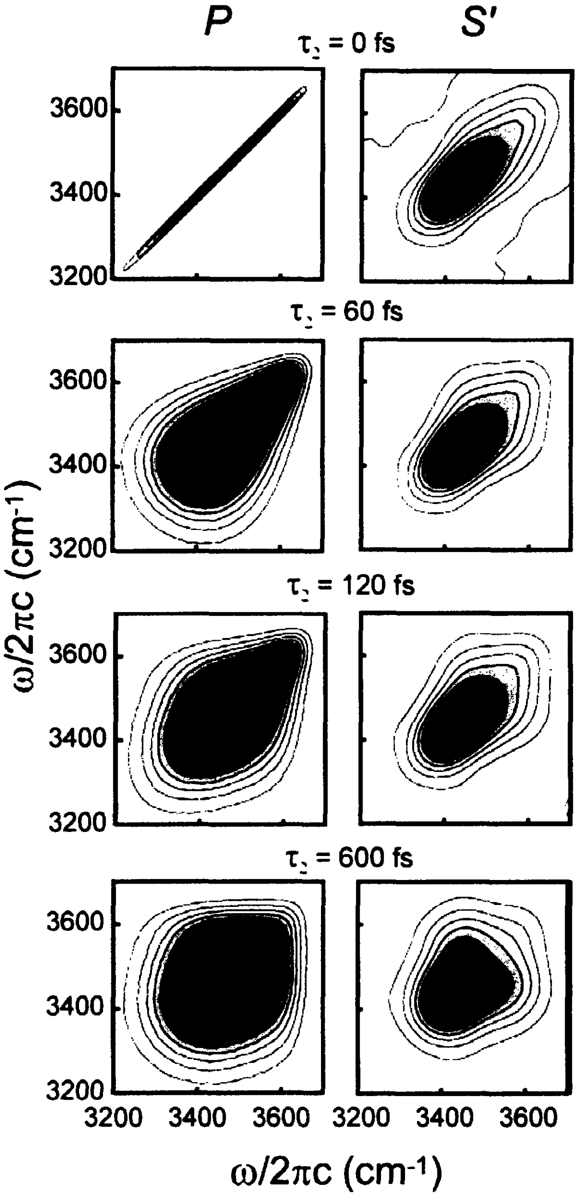

Figure 6.9. (Color) Joint probability frequency distributions, $P(\omega_3,\tau_2|\omega_1)$ (left) for the listed waiting times from the MD simulation. Absorptive 2D IR spectra, S_C',(right column) calculated for the same values of τ_2 without the $\nu = 1 \rightarrow 2$ contribution.

For $\tau_2=0$, the joint probability is naturally a diagonal line, reflecting the inhomogeneity of a system in which no frequency evolution has occurred. With increased waiting time, *P* broadens away from the diagonal, although with a frequency distribution that appears narrower on the blue side than the red. This is very different from the line shape *S'* and closely parallels the model calculation in Figure 6.8c. When characterized by the antidiagonal width, the distribution on the red side spreads out across the majority of the frequency distribution by τ_2 = 60 fs but then narrows again by τ_2 = 120 fs, the timescale of hydrogen bond stretching within the MD simulation. On the blue side of the distribution, the ensemble relaxes monotonically back to band center. The slower evolution of the blue side in *P* leads to a much higher amplitude than in *S'* and even an apparent separation of the distribution into two peaks at τ_2 = 60 fs. For waiting times beyond the intermolecular timescale ($\tau_2>$ 120 fs) the agreement between *P* and *S'* improves. Clearly, an interpretation of the spectroscopy of HOD in D_2O cannot be described purely within the language of joint probabilities. Instead, the 2D line shape characterizes an averaged frequency trajectory over the timescale of the fastest intermolecular motions plus the waiting time. Such averaging acts to narrow the redside of the line shape due to underdamped motion of the hydrogen bond, while the blue side is broader due to its monotonic relaxation toward band center.

Further verification of the proposed free energy surface in Figure 6.1c comes from analyzing the evolution of ω_{OH} during switching events. Trajectories were analyzed to identify when the HOD proton switched from hydrogen bonding with an initial acceptor oxygen to a new acceptor. As a working definition for the switching point,

τ_{switch}, we chose the bifurcated geometry in which the hydrogen of HOD was equidistant from two acceptor oxygen atoms, $r(\mathrm{H}\cdots\mathrm{O}_i)-r(\mathrm{H}\cdots\mathrm{O}_f) = 0$. From this definition, we observed HB switching at a rate of 2700/ns. This was used to calculate the average evolution of the OH frequency from the switching point $\langle\omega_{OH}(\tau-\tau_{switch})\rangle$. Figure 6.10a compares the frequency distribution molecules at the switching point with the total frequency distribution of molecules classified as NHB from the pair-wise geometric definition. The two distributions are indistinguishable, indicating that the instantaneous value of ω_{OH} is unable to differentiate between large fluctuations about HBs and molecules switching partners. We find that 35% of molecules that evolve into a NHB go on to switch hydrogen bonding partners. As can be seen from Figure 6.10b, $\langle\omega_{OH}\rangle$ begins at ~3590 cm^{-1} and rapidly relaxes to the equilibrium distribution in an 80 fs and 500 fs bimodal form: time constants associated with twice the librational period and the global structural rearrangement of the liquid. No 120 fs beat is observed since hydrogen bond vibration does not project favorably onto the switching coordinate. These observations further highlight the transient nature of molecules that visit the blue side of the line shape.

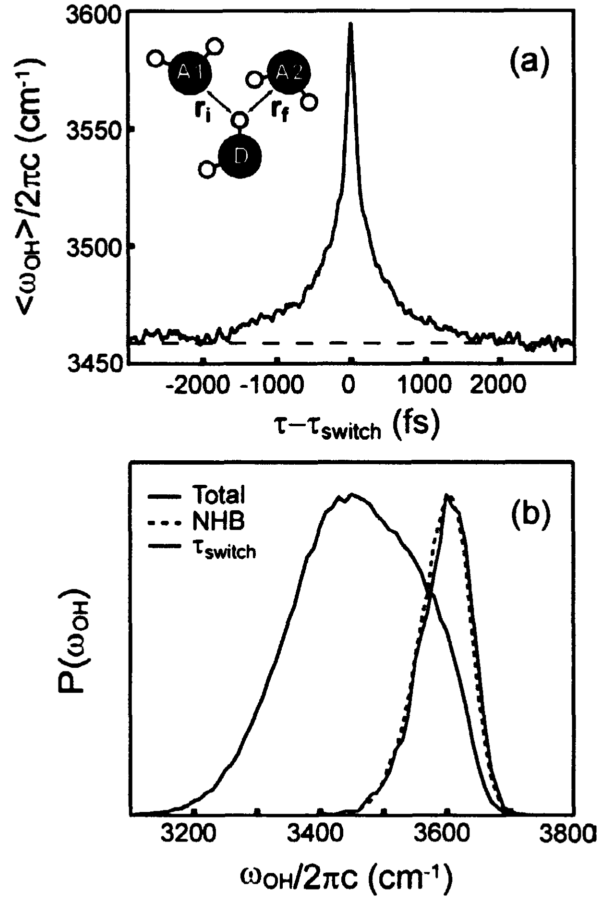

Figure 6.10. (Color) Frequency dynamics of the OH stretch during hydrogen bond switching. (a) Time dependence of $\langle \omega_{OH} \rangle$ around the switching transition state. The switching point was defined by the bifurcated geometry (r_i=r_f) and trajectories were averaged about that point in time. (b) Comparison of the total instantaneous frequency distribution, NHB distribution and those at the switching configuration.

6.4 Discussion

6.4.1 Comparison to related studies

The HOD:D_2O system has been widely studied in an effort to describe local hydrogen bonding fluctuations and rearrangements in water. Advances in ultrafast laser technology have allowed for increasingly detailed studies of the fastest events, with a variety of experimental methods. In general these experiments can be broken into two classes: IR transient hole burning (THB) with IR or Raman probing and broadband IR echo or 2D IR techniques. THB has the advantage of spectrally resolved excitation and detection, although at the expense of time-resolution. Echo experiments have the best time resolution, but integrate over spectral components. 2D IR experiments provide the best available combination of time and spectral resolution, in which the time-resolution for the evolution of different spectral components is set by the vibrational dephasing of the system.

While some of the differences in the results between these classes of experiments are a result of varying experimental parameters, both THB and echo experiments are in general agreement on a ~1 ps long timescale for spectral relaxation.[18,22,62,63] The shorter pulse durations used in echo experiments have also observed an additional fast ~100 fs component[8,64-67], which in some manner is accounted for by analyzing THB spectra by convolution with a homogeneous linewidth. However, other difficulties arise in comparing THB and echo experiments due to differences in how dynamical quantities are extracted from the spectroscopic observables. Echo experiments have traditionally relied on the second cumulant approximation to interpret experiments in terms of a two-point frequency correlation function. The frequency dependent results presented here, however, show that a two-point $C(\tau)$ is incapable of fully capturing the dynamics. The presence of heterogeneous dynamics does not mean that $C(\tau)$ is an inappropriate characterization of the system, but rather that it should be interpreted as a population weighted average of HB and NHB fluctuations and relaxation. As such, the weighting of various timescales of the extracted $C(\tau)$ will depend sensitively on the pulse bandwidth and center frequency of the excitation pulses.

THB experiments are closely related to the 2D IR spectra presented here in that they are capable of resolving frequency dependent dynamics. THB spectra acquired at a pump wavelength of ω_1 and pump-probe time delay τ_2 are analogous to slices through the 2D correlation spectrum at ω_1 for a waiting time τ_2, given that the chosen value of τ_2 accounts for the THB pulse duration τ_{pulse}, ($\tau_2 \approx T + \tau_{pulse}$). This difference emphasizes the importance of Fourier transform 2D IR methods in the present system, since the important dynamical heterogeneities are most clearly observed on time scales less that THB pulse lengths. Similarly, in the THB experiment one would need to select the correct pump frequency resolution a priori, a next to impossible feat given that the broadening of the 2D line shape varies with frequency.

Conclusions drawn from similar THB experiments have argued for various descriptions of the hydrogen bonding dynamics. The groups of Bakker and Gale have emphasized a continuous distribution of structures that spectrally relax through overdamped motion of the hydrogen bond.[62,63] Supporting a mixture picture, results from the groups of Laubereau and Dlott have interpreted their data in terms of distinct subbands underneath the broad OH line shape that interconvert on the picosecond timescale.[18,22,68] Laubereau and Dlott both suggest the presence of two prominent subbands corresponding to strongly hydrogen bonded species and weak or strained hydrogen bonds (i.e. HB and NHB). Our data supports the notion that HB and NHB are spectroscopically distinguishable (although not clearly), but observe the return of NHB to HB by a waiting time of 100 fs. Slices through the 2D surfaces presented here for waiting times of 300 fs (see Figure 6.4), however, are qualitatively similar to THB spectra in Figure 1 of Ref 68. Instead of providing evidence for long-lived NHBs that persist on the order of a picosecond or longer our results argue that the hetereogeneous distribution of local NHB environments rapidly disappears. For longer waiting times the distribution evolves as an ensemble of hydrogen bonded oscillators, although ω_1 slices through the 2D surface still appear qualitatively different due to the initial heterogeneous distribution. Such an interpretation might explain the negligible frequency dependent spectral relaxation observed by Bakker and Gale who have fit THB transients assuming a single correlation time.[62,63]

Recent 2D correlation spectra of the OD stretch of HOD in H_2O by Fayer and coworkers are qualitatively similar to our previously presented results and those shown here.[20] For the τ_2=100 surface, Steinel et al. observed a dynamic linewidth (ω_3 slice) that broadened with increasing ω_3.[21] This frequency dependence was found to have disappeared by a waiting time of 400 fs. The authors interpreted the frequency dependence in terms of faster fluctuations about a less constrained, weakly hydrogen bonded structure that vanishes by 400 fs because of an exchange of local environments. The physical picture implied by this statement is that various stable environments exist in water, which differ in the strength of hydrogen-bonding interactions and their fluctuations. (Here the term "fluctuation" refers to dynamical evolution within a local free energy minimum). While the τ_2=0 surface does reveal that HB and NHB environments experience qualitatively different dynamics, this interpretation does not account for the expected scaling of OH frequency and linewidth discussed above. Fluctuations about the NHB state are particularly fast, but these angular fluctuations lead to a narrower frequency distribution than for the HB state because ω_{OH} is sensitive to the projection of the electric field onto the OH bond vector. The observed broad distribution on the blue side of the 2D line shape for τ_2 = 100 fs results from the rapid reformation of hydrogen bonds and reflects the instability of the NHB state.

Another spectrally varying effect expected to influence the spectroscopy of HOD in D_2O is the non-Condon effect, which predicts that the OH transition dipole moment should increase with increased hydrogen bonding strength. Recent simulations by Skinner and coworkers have concluded that quantitative differences between homodyne and heterodyne echo experiments can also arise due to failings of the Condon approximation, which takes the transition dipole moment to be constant.[69] Our analysis and model calculations here make use of the Condon approximation. I present our experimental studies to quantify this effect in Chapter 7. However, the agreement between 2D IR surfaces from MD simulations calculated within the Condon approximation and our experimental data suggest that these effects will not qualitatively change our interpretation.

6.4.2 Conceptual pictures of hydrogen bonding in water

Analysis of 2D IR experiments shows that the vibrational dynamics of the OH stretching vibration of HOD in D_2O is consistent with the free energy surface proposed in Figure 6.1c. Our observations indicate that molecules prepared in HB or NHB configurations exhibit qualitatively different spectral relaxation processes. Those HB molecules excited on the red side of the line shape experience fluctuations in hydrogen bonding distances and angles, sampling the HB free-energy well, before participating in the activated kinetics of hydrogen bond switching observed on a picosecond time scale. Molecules excited on the blue are preferentially NHB species, which relax rapidly back to HB, either as a result of transient fluctuation into a strained geometry or because the molecule was excited at the transition state for hydrogen bond switching.

More than just a novel spectroscopic observation, the rapid return of NHB to HB has important implications for common structural pictures of liquid water. Couched in the language of reaction dynamics the exchange of hydrogen bonding partners is a concerted process where the NHB state exists either as a large fluctuation about a HB structure or as a fleeting state that appears during hydrogen bond switching. This study provides the most direct experimental verification of Stillinger's hypothesis that the rearrangement of liquid water involves a rapid switching of allegiances between hydrogen bonding partners.[3]

Our experimental results are not consistent with mixture-like pictures of water that propose two or more distinct hydrogen-bonding states separated by a barrier. These include any literal interpretation of HB and NHB configurations as stable states, or models that propose a distribution of stable hydrogen bonding configurations between two molecules. In such views the distinct hydrogen bonded species interconvert "slowly" as an activated process on the ~1 ps or longer timescale, which is inconsistent with the short NHB persistence time observed experimentally. Our observations also indicate that "dangling" hydrogen bonds, NHBs that are frustrated but entropically stabilized by the disorder of the liquid, are not significant species in the liquid. Dangling hydrogen bonds are the intermediate state in the step-wise view to hydrogen bond switching pictured in Figure 6.1b. In addition, these observations suggest that kinetic models for the ultrafast exchange of different hydrogen bonding configurations in the spectroscopy of HOD in D_2O[57] should be applied carefully. Kinetic models inherently assume an equilibrium between chemically distinct minima on a free energy surface, so that ultrafast exchange between species with no barrier separating them may provide a misleading molecular picture of the underlying dynamics.

A working definition of the hydrogen bond should serve as a good order parameter for hydrogen bond switching. Traditional definitions of the hydrogen bond involve an instantaneous evaluation of energetic or geometric criteria between two water molecules. Such criteria, along with the OH frequency, are unable to predict the fate of OH oscillators, a fact made clear by our previous quenching studies and Figure 6.10b.[39] Although taken for granted when one considers a covalent bond, the persistence of a state beyond the timescale of the fastest fluctuations is important when one considers the stability of hydrogen bonded configurations.

Such an observation led Eisenberg and Kauzmann to propose three different views of water's structure: instantaneous or *I* structure, *V* structure which averaged over fast intermolecular vibrations, and *D* structure which included net reorientation and diffusion as well.[1] Hirata and Rossky compared the *I* and *V* structures of water using computer simulations and found a sharpening of both the intermolecular bond length (O···O distance) and the angular distribution (O-H...O angle) when averaged over 200 fs as compared to the instantaneous distribution of hydrogen bonded configurations.[38] This resulted in a significant enhancement in the number of hydrogen bonds in the *V* structure of water. Instantaneous measures of structure can be misleading because a large but short lived fluctuation about the HB state is indistinguishable from a persistent broken hydrogen bond. Echoing the proposal of Eisenberg and Kauzmann, our work shows that a working definition of a hydrogen bond must consider not only geometric or energetic criteria but also the persistence of the bond for timescales greater than intermolecular vibrations. From this perspective our measurements show that the vast majority of non-hydrogen bonded configurations return to hydrogen bonds on the timescale of water's fastest intermolecular motions, suggesting that water's structure is more ordered than instantaneous measures suggest.

The fleeting nature of the NHB state allows us to conclude that the switching of hydrogen bonded partners is a largely concerted process. It is clear that at the very least the switching of hydrogen bonded partners must involve three molecules: a hydrogen bond donor, the initial acceptor, and the subsequent acceptor. Viewed from this local picture it is easy to imagine that the transition state is a bifurcated hydrogen bond, a symmetric species in which the donor proton is shared equally between the two acceptor oxygens. As inferred by the timescale of relaxation for NHB species, it is likely librations that move the proton along this reaction coordinate. MD simulations have suggested that angular fluctuations play an important role in hydrogen bond switching.[34,70] Our results are also consistent with the recent MD simulations by Laage and Hynes that concluded that molecular reorientation in water is accompanied by large angular jumps and correlated motion of the initial and final acceptor.[71]

Our conclusion that the hydrogen bond switching event is a concerted process also suggests a different perspective on defining the hydrogen bonded state from geometrical criteria in simulation. Since effective measures of hydrogen bonding in water will need to distinguish different stable species, we propose that the HB state and the switching event be characterized by an order parameter that characterize hydrogen bond bifurcation. For instance, an effective continuous variable is the difference in H···O distance between the two nearest water molecules to the proton, $r(\mathrm{H}\cdots\mathrm{O}_i)-r(\mathrm{H}\cdots\mathrm{O}_f)$.

6.5 Conclusions

We have presented an analysis of the frequency dependent relaxation of the OH stretching frequency observed in experimental 2D IR surfaces as a function of waiting time. In conjugation with MD simulations we have interpreted the observed heterogeneous dynamics in terms of the interconversion of different local hydrogen bonding environments. HB and NHB configurations experience qualitatively different spectral relaxation. NHB oscillators originating on the blue side of the OH line shape return to the HB state within 100 fs. The HB state was found to behave in a qualitatively different manner. The red side of the OH stretch 2D IR line shape is narrowed due to the underdamped motion of the hydrogen bond. A relatively slow relaxation, largely accomplished by a waiting time of 300 fs, accompanied equilibration within the free energy well of the HB state. Subsequent relaxation on the ~1 ps timescale was observed due to the switching of HB partners induced by the collective reorganization of the liquid.

Our observations also suggest that 2D IR spectroscopy can be used as a condensed phase transition state spectroscopy.[72] Direct experimental measures of chemical dynamics require the structurally sensitive observation of barrierless relaxation of an ensemble prepared at a transition state. The presence of barriers >kT in a non-equilibrium experiment obstruct the coherent evolution of an ensemble, and only provide kinetic data. Provided that a spectrally distinct signature of the transition state is available, 2D spectroscopy can be used to follow the relaxation of a system from the transition state to reactant and product channels. Here NHB configurations are observed as a fleeting excursion into a strained configuration or during the process of hydrogen bond switching from one acceptor molecule to another.

The experimental observations detailed here provide insight into the nature of hydrogen bonding structure and rearrangements in water. The results indicate that dangling hydrogen bonds or distributions of stabile environments with variable hydrogen-bonding strength or configuration are not appropriate models for water dynamics. We find that the transition state for switching will closely resemble the bifurcated hydrogen bond configuration. Thus hydrogen bonding in water should be effectively characterized by order parameters that interrogate this geometry, as opposed merely to geometric criteria that merely sample a pair of molecules. Ultimately hydrogen bonding in water cannot effectively be described in terms of instantaneous configurations between pairs of molecules. Such measures do not account for the chemical stability of the species, which is appropriately characterized through its persistence time relative to the intermolecular motions of the liquid.

Acknowledgements

I thank Sean Roberts for conducting the MD simulations described in this chapter.

References

[1] D. Eisenberg and W. Kauzmann, *The Structure and Properties of Water.* (Clarendon Press, Oxford, 1969).

[2] T. Head-Gordon and G. Hura, Chem. Rev. 102, 2651-70 (2002).

[3] F. H. Stillinger, Science 209 (4455), 451-57 (1980).

[4] R. Jimenez, G. R. Fleming, P. V. Kumar, and M. Maroncelli, Nature 369, 471-73 (1994).

[5] E. W. Castner, Jr., Y. J. Chang, Y. C. Chu, and G. E. Walrafen, J. Chem. Phys. 102, 653-59 (1995).

[6] I. Ohmine, J. Phys. Chem. 99, 6767 (1995).

[7] C. J. Fecko, J. D. Eaves, and A. Tokmakoff, J. Chem. Phys. 117 (3), 1139-54 (2002).

[8] C. J. Fecko, J. D. Eaves, J. J. Loparo, A. Tokmakoff, and P. L. Geissler, Science 301, 1698-702 (2003).

[9] J. J. Loparo, C. J. Fecko, J. D. Eaves, S. T. Roberts, and A. Tokmakoff, Phys. Rev. B 70, 180201 (2004).

[10] J. D. Smith, C. D. Cappa, K. R. Wilson, B. M. Messer, R. C. Cohen, and R. J. Saykally, Science 306, 851-53 (2004).

[11] S. A. Benson and E. D. Siebert, J. Am. Chem. Soc. 114, 4296-76 (1992).

[12] G. W. Robinson, C. H. Cho, and J. Urquidi, J. Chem. Phys. 111 (2), 698-702 (1999).

[13] R. J. Speedy, J. Phys. Chem. 88, 3364-73 (1984).

[14] E. H. Stanley and J. Teixeira, J. Chem. Phys. 73 (7), 3404-22 (1980).

[15] S. A. Rice and M. G. Sceats, J. Phys. Chem. 85, 1108-19 (1981).

[16] F. H. Stillinger, Adv. Chem. Phys. 31, 1-101 (1975).

[17] S. Woutersen, U. Emmerichs, and H. J. Bakker, Science 278, 658-60 (1997).

[18] R. Laenen, C. Rauscher, and A. Laubereau, Phys. Rev. Lett. 80, 2622-25 (1998).

[19] R. Laenen, C. Rauscher, and A. Laubereau, J. Phys. Chem. B 102, 9304-11 (1998).

[20] J. B. Asbury, T. Steinel, K. Kwak, S. A. Corcelli, C. P. Lawrence, J. L. Skinner, and M. D. Fayer, J. Chem. Phys. 121, 12431-46 (2004).

[21] T. Steinel, J. B. Asbury, S. A. Corcelli, C. P. Lawrence, J. L. Skinner, and M. D. Fayer, Chem. Phys. Lett. 386, 295-300 (2004).

[22] Z. Wang, A. Pakoulev, Y. Pang, and D. D. Dlott, J. Phys. Chem. A 108, 9054-63 (2004).

[23] C. P. Lawrence and J. L. Skinner, J. Chem. Phys. 118, 264-72 (2003).

[24] C. P. Lawrence and J. L. Skinner, Chem. Phys. Lett. 369, 472 (2003).

[25] P. Wernet, D. Nordlund, U. Bergmann, M. Cavalleri, M. Odelius, H. Ogasawara, L. Å. Näslund, T. K. Hirsch, L. Ojamäe, P. Glatzel, L. G. M. Pettersson, and A. Nilsson, Science 304, 995-99 (2004).

[26] G. E. Walrafen, M. S. Hokmabadi, and W.-H. Yang, J. Chem. Phys. 85, 6964 (1986).

[27] G. E. Walrafen, M. R. Fischer, M. S. Hokmabadi, and W.-H. Yang, J. Chem. Phys. 85, 6970 (1986).

[28] Y. Raichlin, A. Millo, and A. Katzir, Phys. Rev. Lett. 93, 185703 (2004).

[29] F. N. Keutsch and R. J. Saykally, PNAS 98, 10533-40 (2001).

[30] J. D. Smith, C. D. Cappa, K. R. Wilson, R. C. Cohen, P. L. Geissler, and R. J. Saykally, Proc. Nat'l. Acad. Sci, USA 102, 14171-74 (2005).

[31] H. Xu, H. A. Stern, and B. J. Berne, J. Phys. Chem. B 106, 2054-60 (2002).

[32] A. Luzar, J. Chem. Phys. 113 (23), 10663-75 (2000).

[33] A. Luzar and D. Chandler, Nature 379, 55-57 (1996).

[34] A. Luzar and D. Chandler, Phys. Rev. Lett. 76, 928 (1996).

[35] M. Cho, G. R. Fleming, S. Saito, I. Ohmine, and R. M. Stratt, J. Chem. Phys. 100, 6672-83 (1994).

[36] A. C. Belch and S. A. Rice, J. Chem. Phys. 86 (10), 5676-82 (1987).

[37] I. Ohmine, H. Tanaka, and P. G. Wolynes, J. Chem. Phys. 89 (9), 5852-60 (1988).

[38] F. Hirata and P. J. Rossky, J. Chem. Phys. 74, 6867-74 (1981).

[39] J. D. Eaves, J. J. Loparo, C. J. Fecko, S. T. Roberts, A. Tokmakoff, and P. L. Geissler, Proc. Natl. Acad. Sci. U. S. A. 102, 13019 (2005).

[40] G. C. Pimentel and A. L. McClellan, *The Hydrogen Bond.* (Freeman, San Francisco, 1960).

[41] C. M. Huggins and G. C. Pimentel, Spectral Properties of Hydrogen Bonding Systems, 1615-19 (1956).

[42] E. T. J. Nibbering and T. Elsaesser, Chem. Rev. 104, 1887-914 (2004).

[43] J. D. Eaves, A. Tokmakoff, and P. Geissler, J. Phys. Chem. A 109, 9424-36 (2005).

[44] J. D. Eaves, PhD, Massachusetts Institute of Technology, 2004.

[45] M. P. Allen and D. J. Tildesley, *Computer Simulation of Liquids*. (Oxford University Press, New York, 1989).

[46] J. R. Reimers and R. O. Watts, Mol. Phys. 52 (2), 357-81 (1984).

[47] S. Mukamel, *Principles of Nonlinear Optical Spectroscopy*. (Oxford University Press, New York, 1995).

[48] A. Piryatinski and J. L. Skinner, J. Phys. Chem. B. 106, 8055-63 (2002).

[49] J. J. Loparo, S. T. Roberts, and A. Tokmakoff, J. Chem. Phys. 125, 194521 (2006).

[50] A. Tokmakoff, J. Phys. Chem. A 104 (18), 4247-55 (2000).

[51] P. Mukherjee, I. Kass, I. Arkin, and M. T. Zanni, Proc. Natl. Acad. Sci. USA 103, 3528-33 (2006).

[52] J. D. Hybl, A. A. Ferro, and D. M. Jonas, J. Chem. Phys. 115, 6606-22 (2001).

[53] S. T. Roberts, J. J. Loparo, and A. Tokmakoff, J. Chem. Phys. 125, 084502 (2006).

54 T. Hayashi, T. l. C. Jansen, W. Zhuang, and S. Mukamel, J. Phys. Chem. A 109 (1), 64-82 (2005).

55 S. A. Corcelli, C. P. Lawrence, and J. L. Skinner, J. Chem. Phys. 120, 8107 (2004).

56 K. B. Moller, R. Rey, and J. T. Hynes, J. Phys. Chem. A 108, 1275-89 (2004).

57 T. l. C. Jansen, T. Hayashi, W. Zhuang, and S. Mukamel, J. Chem. Phys. 123, 114504 (2005).

58 D. E. Hare and C. M. Sorensen, J. Chem. Phys. 93 (10), 6954-61 (1990).

59 M. E. Farjardo, S. Tam, and M. E. DeRose, J. Mol. Struct. 695, 111 (2004).

60 S. A. Corcelli, C. P. Lawrence, J. B. Asbury, T. Steinel, M. D. Fayer, and J. Skinner, J. Chem. Phys. 121, 8897-900 (2004).

61 E. Harder, J. D. Eaves, A. Tokmakoff, and B. J. Berne, Proc. Nat. Acad. Sci. 102, 11611 (2005).

62 S. Woutersen and H. J. Bakker, Phys. Rev. Lett. 83, 2077-81 (1999).

63 G. M. Gale, G. Gallot, F. Hache, N. Lascoux, S. Bratos, and J.-C. Leicknam, Phys. Rev. Lett., 1068 (1999).

64 J. Stenger, D. Madsen, P. Hamm, E. T. J. Nibbering, and T. Elsaesser, Phys. Rev. Lett. 87 (2), 027401 (2001).

65 J. Stenger, D. Madsen, P. Hamm, E. T. J. Nibbering, and T. Elsaesser, J. Phys. Chem. A 106 (10), 2341-50 (2002).

66 S. Yeremenko, M. S. Pshenichnikov, and D. A. Wiersma, Chem. Phys. Lett. 369, 107-13 (2003).

[67] J. B. Asbury, T. Steinel, C. Stromberg, S. A. Corcelli, C. P. Lawrence, J. L. Skinner, and M. D. Fayer, J. Phys. Chem. A 108, 1107-19 (2004).

[68] R. Laenen, K. Simeonidis, and A. Laubereau, Bull. Che, Soc. Jpn. 75, 925-32 (2002).

[69] J. R. Schmidt, S. A. Corcelli, and J. L. Skinner, J. Chem. Phys. 123, 044513 (2005).

[70] F. S. Csajka and D. Chandler, J. Chem. Phys. 109, 1125-33 (1998).

[71] D. Laage and J. T. Hynes, Science 311, 832-35 (2006).

[72] D. M. Neumark, Acc. Chem. Res. 26 (2), 33-39 (1993).

Chapter 7

Variation of transition dipole strength across the OH stretching band of water

7.1 Introduction

Although well studied, water is still able to inspire lively debate. The recent challenge to the long established view that liquid water is locally tetrahedral is just one example.[1,2] Water remains controversial because of its complexity. In order to understand the structural dynamics of water's hydrogen bonding network one needs not only a structurally sensitive technique, but one that is able to resolve dynamics on the timescale of water's extremely fast intermolecular motions (i.e. tens of femtoseconds). Previous chapters have described how ultrafast infrared experiments of the OH stretching vibration are quite powerful in this regard because the OH stretching frequency, ω_{OH}, is related to the local hydrogen bonding structure. Therefore, time dependent changes in this frequency can be related to hydrogen bond dynamics. Chapters 4, 5, and 6 describe techniques that have been used to quantify vibrational relaxation, molecular reorientation, spectral diffusion and hydrogen bond rearrangement.

Ultrafast IR experiments have generally probed isotopic mixtures, such as the OH stretch of HOD in D_2O. In this way, one observes a local vibration, as compared to pure water where a delocalized excitonic state results from the close proximity of near degenerate oscillators.[3] Years of empirical observations have established how the OH stretching line shape changes with hydrogen bonding. Upon forming a hydrogen bond the mean frequency red shifts from the gas phase value, the line shape broadens and the integrated intensity increases.[4-6] In recent years there has been a large theoretical effort geared towards quantitatively understanding the origins of these effects.[7-9] Studies have found that ω_{OH} is correlated with the electric field projected onto the OH bond vector.[10] While the electric field is the result of all the water molecules in solution, the contribution of the hydrogen bond acceptor dominates. This means that ω_{OH} is largely determined by the geometric configuration of the hydrogen bonded pair. From such a perspective, it is easy to understand how hydrogen bonding affects the OH stretching coordinate. The electrostatic interaction of the hydrogen bond weakens the OH force constant shifting ω_{OH} to lower frequencies, broadens the distribution of electric field strengths felt by the proton and increases the magnitude of the transition dipole.

While the change in ω_{OH} with hydrogen bonding is exploited in ultrafast IR measurements in order to track changes in the hydrogen bonding environment, the change in transition dipole strength has largely been ignored. Ultrafast IR experiments are generally interpreted in terms of the traditional response function formalism of nonlinear spectroscopy which makes the Condon approximation.[11] Within the context of condensed phase vibrational spectroscopy, the Condon approximation assumes that the OH transition dipole is independent of the solvent degrees of freedom. Such approximations seem to be inappropriate given the increase in the integrated intensity of OH spectral line shapes as hydrogen bonding strength increases. Recent work by Skinner and coworkers have explored this non-Condon effect from a theoretical perspective.[12,13] Using a combined electronic structure/molecular dynamics approach they calculated how the OH transition dipole varied across the line shape and how it influences the spectroscopy as compared to the Condon limit. Such a variation in dipole becomes even more significant for nonlinear measurements where the measured signal is related to higher powers of the transition dipole. Skinner and coworkers concluded that differences in homodyne echo peak shift measurements and heterodyne detected 2D IR measurements for HOD/D_2O and DOH/H_2O, could be explained by how each experiment scales with the transition dipole when one allows for the magnitude of the dipole to vary with hydrogen bonding and hence ω_{OH}.[13]

A quantitative understanding of the OH spectroscopy of water requires knowledge of how different hydrogen bonded species are weighted in spectral observables. In this chapter, I experimentally quantify the variation of the transition dipole of the OH stretch of HOD in D_2O as a function of ω_{OH} through the examination of IR and Raman line shapes. IR and Raman line shapes arise from qualitatively different coupling mechanisms of the electric field to vibrational states, with the Raman polarizability being largely independent of hydrogen bonding strength.[12] Therefore, a comparison of IR and Raman spectra provides an intuitive way to quantify the non-Condon effect.[14] Previous studies have explored changes in the hydride stretching vibration upon altering the hydrogen bonding strength through changes in the solvent.[15-17] We exploit the shift in the density of states of the OH stretching vibration toward higher frequencies that occurs upon increasing the temperature of HOD in D_2O. Temperature dependent changes in the density of states are captured in the Raman spectrum, while the IR spectrum is additionally weighted by the non-Condon effect. Furthermore, we measure the temperature dependence of IR homodyne echoes in order to quantify the higher order dependence of the signal on the transition dipole and to understand how the non-Condon effect appears in higher order spectroscopies.

To extract the frequency dependent transition dipole from the temperature dependent data, we construct a spectroscopic model that accounts for the non-Condon effect. Motivated by our experimental results and the recent theoretical efforts of Skinner and coworkers, we use three frequency dependent transition dipoles as an input to our model to compare to the data. Two cases of spectral diffusion are examined, the inhomogeneous and homogeneous limits, which describe static and instantaneous relaxation, respectively. The static limit best reproduces trends observed in the experimental data. From these calculations we are able to draw conclusions on the variation of the transition dipole across the OH line shape. MD simulations of the OH spectroscopy are then used to examine the influence of more realistic spectral relaxation.

The chapter is organized as follows: In section 7.2 I detail the experimental acquisition of temperature dependent FTIR spectra and homodyne echoes of the OH Stretch of HOD in D_2O. This section also describes the methodology we employ to account for the non-Condon effect in our molecular dynamics simulations of the OH stretch. Section 7.3 presents how linear and nonlinear spectral observables change with temperature. Section 7.4 describes our modeling of the non-Condon effect to extract the variation of the transition dipole across the lineshape. MD simulations including non-

Condon effects are described in 7.5. We conclude in 7.6 by exploring how the variation of the transition dipole affects the interpretation of nonlinear experiments on water.

7.2 Experiment and methods

FTIR spectra were collected on a Thermo Electron spectrometer at 2 cm^{-1} resolution with a home-built temperature controlled sample cell. The sample was held between 1 mm thick CaF_2 windows with a 50 μm teflon spacer. The spectra were collected sequentially during a temperature ramp every ~25.5 s (~0.55 °C) and averaged over 16 scans (22 s, ~0.47 °C). A ~2% HOD in D_2O sample and D_2O background were measured in separate temperature ramps. The background spectrum was subtracted from the sample spectrum if the collection temperatures of each were within 0.2 °C. The final temperatures reported are an average of the sample and background temperatures and are spaced by ~0.5 °C from 20 to 80°C. Depolarized Raman spectra of HOD in D_2O were kindly provided by Saykally and coworkers and were originally published in Ref. 20.

Temperature dependent homodyne echoes were also collected. In this experiment three 45 fs mid-IR pulses impinge on the sample in a boxcar geometry. The phase matching of the excitation beams results in the third order signal being emitted from the missing corner of the box. The signal is integrated on a single channel InSb detector (IR Systems). One of the excitation beams is chopped at 500 Hz to allow for lockin detection of the detector signal. The echo field was collected as a function of the delay between the first two pulses, τ_1, with the delay between the second and third excitation pulses, τ_2, set to zero.

The mid-IR pulses were generated as described previously in Chapter 3. In brief, the output of a Ti:sapphire multipass amplifier (Femtolasers; 30 fs, 1 kHz, 800 nm) was used to pump a home built, two-stage BBO/$KNbO_3$ optical parametric amplifier (OPA) that gave 5 μJ pulse energies in the 3 μm wavelength range. Second harmonic autocorrelation measurements were used to set the timings between the excitation pulses and indicated the pulse was ~45 fs in duration. Spectra of the excitation pulses showed that the pulses were centered at ~3400 cm^{-1}, the maximum of the OH stretching fundamental, and had ~400 cm^{-1} of bandwidth (FWHM).

For the echo measurements, the HOD in D_2O sample was flowed as a 50 μm jet so as to avoid the generation of any nonresonant signal from sample cell windows. Previous measurements have indicated that the resonant OH signal collected from a sample cell can be significantly corrupted at early τ_2 delays by this undesirable window response. The concentration of the sample was approximately 2% H_2O in D_2O resulting in a peak optical density of the OH stretch of ~0.4. The OPA and experimental area was purged with dry air so as to avoid any atmospheric water absorption and to prevent any further exchange of protons in the jet that would result in a change in OH concentration.

Molecular dynamics (MD) simulations employing the commonly used SPC/E water potential were carried out as described in detail elsewhere.[18] Each computed trajectory consisted of a single HOD molecule surrounded by a bath 107 D_2O molecules. Periodic boundary conditions were employed as well as periodic velocity rescaling to maintain the temperature near 298 K. Although the simulation is completely classical, we include a single quantum mechanical degree of freedom, the OH stretching frequency, by making an adiabatic separation between this fast coordinate and the slower translations and rotations of the surrounding bath molecules. We describe the OH stretch by using the gas phase potential of Reimers and Watts.[19] At every time step, the bath molecules are frozen and the potential energy along the OH stretching coordinate is calculated. The OH frequency is then solved for via second order perturbation theory.

With a frequency trajectory in hand, it becomes possible to calculate any linear or nonlinear infrared spectroscopic observable. The third order polarization giving arise to the 2D IR lineshape is described by a convolution of the third order nonlinear response function and the exciting electric fields:

$$P^{(NL)}(t)=\int_0^t d\tau_3\int_0^{\tau_1} d\tau_2\int_0^{\tau_2} d\tau_1 R^{(3)}(\tau_1,\tau_2,\tau_3)E(t-\tau_3)E(t-\tau_3-\tau_2)E(t-\tau_3-\tau_2-\tau_1) \quad (1)$$

In the limit where the exciting fields are delta functions in time, the polarization becomes equal to the nonlinear response itself. This function consists of a sum of eight terms, each term corresponding to a signal measured in a different phase matching direction dictated by the wave vectors of the input pulses. The 2D lineshape is constructed from the Fourier transform of the sum of the rephasing and nonrephasing signals measured in the $\mathbf{k}_s = -\mathbf{k}_1 + \mathbf{k}_2 + \mathbf{k}_3$ and $\mathbf{k}_s = +\mathbf{k}_1 - \mathbf{k}_2 + \mathbf{k}_3$ phase matching directions respectively. Within the semiclassical approximation to the response, for a single vibrational resonance we can write these signals as:

$$\begin{aligned}R_R^{(3)}(t_1,t_2,t_3)=2\Big\langle &\mu_{10}(t_1+t_2+t_3)\mu_{10}(t_1+t_2)\mu_{10}(t_1)\mu_{10}(0)\exp\Big[i\int_0^{t_1}\omega_{10}(\tau)d\tau-i\int_{t_1+t_2}^{t_1+t_2+t_3}\omega_{10}(\tau')d\tau'\Big]\Big\rangle\\ -\Big\langle &\mu_{21}(t_1+t_2+t_3)\mu_{21}(t_1+t_2)\mu_{10}(t_1)\mu_{10}(0)\exp\Big[i\int_0^{t_1}\omega_{10}(\tau)d\tau-i\int_{t_1+t_2}^{t_1+t_2+t_3}\omega_{21}(\tau')d\tau'\Big]\Big\rangle\end{aligned}$$

(2)

Here, $\mu_{10}(t)$, $\mu_{21}(t)$, $\omega_{10}(t)$, and $\omega_{21}(t)$ are the time dependent transition dipoles and frequencies of the 1 ← 0 and 2 ← 1 vibrational transitions.

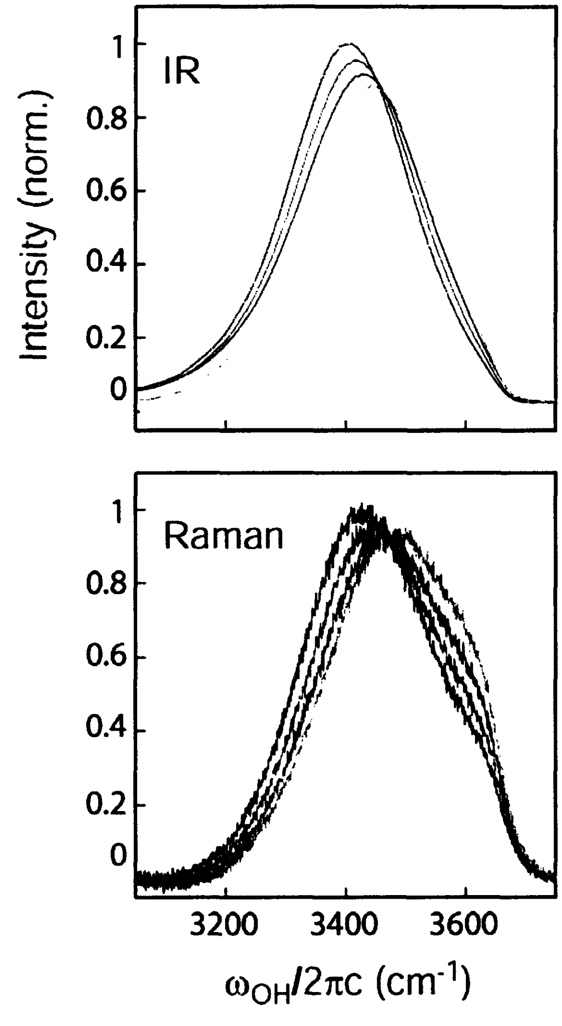

Figure 7.1. (Color) Temperature dependent IR (top panel) and Raman[20] (bottom panel) spectra for the OH stretching region of HOD in D_2O. The spectra displayed were collected at 20, 40, 60 and 80° C.

7.3 Temperature dependent IR spectra and homodyne echoes

A comparison of the temperature dependence of IR and Raman spectra of the OH stretch of HOD in D_2O can be found in Figure 7.1. Qualitative differences exist between the IR and Raman spectra. The IR spectrum is red shifted by ~50 cm^{-1} from the peak of the Raman line shape and while asymmetric, lacks the prominent shoulder at 3600 cm^{-1} of the Raman transition. Both, however span a range of frequencies consistent with a large sampling of hydrogen bonding strengths. The line shapes tail off at high frequencies at 3700 cm^{-1}, which is approximately equal to the gas phase frequency of 3707 cm^{-1}. On the red side, the line shapes extend to 3150 cm^{-1}, which is well beyond the mean frequency of ice at 3300 cm^{-1}.

As is well known, the linear absorbance is proportional to:

$$A \propto \mu^2 N \tag{3}$$

where μ is the transition dipole and N is the number density of resonant oscillators. Raising the temperature of water from 20° to 80° C results in ~2% change in the density. We correct for this temperature dependent change in concentration by multiplying the spectra by a density correction factor. As the temperature is increased, the peaks of both the IR and Raman line shapes shift to the blue, the line widths increase and the line shapes become more asymmetric. This asymmetry is especially visible in the Raman line shape where the shoulder at 3600 cm^{-1} becomes substantially more pronounced. The integrated area of the IR line shape decreases by ~10% over the measured temperature range while the area of the Raman line shape is largely unchanged within the signal to noise. Figure 7.2 quantifies the change in the peak intensity (ε), frequency of the maximum or peak position (ω*), and the line width defined as the FWHM (Γ) for the IR line shape.

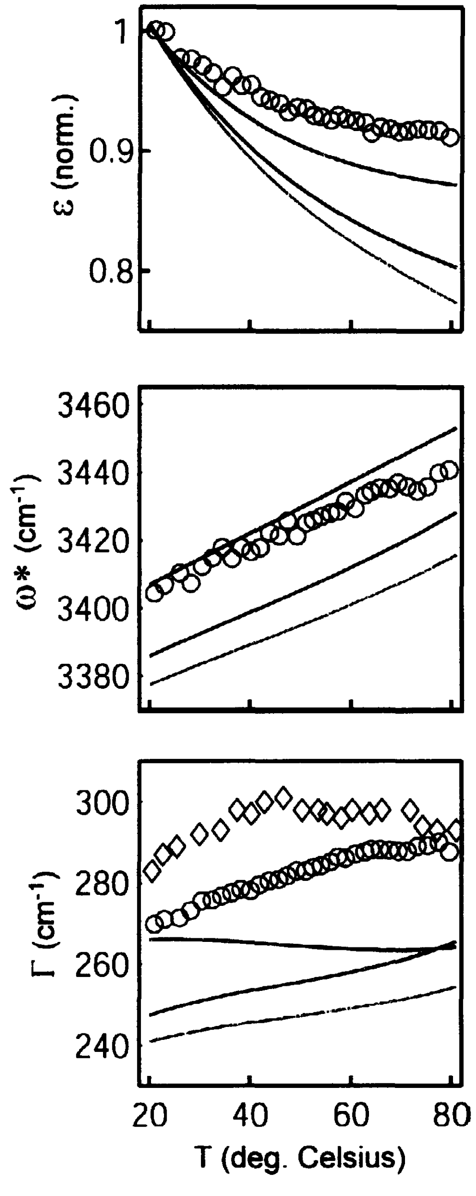

Figure 7.2. (Color) Temperature dependence of peak intensity (ε), frequency of the maximum or peak position (ω*), and the line width defined as the FWHM (Γ) OH IR line shapes. The solid lines represent results of calculations of the temperature dependent IR line shape within the static limit for (blue), μ_{SK} (red), and μ_{SK2} (green) while the open circles are the experimental IR values. Open diamonds in the plot of Γ are the data points of the Raman spectra.

Temperature dependent homodyne measurements are sensitive to the eighth power of the transition dipole:

$$I_{echo} \propto \mu^8 N^2 I_{pump}^3 \qquad (4)$$

where I_{echo} is the intensity of the homodyne echo and I_{pump} is the intensity of the excitation pump beams. Given their higher order dependence on the transition dipole, homodyne echoes are particularly sensitive to non-Condon effects and therefore best illustrate how these effects can influence nonlinear spectroscopy. Representative homodyne echo traces can be found in Figure 7.3. We correct for the effective change in concentration that occurs upon heating by multiplying by a correction factor that goes as the concentration squared. I_{echo} was found to scale as N^2 in the concentration range employed in this study. This scaling breaks down at high concentrations due to the propagation effects resulting in the reabsorption of the signal. As noted previously the echoes are non-Gaussian.[18] This asymmetry does not change with temperature and the peak of the echo maximum remains the same within the signal to noise. Most evident is the dramatic decrease in intensity with increasing temperature. The integrated area as a function of temperature can be found in Figure 7.4. This area decreases by ~40% over a temperature range of 20-70 ° C.

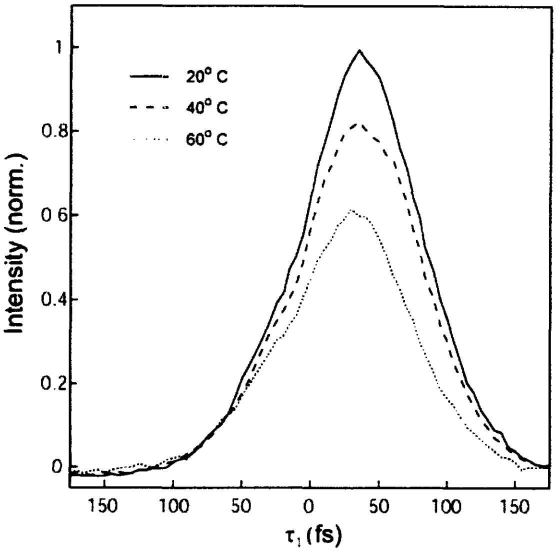

Figure 7.3. Homodyne echo traces for temperature values of 20, 40 and 60° C. Increasing temperature is correlated with a decrease in the maximum intensity.

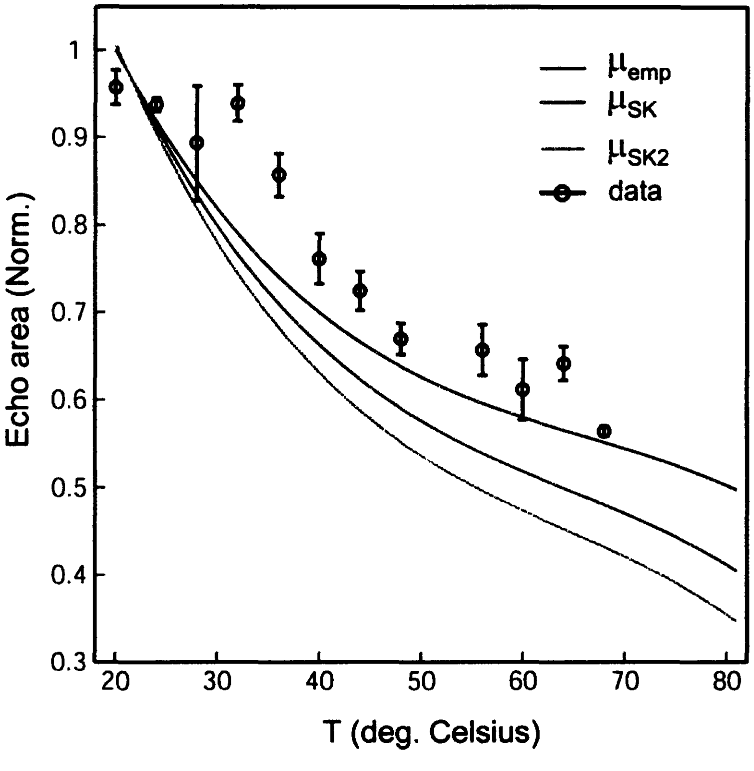

Figure 7.4. (Color) Decrease in homodyne echo area as a function of temperature. Solid lines refer to calculations within the static limit.

7.4 Modeling of the non-Condon effect

7.4.1 Calculation of linear IR spectra

Modeling of the non-Condon effect in infrared spectra is necessary to quantify the variation of the OH transition dipole as a function of ω_{OH}. The absorption of IR radiation requires a change in the permanent dipole of the molecule as it moves along the vibrational coordinate. For the IR line shape it is common to expand the dipole operator in the OH coordinate around its equilibrium position in the liquid:

$$\tilde{\mu}=\tilde{\mu}(q_o)+\left.\frac{\partial\tilde{\mu}}{\partial q}\right|_{q=q_o} q+\left.\frac{\partial^2\tilde{\mu}}{\partial q\partial Q}\right|_{q=q_o,Q=Q_o} qQ+\ldots \qquad (5)$$

where q is the intramolecular OH coordinate and Q refers to the bath coordinates. The transition dipole moment is given by $\mu_1=\frac{\partial\tilde{\mu}}{\partial q}$. The term $\mu_2=\frac{\partial^2\tilde{\mu}}{\partial q\partial Q}$ is the leading term that makes the transition dipole moment dependent on the bath coordinates, and will be referred to as the non-Condon parameter. For the OH stretch of HOD, Q, it is now well established that the dominant interaction of the OH coordinate with the intermolecular degrees of freedom is expressed through the electric field E that the surroundings exert on q.[10,21,22] Therefore, we equate $Q\sim E$. Furthermore, calculations have shown that a linear correlation exists between ω_{OH} and E, so that $\frac{\partial}{\partial\omega}\left[\frac{\partial\mu}{\partial q}\right]\propto\frac{\partial^2\mu}{\partial q\partial Q}$.[10,21,22] For this reason, if higher order terms are negligible, the transition dipole is expected to vary linearly with frequency:

(6)

where ω_g is the gas phase frequency.

In this study we make use of the difference in transition dipole variation between the IR and Raman lineshapes. The IR absorption and Raman scattering line shapes are commonly expressed as the Fourier transform of a correlation function in the dipole operator μ and polarizability operator α respectively. In the limit that population relaxation and orientational relaxation negligibly influence the line shape, the line shape is dictated by the correlated fluctuations of the transition moment matrix elements with the $v = 0 \rightarrow 1$ energy gap[11]:

$$\begin{aligned}\sigma_{IR}(\omega) &= \int_{-\infty}^{+\infty} dt\, e^{i\omega t} \left\langle \mu_{10}(t)\mu_{10}(0) e^{-i\int dt\, \omega_{10} t} \right\rangle \\ \sigma_{R}(\omega) &= \int_{-\infty}^{+\infty} dt\, e^{i\omega t} \left\langle \alpha_{10}(t)\alpha_{10}(0) e^{-i\int dt\, \omega_{10} t} \right\rangle\end{aligned} \tag{7}$$

These expressions indicate that transition dipole variation will have the most pronounced effects for inhomogeneous systems, where it is not averaged out by motional narrowing. For that reason we begin to analyze the non-Condon effect on the vibrational spectroscopy of water in the static limit, in which these expressions can be written by the common Golden Rule expression for spectral line shapes.

$$\begin{aligned}\sigma'_{\mathrm{IR}}(\omega) &= \int d\omega_i \rho(\omega_i) \left|\mu_{10}(\omega_i)\right|^2 \delta(\omega - \omega_i) \\ \sigma'_{\mathrm{R}}(\omega) &= \int d\omega_i \rho(\omega_i) \left|\alpha_{10}(\omega_i)\right|^2 \delta(\omega - \omega_i)\end{aligned} \tag{8}$$

Here $\rho(\omega)$ is the density of states and the dash refers to the inhomogeneous limit.

Experiments and theory suggest that the polarizability is largely independent of hydrogen bonding.[14] It has been observed that the integrated area of the OH line shape changes by only a factor of 1.7 going from the gas to the liquid. This is compared to a factor of ~20 for the IR line shape.[23] Furthermore, the integrated area of the Raman line shape shows little change over the temperature range investigated here. Recent calculations by Corcelli et al. showed that the polarizability was nearly unchanged for the electric field strengths generated by configurations of liquid water.[12] As an approximation we therefore assume that the Raman line shape best reflects the OH density of states. Other factors could result in the Raman line shape deviating from the density of states including coupling to lower frequency modes, overlapping overtone bands and spectral narrowing due to frequency relaxation processes and reorientational dynamics, but we ignore these effects in the following discussion. These processes will act to reduce the magnitude of the observed non-Condon effect.

Within these approximations, when the transition dipole is independent of frequency, the IR and Raman line shapes are directly proportional. Frequency dependence of μ can cause the line shape to deviate significantly from $\rho(\omega)$. This is illustrated in a model calculation in Figure 7.5. The increase in $\mu(\omega)$ with hydrogen bonding results in the red shift of $\sigma'_{IR}(\omega)$ and the suppression of the shoulder on the high frequency side of the line shape.

The non-Condon effect is the most significant in the inhomogeneous limit. Allowing the frequencies of OH oscillators to evolve averages the magnitude of $\mu(\omega)$ over the timescale of the free induction decay. The opposite extreme of a static frequency distribution is the homogeneous limit where it is assumed that spectral diffusion is instantaneous. In this limit the entire spectrum is proportional to the transition dipole squared evaluated at the mean frequency of the density of states:

$$. \tag{9}$$

Figure 7.5 shows calculated spectra in the homogeneous limit for three different temperatures. Within these approximations the σ''_{IR} line shape is identical to the Raman spectrum. The temperature dependent σ''_{IR} line shapes deviate slightly from the Raman spectra in their intensity because they are weighted by the average transition dipole. Given the inability of the homogeneous limit to reproduce the clear differences between the IR and Raman spectra we will not consider it further.

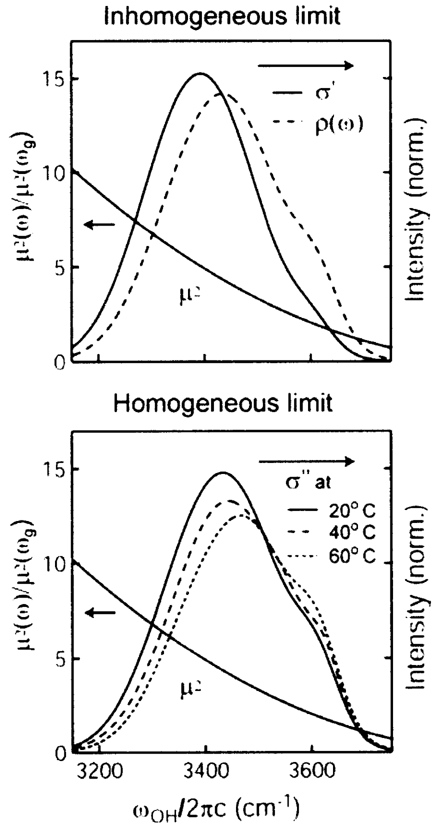

Figure 7.5. IR line shapes calculated in the inhomogeneous (top) and homogeneous (bottom) limits.

7.4.2 Calculation of IR homodyne echoes

We can extend the inhomogeneous model to calculate the homodyne echo signal. The general expression for the third order polarization is given in equation (1) and involves a response function convolved with the three excitation fields. The response function is a summation over the well-known Feynman diagrams of a three level system.[18,24] These diagrams describe the states that can be prepared given the phase matching and pulse ordering of the excitation beams. In general, the diagrams can be divided into two groups: rephasing or echo-like processes and nonrephasing processes, which resemble a free induction decay. Given the broad bandwidth of the excitation fields, $R(t_3,t_2,t_1)$ includes contributions from the 0→1 and 1→ 2 transitions. For simplicity we will assume that the 1→2 density of states is identical to 0→1 distribution but shifted by an anharmonicity, Δ, of 250 cm^{-1} and that the 1→2 transition dipole strength is scaled harmonically:

$$\begin{aligned}\rho_{1\to 2}(\omega) &= \rho(\omega-\Delta)\\ \mu_{1\to 2}(\omega) &= \sqrt{2}\,\mu(\omega-\Delta) \qquad (10)\end{aligned}$$

In addition, the contribution from nonrephasing processes will be ignored as the rephasing signal dominates in the static limit. With only rephasing signals to consider we can neglect the mixing of diagrams that occurs when the finite excitation pulses overlap in time. This allows for the application of the convolution theorem to write the frequency domain expression for the polarization as a product of the excitation beams with the response function. The excitation beams act to spectrally filter the molecular response.

Under these assumptions and after integrating over the static distribution of frequencies we can write the frequency domain expression of the polarization as:

$$P^{(3)}(\Omega_1,\Omega_3) = E(\Omega_1)^2 E(\Omega_3) \int d\omega_i \Big[2\rho^2(\omega_i)\mu^4(\omega_i)\delta(\Omega_1+\omega_i)\delta(\Omega_3-\omega_i) \\ + \rho^2(\omega_i)\mu^2(\omega_i)\delta(\Omega_1+\omega_i)\delta(\Omega_3-\omega)\cdot 2\rho^2_{1\to2}(\omega)\mu^2_{1\to2}(\omega)\delta(\Omega_1+\omega_i)\delta(\Omega_3-\omega_i+\Delta) \Big] \tag{11}$$

where Ω_1 and Ω_3 refer to the Fourier transforms of the time variables t_1 and t_3 and $E(\Omega)$ is the spectrum of the excitation pulses.[25] The homodyne echo measures the intensity of the polarization:

$$I_{echo} = \left| \int\int P^{(3)} d\Omega_1 d\Omega_3 \right|^2 \tag{12}$$

Application of the equations 10-12 allows for a prediction as to how the integrated area of the echo signal should change with temperature.

7.5 Temperature dependence of the spectroscopic model

In order to quantify $\mu(\omega)$, we compare our experimental temperature dependence of the OH line shape and echo with calculations using our static spectroscopic model using three cases of the transition dipole as inputs. The choices of transition dipoles are motivated by our experiments and recent theoretical work. Each transition dipole is normalized to its value at the experimental gas phase frequency of 3707 cm^{-1} and plotted in Figure 7.6 along with μ_2 in the bottom panel.

In the first case, we consider the frequency dependent transition dipole empirically determined from the ratio of the IR and Raman line shapes. The expression for suggests that one is able to invert the IR and Raman data to obtain $\mu(\omega)$ without making any approximations in how μ varies with frequency:

$$\left|\mu_{emp}(\omega)\right| \propto \sqrt{\frac{\sigma_{IR}(\omega)}{\sigma_{R}(\omega)}}\,. \tag{13}$$

Figure 7.7 plots the empirical transition dipole, μ_{emp}, for a few representative temperatures. The extracted frequency dependence of the transition dipole is largely independent of temperature while the frequency dependence of μ_{emp} is strongly nonlinear: the magnitude of the dipole increases by a factor of 2.6 from the gas phase frequency to 3600 cm^{-1}. On resonance at 3400 cm^{-1}, μ_{emp} is linear with a slope of -4.3×10^{-3} /cm^{-1}. The transition dipole changes by a factor of 1.7 over the line shape as defined by the FWHM of the 20° Raman spectrum (3300 cm^{-1} to 3580 cm^{-1}). On the red edge of the spectrum (~3200 cm^{-1}) μ_{emp} turns up again, strongly increasing with decreasing frequency.

The second transition dipole we consider is one recently calculated by Skinner and coworkers, μ_{SK}.[21] They performed DFT electronic structure calculations on randomly selected water clusters taken from MD simulations with the SPC-FQ potential. From these calculations they performed a linear fit relating the transition dipole to the electric field. We subsequently relate electric field to OH frequency using the relationship determined by Skinner and coworkers.[12] On resonance the slope of μ_{SK} is -5.3×10^{-3} /cm^{-1}, which is similar to the slope of μ_{emp}. It is on the wings of the spectrum (i.e. 3300 and 3600 cm^{-1}) that the two deviate significantly. The resultant μ_{SK} varies by a factor of 1.9 across the line shape as defined by the FWHM of the Raman spectrum (see above). Finally, we consider the transition dipole of Skinner with almost twice the slope, μ_{SK2}. This transition dipole is roughly a linear approximation to between the gas and liquid phase frequencies. On resonance the slope of μ_{SK2} is -10×10^{-3} /cm^{-1}, which is significantly larger than the slope of μ_{emp}, but this value agrees quite well with μ_{emp} on the wings of the spectrum. μ_{SK2} changes by a factor of 2.3 over the line shape.

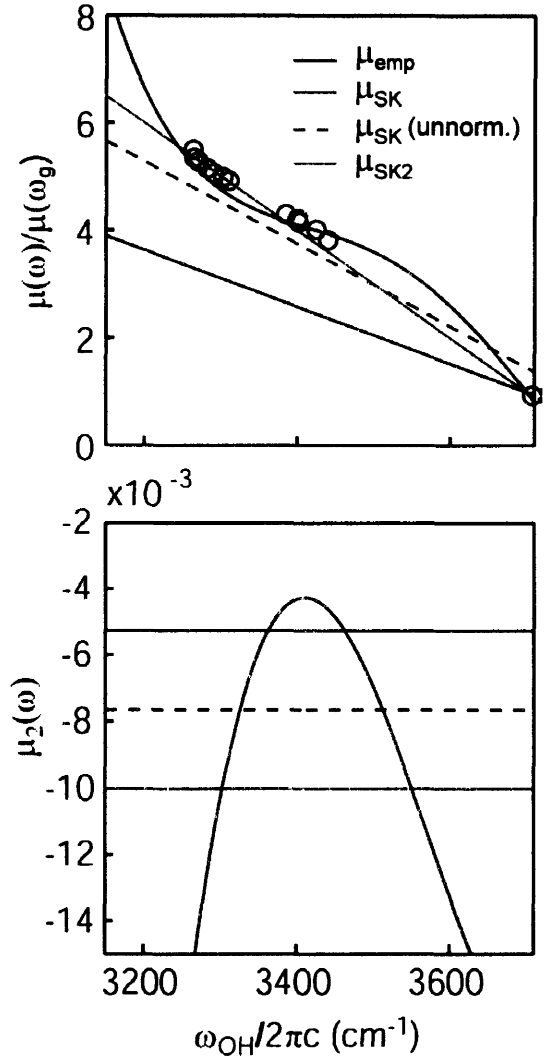

Figure 7.6. Plot of $\mu(\omega)$ (top panel) and μ_2 (bottom). The three transition dipoles correspond to μ_{emp} (blue), μ_{SK} (red), and μ_{SK2} (green). The unfilled circles in the top panel are from Ref 23.

Calculated IR spectra at 20° and 80° C using the three different transition dipoles as inputs into equation 8 can be found in Figure 7.8. The temperature dependence of the calculated spectra are quantified in the change of ε, ω*,and Γ as shown in Figure 7.2. In general the calculations follow the trends of the experimental IR spectra: ε decreases, ω* blue shifts and Γ increases with temperature. As anticipated, the spectra calculated with μ_{emp} agree well with the experimental spectra. Changes in the ε and ω* are in almost perfect agreement with the experimental values. Surprisingly, the trend of Γ with temperature deviates from the IR spectra, being in closer agreement with the trend of the Raman spectrum. It is important to note, however, that while the trend is not correct, the magnitudes of Γ are still in better agreement with the experiment as compared to the calculations with the other two transition dipoles. Spectra calculated with μ_{SK} are too far red shifted and too narrow by ~20 cm^{-1} each, while the overall intensity decreases by a factor of 2 too great at high temperatures. Spectra calculated with μ_{SK2} deviate even more significantly from the experimental values.

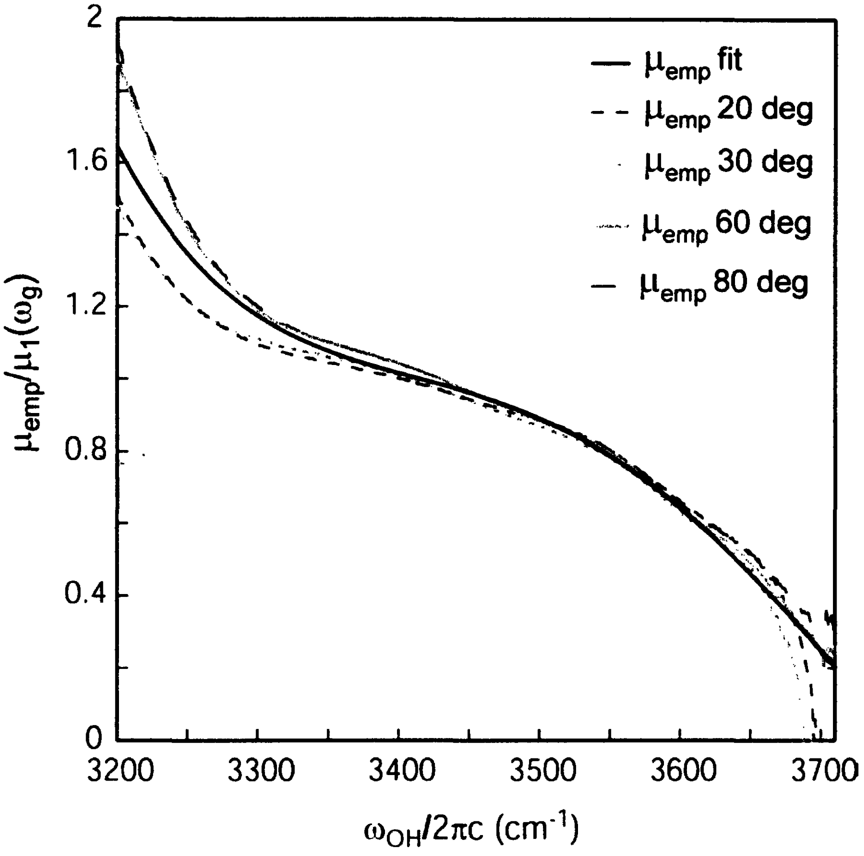

Figure 7.7. Extracted empirical transition dipole, μ_{emp}, calculated from the ratio of IR and Raman line shapes. μ_{emp} shows little temperature dependence.

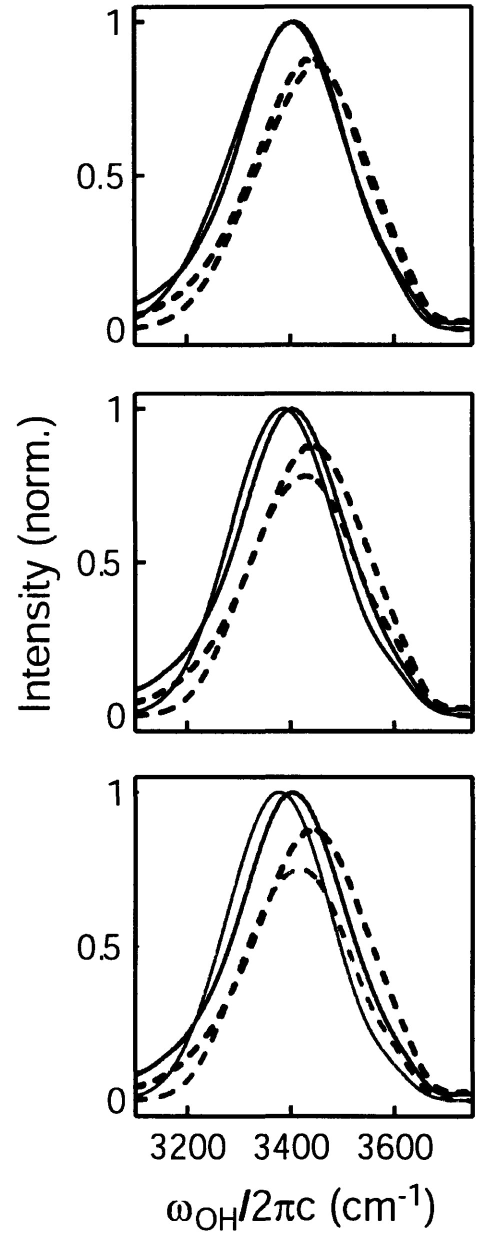

Figure 7.8. (Color) A comparison of experimental (black lines) and calculated line shapes at 20° (solid lines) and 80° C (dotted lines). Colored lines correspond to (blue), μ_{SK} (red), and μ_{SK2} (green).

Clearly, linear approximations of μ with frequency are unable to provide accurate IR line shapes in the static limit. Previous studies have also suggested a nonlinear dependence. Electronic structure calculations of Hermansson found a linear relationship between μ^2 and ω_{OH}, implying a square root dependence on μ with frequency.[26] Experiments have drawn similar conclusions. Studies on the OH stretch of HOD in various organic solvents by Glew and Rath found that the integrated area, A, of the line shape varied linearly with $\langle \omega_{OH} \rangle$.[16] Huggins and Pimental examined a series of hydrogen bonding systems and found that A varied linearly with $\Delta\nu$, the shift of the mean frequency from the gas phase value, for modest hydrogen bond strengths. For $\Delta\nu > 200$ cm^{-1}, the relationship between A and $\Delta\nu$ became sublinear.[15] The large slope of μ_{emp} at low frequencies (<3250 cm^{-1}) is also inconsistent with these experimental observations. The low frequency wing of the OH spectrum changes significantly with temperature and could be complicated by an underlying overtone of the HOD bend, which would make the accurate extraction of the transition dipole in this region of the spectrum difficult.

The calculated spectra are normalized to their 20° degree value and thus are not sensitive to the magnitudes of the transition dipole. This is not to say that the magnitudes are not important. The three cases examined differ significantly in the magnitudes of the transition dipole as a function of frequency. The experimental data of Iogansen serves as a convenient way to estimate this magnitude.[23] Iogansen investigated A vs. ω_{OH} for HOD in D_2O across a broad temperature range in the gas, liquid and ice phases. His data are plotted in Figure 7.6 and it bears striking similarity to . This agreement, however, may be somewhat fortuitous as the normalization of the transition dipole depends sensitively on the magnitude evaluated at the gas phase frequency. It is on the edges of the spectrum that μ_{emp} has the most noise (see Figure 7.7). Nevertheless, it shows that μ_{emp}, with the proper scaling, can predict the change in spectral intensity over a broad range of temperature and phases. The magnitude of μ_{SK} is too low by a factor of 2 while μ_{SK2} is roughly a linear approximation to the Iogansen data.

The decrease in the calculated echo intensity using equation 12 is similar for all three transition dipoles examined and agrees well with the experimental data within the signal to noise (shown in Figure 7.4). The experimental echo signal is best matched when μ_{emp} is used as an input into the static model. The μ^8 dependence of the homodyne echo signal results in the echo signal being particularly sensitive to the red side of the line shape where the magnitude of μ is larger. Calculations of the dispersed echo signal with the examined transition dipoles, excluding contributions due to the 1→2 transition, highlight this and are shown in Figure 7.9. Note that the calculated echo signal is not only significantly red shifted compared to the Raman spectrum but that it is also much narrower. This results in the homodyne echo not being particularly sensitive to how the dipole changes with frequency as the relevant spectral window that contributes to the echo signal is fairly small when compared to the breadth of the OH frequency distribution.

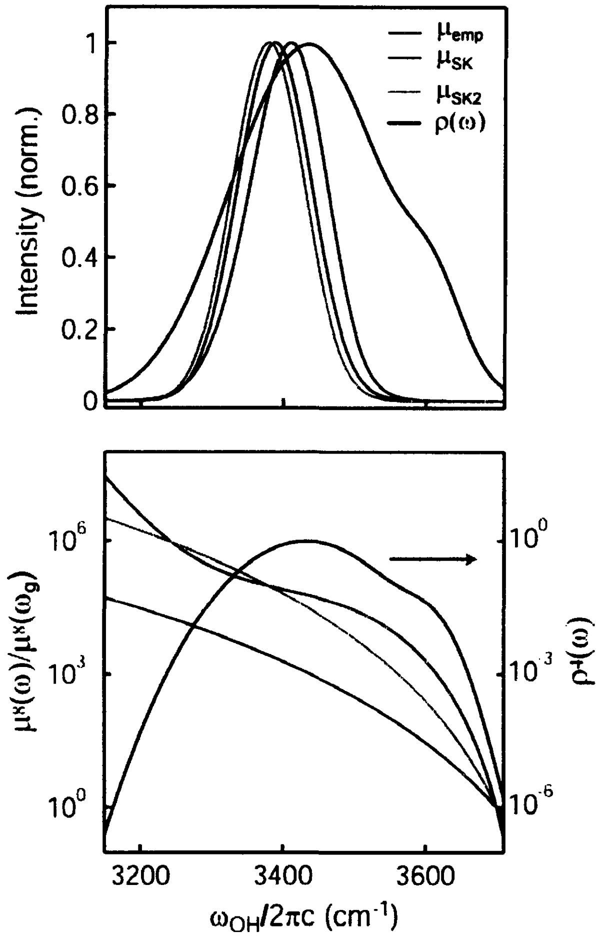

Figure 7.9. (Color) Calculation of the homodyne echo signal. The top panel shows the v=0→1 contribution to the echo signal. The echo signal is significantly red-shifted from the density of states due to the μ^8 scaling of the homodyne echo. The bottom panel plots μ^8 as a function of frequency along with the scaling of the density of states that occurs in the homodyne echo, $\rho^4(\omega)$.

7.6 MD simulations of the non-Condon effect

Up to this point the modeling of the temperature dependent spectral observables has assumed that on the timescales of the experiment that the frequencies of individual OH oscillators is static. Yet, the spectral relaxation of the OH stretch of HOD in D_2O is best described as somewhere in between the inhomogeneous and homogeneous limits. Ultrafast echo experiments measure a frequency correlation time of ~300 fs so while water is inhomogeneous it is only modestly so. Incorporation of a frequency dependent dipole into our previously developed MD simulations of the vibrational spectroscopy of the OH stretch of HOD in D_2O serves as a relatively easy extension to examine the influence of spectral relaxation on the Non-Condon effect. Classical MD simulations have done a surprisingly good job at reproducing IR observables including population relaxation[27,28], molecular reorientation[8], spectral diffusion[7,9] and recently 2D IR spectra[29,30]. While not providing quantitative agreement, MD simulations have been able to capture all the qualitative relaxation observed in IR experiments to date. Many recent papers have compared these IR observables to predications from MD simulations.[9,29,31,32]

Within our MD simulations, we have calculated linear and 2D IR spectra for the three transition dipoles examined above and in the limit of the Condon approximation. Calculations of the linear spectra using equation 7 are shown in Figure 7.10. It is instructive to first compare the OH frequency distribution and the Condon limit line shape. Spectral relaxation results in significant narrowing on both the red and blue sides of the IR line shape. The spectra calculated with the three transition dipoles are shifted by ~20 cm^{-1} from the Condon value and the wing on the blue side of the line shape is slightly suppressed. Inclusion of the non-Condon effect results in better agreement with the experimentally observed mean frequency but the line width is too narrow. While the MD calculated spectra show similar trends to what was observed in the static limit, the differences are greatly minimized. This result shows how fast spectral relaxation strongly reduces the differences between the three transition dipoles by averaging over the timescale of intermolecular fluctuations.

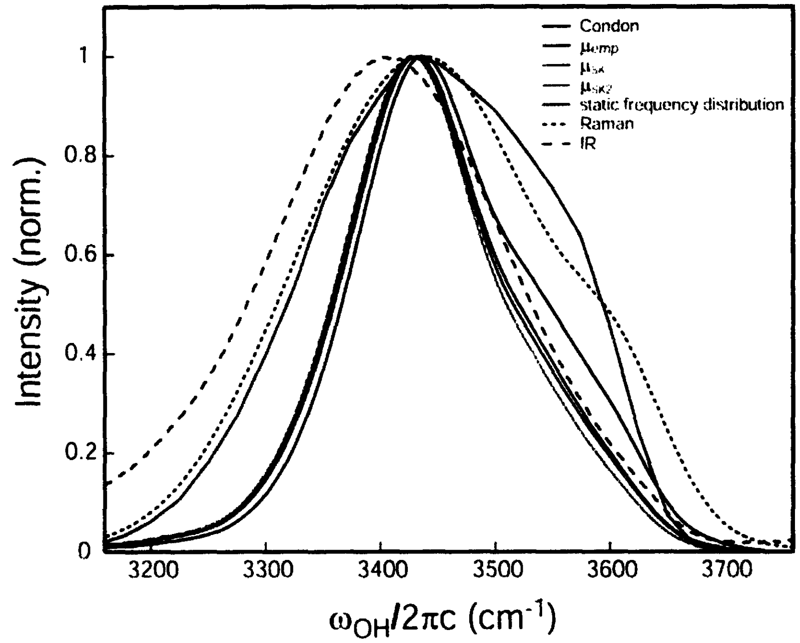

Figure 7.10. (Color) Plot of both experimental and MD calculated one dimensional linear spectra.

Calculated 2D IR spectra using equation 2 for the different cases of the transition dipole follow a similar trend as the linear spectra. The heterodyne-detected echo scales with the fourth power of the transition dipole and is shown in Fig. 7.11. In the homogeneous limit the 2D line shape is equal to the product of the one dimensional line shape in both frequency dimensions. Compared to the Condon line shapes the non-Condon effect acts to shift the frequency to the red and suppress the blue side of the diagonal. This acts to diminish the asymmetry in the line shape.

One should be cautious in over interpreting the results from the MD simulation. Calculations of the spectroscopy are only in qualitative agreement with the data. Slowing down of the simulated dynamics so that frequency relaxation is in better agreement with experimental results will likely result in more accurate line widths and may better highlight the differences between the three transition dipoles investigated.

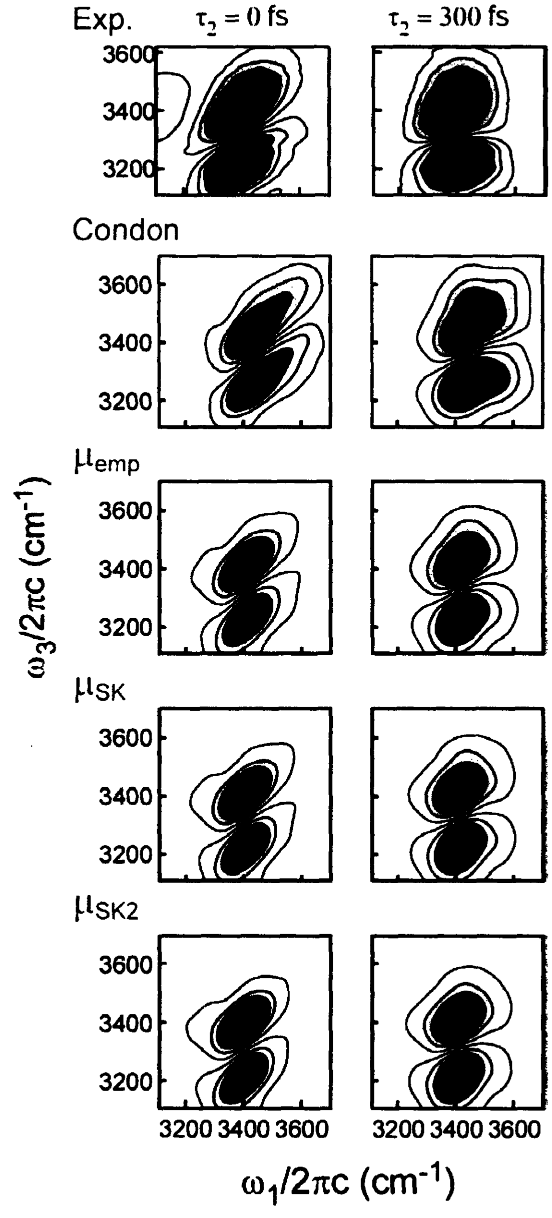

Figure 7.11. (Color) Experimental and MD calculated 2D IR line shapes in the Condon and non-Condon limits. Spectra are plotted with 15 evenly spaced contours. 2D spectra for the three transition dipoles examined are nearly identical.

7.7 Conclusions

Observations in the linear spectroscopy of hydrogen bonded systems have long suggested that increases in hydrogen bonding strength strongly modulate the magnitude of the transition dipole of the hydride stretch. We have measured the transition dipole as a function of frequency for the OH stretch of HOD in D_2O by conducting temperature dependent linear and nonlinear spectroscopies. These experiments exploit the shift in the density of states that occurs with a change in temperature to isolate the transition dipole.

Direct inversion of the IR and Raman data yielded μ_{emp}. Within the static limit μ_{emp} best reproduces the temperature dependent experimental data presented here, resulting in an accurate reproduction of the data of Iogensen and the IR line shapes. Maybe most impressively, calculations within the static limit with μ_{emp} as an input are able to accurately reproduce the decrease in the homodyne echo intensity with temperature. Calculations of the transition dipole by Skinner and coworkers were also in reasonable agreement with the data, although predicting too large of a red shift of the IR band. On resonance the slopes of μ_{emp} and μ_{SK} with frequency are nearly identical, but they deviate fairly significantly on the wings of the OH spectrum. The nonlinear dependence of the transition dipole at low fields strengths, present in μ_{emp} but not μ_{SK}, is essential to get the line shape correct in the static limit. There is a long history of empirical observations that have suggested a sublinear relationship between the transition dipole and the shift of the frequency from the gas phase. Further electronic structure calculations are necessary to understand the origin of this effect.

The significant change in the homodyne echo intensity with temperature provides the first experimental verification of the importance of the frequency dependence of the transition dipole in nonlinear measurements of water. Echoing the conclusions of Skinner and coworkers[13], modeling within the static limit concludes that the homodyne echo primarily probes the low frequency side of the line shape. Increasing the temperature shifts the density of states to higher frequency, resulting in a decrease in intensity. Unlike the linear spectroscopy, which is highly dependent on which transition dipole was examined, the decay of the echo signal with temperature is very similar for the cases of the transition dipoles examined.

MD simulations suggest that the differences between the three transition dipoles examined are largely washed out when one accounts for the spectral diffusion of OH oscillators. It is important to note, however, that spectral diffusion is about a factor of 2 faster compared to the experimental measures. Non-Condon effects manifest themselves in the 2D IR spectrum as suppression of the high frequency side of the line shape. Calculated 2D line shapes maintain their asymmetry that is observed in the experiment, although suppressed to a lower contour level.

Acknowledgements

I gratefully acknowledge Jared Smith and Richard Saykally for providing the temperature dependent Raman spectra and Sean Roberts for conducting the MD simulations.

References

1 J. D. Smith, C. D. Cappa, K. R. Wilson, B. M. Messer, R. C. Cohen, and R. J. Saykally, Science 306, 851 (2004).

2 P. Wernet, D. Nordlund, U. Bergmann, M. Cavalleri, M. Odelius, H. Ogasawara, L. Å. Näslund, T. K. Hirsch, L. Ojamäe, P. Glatzel, L. G. M. Pettersson, and A. Nilsson, Science 304, 995 (2004).

3 S. Woutersen and H. J. Bakker, Nature 402, 507 (1999).

4 D. Eisenberg and W. Kauzmann, *The Structure and Properties of Water.* (Clarendon Press, Oxford, 1969).

5 *Water - A Comprehensive Treatise*, edited by F. Franks (Plenum, New York, 1972-1982), Vol. 1-7.

6 E. T. J. Nibbering and T. Elsaesser, Chem. Rev. 104, 1887 (2004).

7 R. Rey, K. B. Moller, and J. T. Hynes, J. Phys. Chem. A 106 (50), 11993 (2002).

8 C. P. Lawrence and J. L. Skinner, J. Chem. Phys. 118, 264 (2003).

9 C. J. Fecko, J. D. Eaves, J. J. Loparo, A. Tokmakoff, and P. L. Geissler, Science 301, 1698 (2003).

10 J. D. Eaves, A. Tokmakoff, and P. Geissler, J. Phys. Chem. A 109, 9424 (2005).

11 S. Mukamel, *Principles of Nonlinear Optical Spectroscopy.* (Oxford University Press, New York, 1995).

12 S. A. Corcelli and J. L. Skinner, J. Chem. Phys. 109, 6154 (2005).

13 J. R. Schmidt, S. A. Corcelli, and J. L. Skinner, J. Chem. Phys. 123, 044513 (2005).

14 E. Marechal and S. Bratos, J. Chem. Phys. 68 (4), 1825 (1978).

[15] C. M. Huggins and G. C. Pimentel, Spectral Properties of Hydrogen Bonding Systems, 1615 (1956).

[16] D. N. Glew and N. S. Rath, Canadian Journal of Chemistry 49, 837 (1971).

[17] C. Sandorfy, in *The hydrogen bond: Structure and spectroscopy*, edited by P. Schuster, G. Zundel, and C. Sandorfy (North-Holland Publishing Company, New York, 1976).

[18] C. J. Fecko, J. J. Loparo, S. T. Roberts, and A. Tokmakoff, J. Chem. Phys. 122, 054506 (2005).

[19] J. R. Reimers and R. O. Watts, Mol. Phys. 52 (2), 357 (1984).

[20] J. D. Smith, C. D. Cappa, K. R. Wilson, R. C. Cohen, P. L. Geissler, and R. J. Saykally, Proc. Nat'l. Acad. Sci, USA 102, 14171 (2005).

[21] S. A. Corcelli, C. P. Lawrence, and J. L. Skinner, J. Chem. Phys. 120, 8107 (2004).

[22] T. Hayashi, T. l. C. Jansen, W. Zhuang, and S. Mukamel, J. Phys. Chem. A 109 (1), 64 (2005).

[23] A. V. Iogansen, Spectrochim. Acta 55, 1585 (1999).

[24] M. Khalil, N. Demirdoven, and A. Tokmakoff, J. Phys. Chem. A 107 (27), 5258 (2003).

[25] M. Khalil and A. Tokmakoff, Chem. Phys. 266 (2-3), 213 (2001).

[26] K. Hermansson, J. Chem. Phys. 99, 861 (1993).

[27] C. P. Lawrence and J. L. Skinner, J. Chem. Phys. 117 (12), 5827 (2002).

[28] R. Rey, K. B. Moller, and J. T. Hynes, Chem. Rev. 104, 1915 (2004).

29 J. D. Eaves, J. J. Loparo, C. J. Fecko, S. T. Roberts, A. Tokmakoff, and P. L. Geissler, Proc. Nat. Acad. Sci. USA. 102, 13019 (2005).

30 J. J. Loparo, S. T. Roberts, and A. Tokmakoff, J. Chem. Phys. 125, 194522 (2006).

31 J. B. Asbury, T. Steinel, C. Stromberg, S. A. Corcelli, C. P. Lawrence, J. L. Skinner, and M. D. Fayer, J. Phys. Chem. A 108, 1107 (2004).

32 E. Harder, J. D. Eaves, A. Tokmakoff, and B. J. Berne, Proc. Nat. Acad. Sci. 102, 11611 (2005).

Joseph J. Loparo

395 Beacon St. #2R
Boston, MA 02116
617-266-4637
Loparo@mit.edu

77 Massachusetts Ave.
Room 6-030
Cambridge, MA 02139
617-253-7372
617-253-7030 (fax)
web.mit.edu/~tokmakofflab

Education

Massachusetts Institute of Technology, Dept. of Chemistry Fall 2001-current
Ph.D., Chemistry, expected Fall 2006
Thesis: *Ultrafast structural fluctuations and rearrangements of water's hydrogen bonded network*
Advisor: Andrei Tokmakoff
GPA: 5.0/5.0

Case Western Reserve University Fall 1997-Spring 2001
B.S. with Honor's, May 2001, Summa Cum Laude
Honor's Thesis: *The ultrafast dynamics of five- and six-coordinate iron porphyrins*
Advisor: M.Cather Simpson
GPA: 3.93/4.00

Honors and Awards

Massachusetts Institute of Technology
Dept of Defense NDSEG predoctoral fellowship, Fall 2001 – Fall 2004
Best Poster Prize, *Liquids* Gordon Research Conference, August 2003
Lester Wolfe predoctoral fellowship, Fall 2005-Fall 2006

Case Western Reserve University
The Freshmen Chemistry Achievement Prize, for highest achievement, Spring 1998
Dean's High Honor's, every semester in attendance
Golden Key National Honor Society, Inducted Fall 1999
W.R. Veazey Prize, for achievement in physical chemistry, Spring 2000
The Carl F. Prutton Prize, for outstanding achievement in chemistry, Spring 2001

Publications

1) *Transient Raman Observations of Heme Vibrational Dynamics in Five-coordinate Iron Porphyrins* Loparo, J.J; Cheatum, C.M..; Ondrias, M.R.; Simpson, M.C. , **Chem. Phys**. 286 (2003) 353-274.

2) *Ultrafast Hydrogen Bond Dynamics in the Infrared Spectroscopy of Water* Fecko, C.J.; Eaves, J.D.; Loparo, J.J.; Tokmakoff, A.; Geissler, P.L., **Science** 301 (2003) 1698-1702.

3) *Reorientational and Configurational Fluctuations in Water Observed on Molecular Length Scales* Loparo, J.J.; Fecko, C.J.; Eaves, J.D.; Roberts, S.T.; Tokmakoff, A., **Phys. Rev. B** (2004).

4) *Generation of 45 Femtosecond Pulses at 3 μm with a $KNbO_3$ Optical Parametric Amplifier* Fecko, C.J.; Loparo, J.J.; Tokmakoff, A., **Opt. Comm.** 241 (2004) 521-528.

5) *Local Hydrogen Bond Dynamics and Collective Reorganization of Water: Ultrafast Infrared Spectroscopy of HOD in D_2O* Fecko, C.J.; Loparo, J.J.; Roberts, S.T.; Tokmakoff, A., **J.Chem. Phys.** 122 (2005) 054506.

6) *Hydrogen Bonds in Liquid Water are Broken Only Fleetingly.*Eaves, J.D.*; Loparo, J.J*; Fecko, C.J.; Roberts, S.T.; Tokmakoff, A. ; Geissler, P.L., **Proc. Natl. Acad. Sci. USA**. 102 (2005) 13019-13022. *coauthors

7) *Characterization of spectral diffusion from two-dimensional lineshapes* Roberts, S.T.; Loparo, J.J.; Tokmakoff, A.; **J. Chem Phys.** 125 (2006) 084502.

8) *Multidimensional infrared spectroscopy of water I. Vibrational dynamics in 2D lineshapes* Loparo, J.J.; Roberts, S.T.; Tokmakoff, A.; **J. Chem Phys.** 125 (2006) 194521.

9) *Multidimensional infrared spectroscopy of water II. Hydrogen bond switching dynamics* Loparo, J.J.; Roberts, S.T.; Tokmakoff, A.; **J. Chem Phys.** 125 (2006) 194522.

Conference Proceedings

1) *A Unified Analysis of Ultrafast Vibrational and Orientational Dynamics of HOD in D_2O* Loparo, J.J.; Fecko, C.J.; Eaves, J.D.; Roberts, S.T.; Tokmakoff, A., in **Ultrafast Phenomena XIV** (eds. Kobayashi, T.; Okada, T.; Kobayashi, T.; Nelson, K. A.; & DeSilvestri, S.) (Springer-Verlag, Berlin, 2005).

2) *Dynamics of hydrogen bonds in water: vibrational echoes and two-dimensional infrared spectroscopy* Fecko, C. J.; Eaves, J.D.; Loparo, J.J.; Roberts, S.T.; Tokmakoff, A.; in **Ultrafast Phenomena XIV** (eds. Kobayashi, T.; Okada, T.; Kobayashi, T.; Nelson, K. A.; & DeSilvestri, S.) (Springer-Verlag, Berlin, 2005).

3) *2D IR Spectroscopy of Hydrogen Bond Switching in Liquid Water* Loparo, J.J.; Roberts, S.T.; Tokmakoff, A. in **Ultrafast Phenomena XV** (August 2006) in press.

Presentations

1) *Ultrafast Hydrogen Bond Dynamics in Water: Ultafast Infrared Spectroscopy* Presentation at Laser Science XX: The 88th OSA *Annual Meeting* in Rochester, NY, October 2004.

2) *Two-dimensional IR spectroscopy: Observing coherent vibrations and hydrogen bond dynamics in water* Invited Presentation at The Multidimensional Spectroscopy Symposium sponsored by the G.R. Harrison Laboratory at MIT, January 2005.

3) *Probing ultrafast hydrogen bond dynamics on water's energy landscape* Presentation at Spring National Meeting of the ACS San Diego, CA, March 2005.

4) *2D IR spectroscopy of hydrogen bond switching in liquid water* at the Fifteenth International Conference on Ultrafast Phenomena in Monteray, CA, August 2006.

5) *Experimental observations of hydrogen bond dynamics in liquid water* at Fall National Meeting of the ACS San Francisco, CA, Sept. 2006.

Posters

1) *The Ultrafast Infrared Spectroscopy of Water* Presented at The Chemistry and Physics of Liquids: Gordon Research Conference August 2003.

2) *A Unified Analysis of Ultrafast Vibrational and Orientational Dynamics of HOD in D_2O* Presented at Ultrafast Phenomena in Niigata, Japan July 2004.

3) *A Unified Analysis of Ultrafast Vibrational and Orientational Dynamics of HOD in D_2O* Presented at Water and Aqueous Solutions: Gordon Research Conference August 2004.

Professional Organizations

American Chemical Society: Student member since 2000

Optical Society of America: Student member since 2004